Multiphase Simulations of a Lyocell Process

Marinus H. Bouwman

Department Mineral Resources and Petroleum Engineering
Lehrstuhl für Petroleum Production and Processing

Montanuniversität Leoben

A thesis submitted for the degree of

Doktor der Montanistischen Wissenschaften

October 2008

I declare in lieu of oath, that I wrote this thesis and performed the associated research myself, using only literature cited in this volume.

Marinus H. Bouwman

I would like to dedicate this thesis to my wife Sandra who supported me in every possible way while at the same time giving me two wonderful daughters, Ameline and Romy.

Acknowledgements

I would like to thank the following people and institutions for making this thesis possible.

The company Lenzing AG for the highly interesting topic. Everybody at the Lyocell plant has been a great help. In particular I would like to thank Mr C. Schrempf for his ideas and input.

The company Mittersil for donating 18kg of scheelite.

The company ICE Strömungsforschung GmbH and in particular its employees that developed the tools used in this thesis: Mr G. Boiger (icoLagrangianFoam), Mr J. Leixnering (reconstruction algorithm), Mr B. Gschaider (optimisation), Mr M. Gruber (non-Newtonian fluids) and finally Miss A. Kreuzig for dealing with any logistic issue in an amazing tempo.

The Montanuniversity Leoben for offering me the PhD position. Mr. H. Mali for his expertise on mineralogy and optical microscopy. Mr R. J. Bakker for letting me use his Raman Spectroscope. Mr B. Lederhaas for the amazing work with the SEM. Professor Jäger and Professor Teichert for showing me the microscopic world of surfaces. Professor H. Flachberger and Mr A. Böhm for lending me there laboratory and helping me with the processing of the Scheelite. My colleagues from the Department who made four years look like a very short time. Thank you Gebhard, Michi and Adel.

Finally, I am very thankful to professor W. Brandstätter for giving me new insights in the world of CFD.

Abstract

The thesis deals with the simulation and optimisation of parts of the Lyocell process. Starting with trees and ending with cellulose fibres, the Lyocell process is one of the most advanced methods for creating natural fibres without causing any pollution to the environment.

In particular, the filter systems and the spinneret at the end of the spinning process are studied in detail. After locating the key players that prohibit the spinneret to function continuously, possible blocking theories are described.

Using the possibilities of Computational Fluid Dynamics (CFD), these theories are than verified by computer simulations. Finally, after studying the optimisation potential, the filters and spinneret are optimised using a variational method.

A very complex and highly advanced industrial process has been investigated intensively from various angles while at the same time, solid suggestions on improvements are given.

Contents

List of Figures

List of Tables

Nomenclature

Roman Symbols

$\boldsymbol{a}$	acceleration
$\boldsymbol{b}$	body force
$\boldsymbol{D}$	strain tensor
$\boldsymbol{F}$	force
F_b	Basset force
F_d	drag force
F_l	lift force
F_{vm}	virtual mass force
g	gravity
$\boldsymbol{I}$	unit tensor
k	time constant
L	characteristic length
m	consistency index
M	total momentum transfer
m	mass

$\dot{m}$	mass flux
n	power law index
$\boldsymbol{n}$	unit vector
p	static pressure
S	surface
t	time
$\boldsymbol{T}$	surface force
Tr	tensor trace
u	velocity vector component
$\boldsymbol{U}$	velocity vector
U_m	average velocity
x	cartesian coordinate

Greek Symbols

α	mobility factor
α_i	fluid volume fraction of phase i
ϵ	elongation parameter
Φ	extensive general property
ϕ	intensive general property
$\dot{\gamma}$	strain rate
λ	relaxation time
μ	dynamic viscosity
ν	kinematic viscosity

Ω volume

ρ density

$\boldsymbol{\tau}$ viscoelastic stress tensor

ξ slip parameter

Superscripts

n new values

o old values

Subscripts

0 denotes constant linear viscoelastic material functions

c continuous phase

CM control mass

coll particle collision effects

CV control volume

d dispersed phase

f fluid

ij ijth tensor component

k kth vector component

N information belonging to cell N

P information belonging to cell P

p particle

wall particle-wall interaction

Other Symbols

CFD Computational Fluid Dynamics

CP crossed polars

CRT Cathode-Ray Tube

FD Finite Difference method

FE Finite Element method

FV Finite Volume method

∞ infinity

$\int$ integral

∇ nabla operator, gradient

$\nabla\times$ curl

$\nabla\cdot$ divergence

∇^2 Laplacian

OM Optical Microscopy

PEEK Polyetheretherketone

PP plane-polarized

Re Reynolds number

RS Raman Spectroscopy

SEM Scanning Electron Microscope

$\sum$ surface area per unit volume

VoF Volume of Fluid

Chapter 1

Introduction

Clothing has always been an essential (t)issue for mankind ever since we left the trees and started walking upright. However, its been a long road from wearing animal skins up to Milan's fashion week. Over centuries, classical tissues such as wool and animal skin have been used. Early high cultures, mainly from the east, already knew how to produce fine fabrics from plants such as cotton and linen. It was not until the industrial revolution and the creation of plastics that clothes are being made from unnatural substances such as polyester.

Ironically enough, at the beginning of the twentieth century, people have started creating natural fibres out of cellulose, the basic substance that trees are made of. So after hundreds of thousands of years, mankind is back where it started its fashion journey.

Creating natural fibres with amazing properties from cellulose sounds easier than it is. The oldest process, the viscose process, needs a lot of chemicals in order to dissolve the cellulose so that it can be manufactured. Most of these chemicals are lost during the process and a lot of energy is needed as well.

In the past decades, all industries have acknowledged that, in order to remain long term global players, their processes must be energetically optimised. Also, pollutants such as toxic chemicals are reduced to a minimum. It should be no surprise that the viscose process was also undertaken a thorough study of how it could fit the ecological principles better and in the eighties the Lyocell process

was born. This process uses mainly one organic substance that can dissolve cellulose and is recovered in the process for almost 100%.

In this thesis, an overall study is made of the Lyocell process, in particular what happens at the end of the process where the cellulose mass, the dope, is pressed through a large ring containing thousands of very small holes. Although this process is actually an extrusion, it is called *spinning* and the ring with holes is called the *spinneret*.

At the Montanuniversity, a lot of different disciplines are present that helped to look at the situation from many different angles in order to get a complete overlook. The mineralogy of the solid particles in the dissolved cellulose are studied using different microscopic methods such as optical microscopy, scanning electron microscopy and Raman spectroscopy (geology and metallurgy department). The mineral scheelite has been applied as a dopant for a large scale experiment. Before it was used, however, it needed to be refined and processed (Mineral processing department). At the same time, a complex production process such as the Lyocell process had to be studied and understood before improvements could be suggested. It should be clear that basic chemistry, physics and mechanics are only a near necessity to grasp all this (physics and petroleum engineering department). This thesis embraces most of the competence present at the Montanuniversity.

1.1 Motivation

The Lyocell process is a very modern and advanced method of creating natural fibres from cellulose without polluting our environment. The process recycles 99% of all the chemicals used and is far more energy efficient than any previous method. However, at the same time, the method is very young and as with all youngsters, there is still a lot to learn before the process runs without any failures or interruptions.

One of the major issues is that in the spinneret some of the holes get blocked. Whenever this happens, the process needs to be interrupted and as for any industrial process, this costs time and money.

The company Lenzing AG allowed Mr Bouwman to take a closer look at their spinning process in order to find the reasons for the blocking of the spinneret. Through numerous discussions it became clear that a lot of improvements have already been implemented, such as the introduction of several filters. However, it is doubted if these filters function optimally which is exactly what is studied in this thesis.

1.2 Objective

From earlier investigations it is known that solid particles such as sand grains and gel particles, that are in fact badly dissolved cellulose, might block the filters and hence the flow through the spinneret. The objective of this thesis is to find the exact mechanisms that block the filters and the spinneret and how these mechanisms can be influenced in order to maximise the operating time of the spinneret.

1.3 Outline

The second chapter briefly describes the ideal Lyocell process in general. Here every aspect of the Lyocell process is described what it should do and how the process would work without any interruptions. At the same time a comparison is made with a real Lyocell process with all the difficulties that can arise. In chapter three, all the experiments conducted on all the major actors in the Lyocell process are explained in great detail. All the results are discussed in order to set up blocking theories in chapter four. Using these blocking theories, computer simulations using Computational Fluid Dynamics (chapter five) were carried out to test the theories (chapter six) and finally to find optimisation possibilities of the situations at hand (chapter seven). At the end of the thesis, conclusions based on the work done are drawn. This complete process is sketched in figure 1.1.

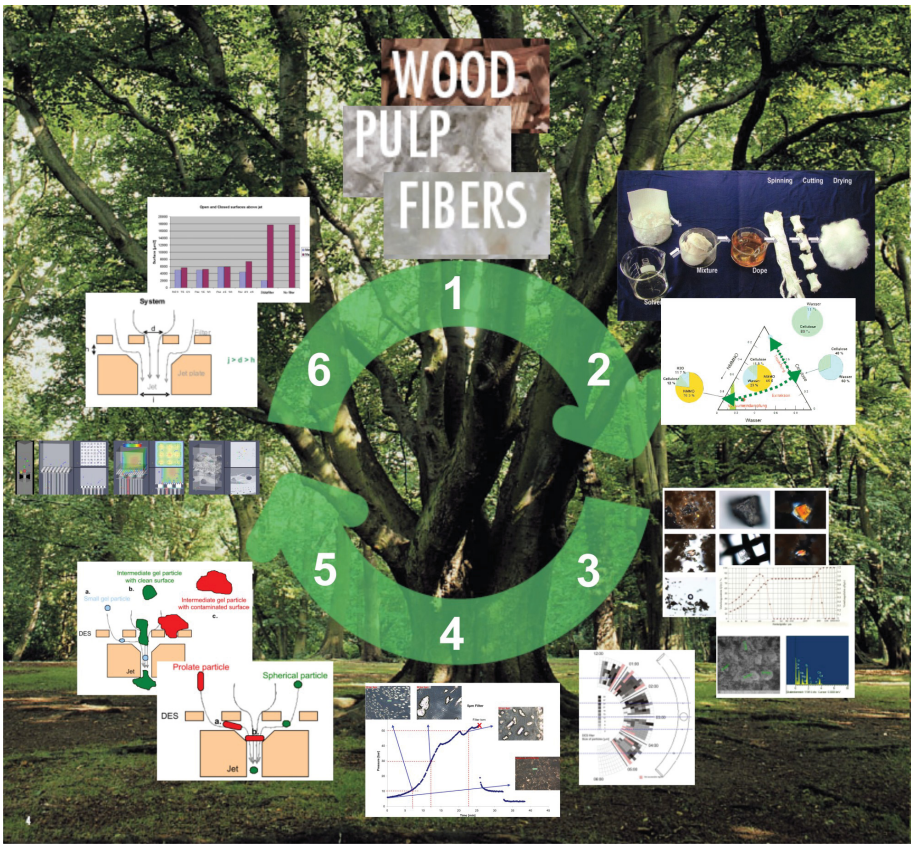

Figure 1.1: Outline of this thesis (source background image: Lenzing AG)

Chapter 2

The Lyocell Process

2.1 Introduction

Lyocell is a textile fibre made from wood pulp or cellulose. Lyocell shares many properties with other cellulosic fibres such as cotton, linen, ramie and rayon. Some main characteristics of Lyocell fibres are that it is soft, absorbent, very strong when wet or dry, and resistant to wrinkles; so my wife says.

In the past, toxic chemicals were needed to produce cellulose based fibres in the so called viscose process [36, 39]. However, in the eighties, Akzona (Akzo Nobel) introduced a new technique called solvent spinning [19, 22, 23, 50, 65]. In this process, the wood pulp or cellulose is directly dissolved in an organic amino oxide solvent called N-Methylmorpholine N-oxide (NMMO), creating a solution called *dope*. The dope is pushed through a spinneret to form the individual fibres. After the dope has been spun into Lyocell fibres, these fibres are washed and the amino oxide is retrieved from the water, purified, and recycled [37]. Since there is little by-product, this process is relatively eco-friendly [26, 27].

Lyocell was first manufactured and marketed in the nineties by Courtaulds and by Lenzing AG [49]. Lenzing markets this fibre under the name Tencel®. The fibre is classified as a sub-category of Rayon, also known as viscose, and is used in the production of many clothes, such as jeans, trousers and coats.

The following section will describe the ideal and optimal Lyocell process. However, as so often in life, hardly anything goes as planned and therefore, the problems in a real Lyocell process are discussed briefly in the final section of this chapter.

2.2 Ideal Lyocell Process

This paragraph briefly describes the complete production process from native cellulose I to man-made cellulose II [9]. A sketch of the large scale Tencel® process is given in figure 2.1 with the major steps indicated by capital letters. Figure 2.2 shows the intermediate products on a small scale.

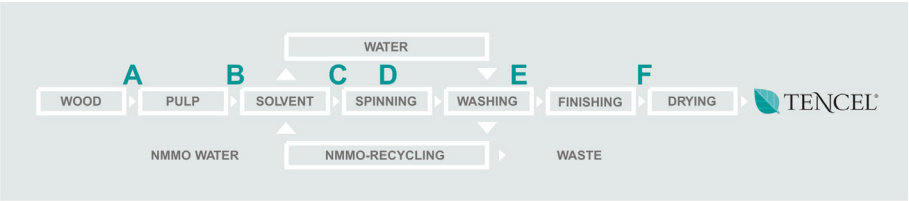

A Grinding of native cellulose I
B Dissolving of cellulose I to form dope
C Filtering impurities out of dope
D Spinning of fibers
E Washing NMMO out of cellulose II
F Cutting, drying and wrapping of final product

Figure 2.1: Tencel® production process (Lenzing AG)

2.2.1 Cellulose I (A)

At the start of the production process, cleaned native cellulose I is bought on roles and looks and feels a bit like cardboard material. This solid material must be liquefied so that it can be extruded through the spinneret (see section 2.2.4). Cleaned cellulose means that there are no major dirt particles present any more and the cellulose chains are broken by the use of boiling, ozone or peroxides, depending on the wanted chain length. This cellulose is now grinded to parts of about 10mm in size so that it dissolves more easily in the NMMO solvent.

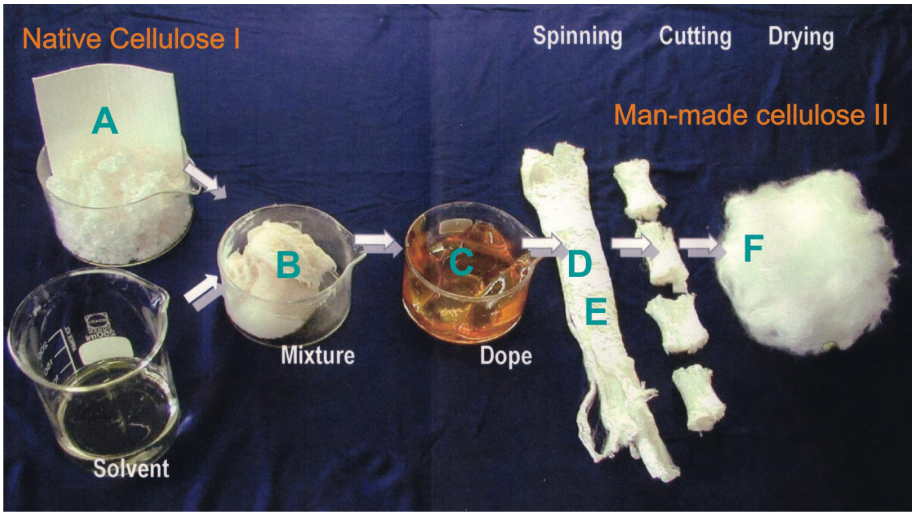

Figure 2.2: End and intermediate products for the complete production process of cellulose II

2.2.2 Dope, a cellulose-NMMO-water mixture (B)

N-Methylmorpholine-N-oxide monohydrate (NMMO) is used as an organic solvent of amino oxide for direct dissolution of cellulose in the Lyocell process. Ideally, Lyocell fibre production should be an entirely physical process without chemical changes in the pulp or the solvent[62]. NMMO reacts exothermal with fast rising temperatures and it oxidises with itself which makes it difficult to experiment with. Figure 2.3 contains a sketch of the chemical composition of NMMO and the position of the solvent in the Lyocell process. Practically all NMMO is recovered in the spinning bath (see 2.2.4) and reused for dissolving cellulose I.

At room temperature, NMMO is a mixture of a liquid phase and a crystallized phase. At 60℃ it is a liquid and feels like oil. The NMMO solvent is used in a dihydrate form, with about 78% NMMO content. Only the monohydrate form of NMMO with about 86% NMMO can dissolve cellulose. The water content in the NMMO mixture is of crucial importance for the solving process of the cellulose and is solely controlled by the temperature (distillation). The phase diagram of the NMMO-water mixture as derived by Biganski is shown in figure 2.4 [3].

The mixing of the cellulose and the dihydrate NMMO is done at 80℃. The

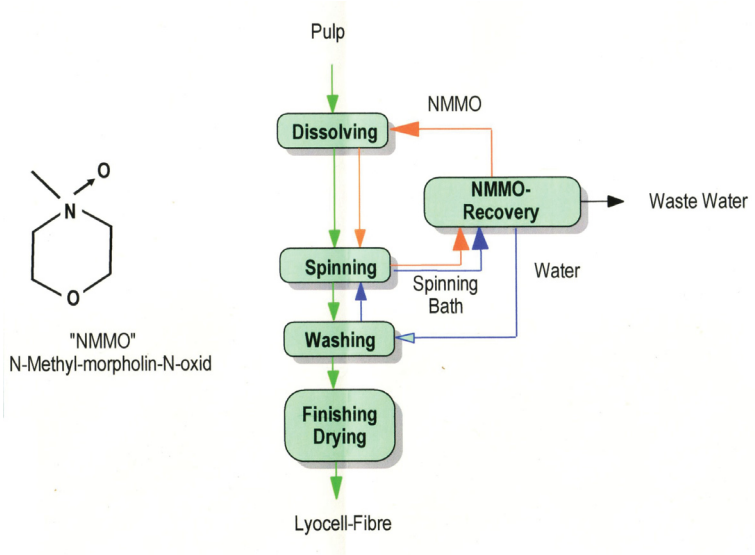

Figure 2.3: Chemical structure of NMMO (left) and the position of NMMO in the Lyocell process

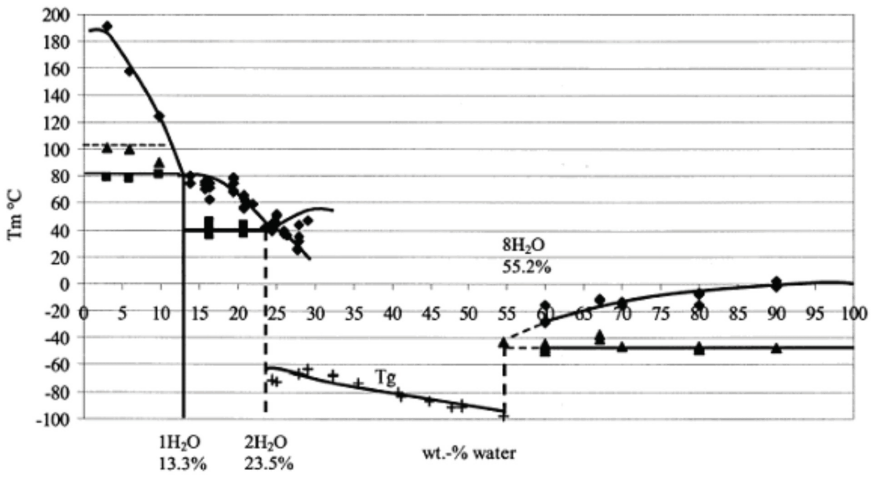

Figure 2.4: NMMO-water phase diagram [3]

cellulose gets impregnated and forms kind of a suspension. The NMMO only detaches the cellulose strings and moves them away from each other in such a way that they do not *feel* each other any more. This way, they can move freely through the solution. The solving of cellulose by NMMO is irreversible at certain H_2O content.

After the impregnation of the cellulose with NMMO, the mixture is slowly heated to 110℃ by using a filmtruder. This way, the dope (or spin mass) gets formed. The dope is a mixture of cellulose, NMMO and water, typically in ranges of:

- 10-15% cellulose
- 9-12% H_2O
- 73-81% NMMO

The exact percentage depends on the kind of cellulose that is used. Stabilizers are added to the dope for catalytic reasons and to control the temperature of the mixture. These stabilizers are not thought to influence the behaviour of the dope [62].

At this stage, the dope can contain several impurities such as gel particles (badly dissolved cellulose, high concentrated cellulose), organic solid particles (undissolved cellulose, wood) and anorganic solid particles (silicates, sand). The exact origin and properties of these particles are discussed in more detail in section 2.3. The complete phase diagram of the cellulose-NMMO-water mixture is plotted in figure 2.5.

2.2.3 Filters (C)

In the spin mass or dope, solid organic (cellulose) and anorganic (silicate) particles exist. These can obstruct the spinning process and must be removed. This is done by three filters in the Lyocell process:

1. **KREY**: *Kreyenbourg* filter right after the filmtruder
2. **DHS**: *Düse Haupt Sieb* filter after the dispenser of the spin mass and before the jets
3. **DES**: *Düse Einlege Sieb* filter right before the jets

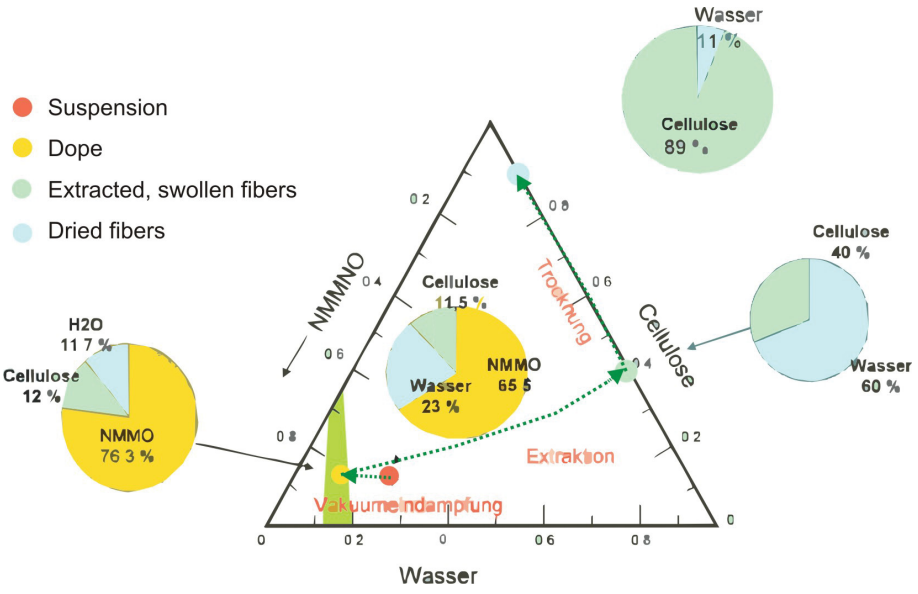

Figure 2.5: Phase diagram of the cellulose-NMMO-water mixture (Lenzing AG)

2.2.3.1 Kreyenbourg Filter (KREY)

Once the spin mass is formed, a multilayer surface filter is used to filter out impurities, i.e. the Kreyenbourg filter or KREY. This filter is about 150mm in diameter and consists of seven filter layers, all of different mesh spacing and wire thickness as described in table 2.1 and shown in figure 2.6. The finest mesh spacing in the centre of the filter is needed to filter out the small particles; the larger filters at both sides of the filter are needed to give the small filters enough strength to withstand the high pressures over the filter (up to 60 bar). The filter is a two-way filter. This means that it cleans itself automatically by means of reversed flow.

Ideally, the KREY takes out all impurities. At the end of the spinning process, before the spinneret, there are two more filters, i.e. the DHS and DES filter which have a drainage effect rather than a filter effect. Figure 2.7 shows a sketch of the location of the filters.

Table 2.1: Description of each layer of the KREY filter

Layer	Mesh spacing [mm]	Wire thickness [mm]	Walsed	Sintered
1	0.63	0.40	X	
2	0.25	0.16	X	
3	0.10	0.063		X
4	0.02	0.02		X
5	0.10	0.063		X
6	0.25	0.16	X	
7	0.63	0.40	X	

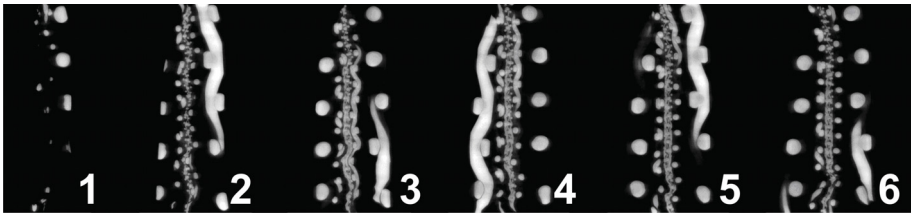

Figure 2.6: Six consecutive CT images perpendicular to layers

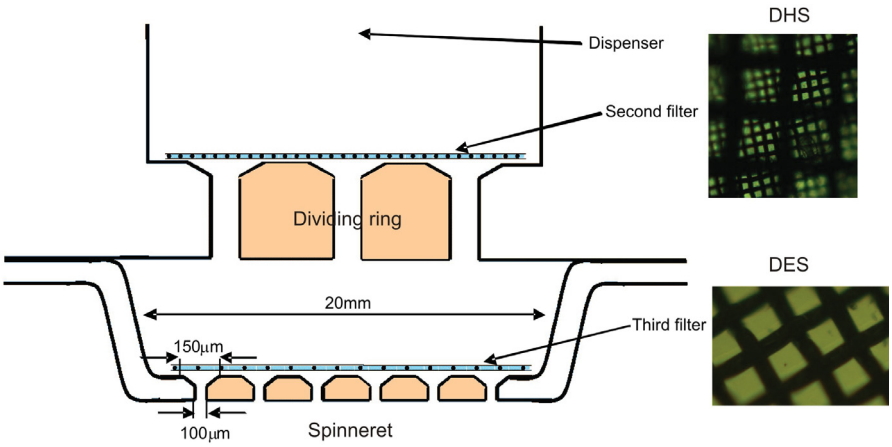

Figure 2.7: Sketch of the position of the second (DHS) and the third filter (DES) after the dispenser and before the extrusion jets in the spinneret with optical microscope images of both filters on the right

2.2.3.2 Düse Haupt Sieb Filter (DHS)

The *Düse Haupt Sieb* (DHS) consists of two quadrature woven meshes. The coarse mesh is used as stabilizer for the finer mesh. The dimensions of the mesh are summarized in table 2.2. The finer mesh is much coarser than the finest mesh of the KREY filter. Hence, its main purpose is to take out the few large (>50μm) solid particles that might get passed the KREY and that might block the jets of the spinneret directly. Secondly, it smears out the spin mass in a homogeneous way.

Table 2.2: Dimensions of the DHS filter

Filter	Mesh spacing [mm]	Wire thickness [mm]
Fine	0.035	0.030
Coarse	0.200	0.125

2.2.3.3 Düse Einlege Sieb Filter (DES)

The third and final filter is called *Düse Einlege Sieb* (ELS) and also has a quadrature mesh spacing of about 75μm and a wire thickness of 53μm. Again this mesh spacing is larger than the two previous filters. This filter is not used for taking out solid particles, but only for making the flow and temperature over the spinneret more homogeneous.

2.2.4 Spinneret (D)

The Lyocell fibres are created at the spinneret. This is a large ring with about 70.000 small holes (jets) in it, each with a diameter of about 100 μm, depending on the final product. These small jets are very sensitive to dirt particles in the spin mass, hence the use of three filters. As the spin mass is pressed through this ring with a velocity of about 0.5m/s, single cellulose fibres of diameter 100μm are formed. These are immediately drawn through the spinning bath where the last bits of NMMO are washed out and the fibres are cooled down from the operating temperature of 110°C to about 30°C. A sketch of the dispenser holes above the spinneret can be seen in figure 2.8.

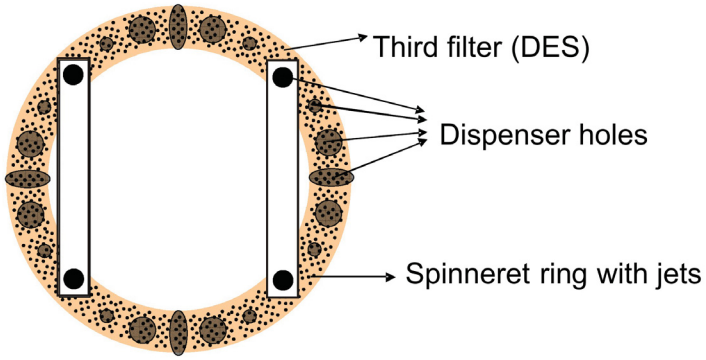

Figure 2.8: Top view of the section between the dividing ring (dispenser holes) after the DHS filter and the spinneret

2.2.5 Cellulose II (E)

After the fibres have been washed in the spinning bath, there will be about 20% NMMO left in the cellulose mixture and little water. This cellulose II is more fibre-like than the cellulose I phase.

Depending on how good the cellulose is dissolved, its physical properties change. Pure cellulose has a density of 1.54gr/cm^3. Pure NMMO has a density of 1.14gr/cm^3. The mixture has a density that depends on the amount of NMMO in it and lays usually around 1.2gr/cm^3. The viscosity strongly depends on the history of the spin mass [28, 59].

2.2.6 Cutting, drying and wrapping (F)

Finally, strands of continuous filament fibres are twisted together to form a continuous filament yarn, which is then woven or knit into fabric or the filaments are collected in a large bundle called a *tow* containing a large number of continuous filaments. The tow bundle is then crimped and mechanically cut into staple fibres to provide a fibre material which, after being dried, can be processed in much the same way as cotton.

2.3 Real Production Process

The ideal process is understood fairly well and no blocking of the process would occur using the spinning method as described in section 2.2. However, blocking of the spinneret and hence a malfunctioning production of Lyocell fibres is seen in periods as small as 40 to 50 hours. This section describes where these imperfections come from and what parts of them are not yet fully understood.

2.3.1 Cellulose Solution - Dope

Basically, cellulose is nothing more than wood pulp. This wood comes from trees that are cut down somewhere in the world, mainly from countries as far as Brazil or Russia. Imagine cutting a tree in the rain forest of Brazil and the time it takes to get this tree in Europe where it can be cut to wood pulp. A lot can happen with the tree in the mean time. Ants or termites can nest inside the tree, even before it is cut down, transporting sand and other minerals inside the wood structure. Transporting the tree through the jungle or overseas can contaminate the wood even further. Finally, the tree is cleaned, but it should be clear that microscopical particles can not all be removed by a coarse cleaning of the tree. All these factors can cause microscopical dirt particles to remain in the final cellulose I pulp, which can cause major problems at the KREY filter and the spinneret with its 100μm jets.

At the same time, cellulose is one of the most difficult materials to dissolve, due to its complex structure. NMMO is capable of dissolving cellulose directly, but in reality some wood pulp might still exist in the dope as well as a lot of by-products of the NMMO-cellulose system [62]. This badly dissolved cellulose might form gels that again do not damage the final product, but might cause trouble at the spinneret.

2.3.2 Gel Particles

The gels, as discussed in the previous paragraph, can be considered as a deformable mass rather than a real liquid due to the complex chemical network of molecules the cellulose-NMMO mixture consists off [49, 59]. Two basic theories

exist on the origin of gels as seen from an experimental and a theoretical point of view.

From the experimentalist point of view, the gels consist of exactly the same material as the cellulose mixture. However, the cellulose chains in the gels are locally more connected than in the rest of the spin mass. This way, the density locally rises. The reason for this macroscopic clustering is that cellulose is not homogeneous, as wood is not homogeneous. This also has to do with the solution state that might not be homogeneous throughout the spin mass. Other extreme statements to this theory are that the gel solution is not a solution, but rather a weakened cellulose and that the solution does not take place at molecular level, but only on macroscopic level.

A theoretical view says that the native cellulose I consists of aligned molecular chains. Only the NMMO can penetrate between these chains and hence dissolve the cellulose. However, this is not a straight forward process as for example the dissolving of sugar in water. The dissolving is not always homogeneous which causes local higher concentrations of cellulose to persist inside the solution. Cellulose chains break up in smaller cellulose pieces during the dissolving. During the break up, caused by an overpressure inside the chains caused by the penetrating NMMO, cellulose and NMMO can get pressed into the remaining smaller cellulose pieces. This way, the concentration of cellulose inside these pieces rises from about 12% to 18%. Due to this higher concentration of cellulose, no further NMMO can penetrate the cellulose pieces and hence these pieces can no longer dissolve. It looks as if the undissolved cellulose is protected by a film that keeps the NMMO out. These undissolved pieces of cellulose behave like solid pieces of wood and can cause the filters to block. This agrees with the experimentalist view of organic pollution [9].

Basically, there are two gel types present in the Lyocell process, i.e. the primary gel and the secondary gel [11]. The primary gel is created at the beginning of the Lyocell process and originates from a bad impregnation. It has practically the same properties as the cellulose mixture and can be created deliberately for further investigation and experiments. The secondary gel is created inside the

Lyocell spinning process. It is a primary gel that accumulates dirt and other particles during its path through the complete process. It has a darker colour than the primary gels and might have different properties than the cellulose mixture, depending on the dirt captured in it. The secondary gel is more difficult to create in a controlled manner.

2.3.3 Solid Particles

As discussed in paragraph 2.3.1, the cellulose pulp might contain quite some solid particle at micron dimensions. Particles up to 20μm should be taken out by the KREY filter or the DHS filter. The fact that blocking is seen and that large (>50μm) particles are found on the DES filter and inside the spinneret means that these filters do not function perfectly.

Due to the quadratic woven meshes of both the KREY and the DHS filter, larger particles than the finest mesh spacing will pass, i.e. $\sqrt{2}$ times mesh spacing. Also, particles with two dimensions smaller than the mesh spacing, can still pass the filter even though the third dimension might be much larger than the mesh spacing. Two other phenomena that are considered possible at the KREY and DHS filter might cause larger particles in three dimensions than the mesh spacing to pass the filters, i.e. *leaking* and *breathing* [9]. The DHS filter simply lies on top of the dispenser and is not connected to the side. This way, due to local high pressures on the filter, the filter might lift up at its borders hence letting large particles pass. Local damages in the woven structure might also diminish the filter function. The KREY filter has to withstand pressures up to 100 bar. Due to these high pressure on the filter, the very thin metal wires inside the filter are being pressed away and towards each other, which makes it look as if the filter is breathing. Because of this breathing, the mesh spacing is not constant and larger particles than the standardized filter mesh might pass the filter.

This section on the real Lyocell process made it clear that both the system with its filters as well as the used ingredients (cellulose, gels and solid particles) must be studied in more detail before the actual situation can be studied and optimized.

Chapter 3

Basic Ingredients

In chapter 2 the Lyocell process has been described. In order to understand the process better and to find the optimization potential, experiments and tests on the basic ingredients of the process have been be conducted. This chapter describes all the conducted experiments on the dope, the gels and the solid particles as well as the digital reconstruction of the KREY filter.

3.1 Dope

The cellulose-NMMO-water mixture or dope shows a very complex rheological behaviour, also called viscoelastic behaviour. This behaviour has been studied in great detail by Mr Markus Gruber as part of his PhD study [28]. The dope at operating temperature of 110℃ behaves similar as cold honey. Its behaviour is non-Newtonian in that its viscosity depends strongly its history and local stress and strain conditions.

In contrast to purely viscous fluids where Newton's law of viscosity is applicable to relate fluid stresses and flow kinematics, viscoelastic fluids obey no such law although several constitutive equations are available. The ones most suitable for the behaviour of the dope have been studied in Mr Grubers PhD and can be summarised in one equation as

$$F_d(\tau).\tau_{ij} + \lambda_0 \left[\frac{\delta \tau_{ij}}{\delta t} + u_k \frac{\delta \tau_{ij}}{\delta x_k} - \tau_{kj} \frac{\delta u_i}{\delta x_k} - \tau_{ki} \frac{\delta u_j}{\delta x_k} \right] + \lambda_0 F_c(\boldsymbol{\tau}, \boldsymbol{D}) = \mu_0 D_{ij} \quad (3.1)$$

where the subscript *0* denotes the constant, linear viscoelastic material functions obtained in the limit of infinitesimal small strains. The influence of the introduced terms F_d and F_c can be described as [28]:

- $\boldsymbol{F_d}$ The relaxation time of the model as a function of the viscoelastic stress tensor.
- $\boldsymbol{F_c}$ This term alters the rate at which stress builds up and can be a function of both the stress and rate-of-deformation tensor.

Depending on the specific definition of the terms F_d and F_c several viscoelastic models can be derived from equation 3.1 including the well-known Phan-Thien Tanner (PTT), Giesekus and in the limit of small strains the Upper Convected Maxwell (UCM) model [28].

Model	$\boldsymbol{F_d}$	$\boldsymbol{F_c}$
UCM	1	0
PTT linear	$F_d = 1 + \frac{\epsilon \lambda_0}{\mu_0} \mathrm{Tr}\boldsymbol{\tau}$	$F_c = \frac{\xi}{2} \left[D_{ik}.\tau_{kj} + \tau_{ki}.D_{jk} \right]$
PTT exponential	$F_d = exp\left(\frac{\epsilon \lambda_0}{\mu_0} \mathrm{Tr}\boldsymbol{\tau} \right)$	$F_c = \frac{\xi}{2} \left[D_{ik}.\tau_{kj} + \tau_{ki}.D_{jk} \right]$
Giesekus	1	$F_c = \frac{\alpha}{\mu_0} \{\boldsymbol{\tau}.\boldsymbol{\tau}\}$

(3.2)

It should be clear that the behaviour of the dope mass is very complex. Since the main focus of this thesis is to optimize the filters in the system, rather than to study the dope, no further attention has been given to the viscoelastic behaviour of the dope.

3.2 Gels

No exact theoretical definition of the existing gels in the dope exists and describing these gels in mathematical models is therefore quite a challenge. In order to obtain a better understanding of the gel behaviour and some basic properties, two experiments were conducted.

The first experiment studies the relation between the presence of primary gels in the cellulose mixture and the pressure rise over the jet filter. The second experiment visually studies the propagation of gels in the dope.

3.2.1 Pressure rise over filter due to gels

In the following paragraphs, the testing range is described, the experiment is explained and finally, the results of this experiment are briefly discussed.

3.2.1.1 Description of Testing Range

In the testing range (figure 3.1), an undissolved cellulose-NMMO-water mixture is inserted. This mixture is heated at a pressure of 5 bar and mixed for at least 40 minutes in order to create the spin mass. Due to a high water percentage, the cellulose does not dissolve completely, which causes gels to arise [17].

The testing range consists of a rod that can move slowly into a chamber containing the mixture. This causes the pressure in the chamber to rise. Underneath the chamber, a filter can be installed above a jet configuration. For this particular experiment, filters of 5μm and 25μm are used and only one jet with a diameter of 1mm exists at the outlet. Note that a very coarse filter is placed underneath the fine filter in order to enforce the fine filter and prevent it from large deformations.

Once the mixture is prepared, the pressure in the testing range is gradually raised by lowering the rod and hence pressing the mixture through the filter and the jet. Note that the testing range can take up a maximum pressure of 105 bar. The maximum operational pressure difference over the jets in the Lyocell process is 60 bar. For higher pressures, the jets might deform.

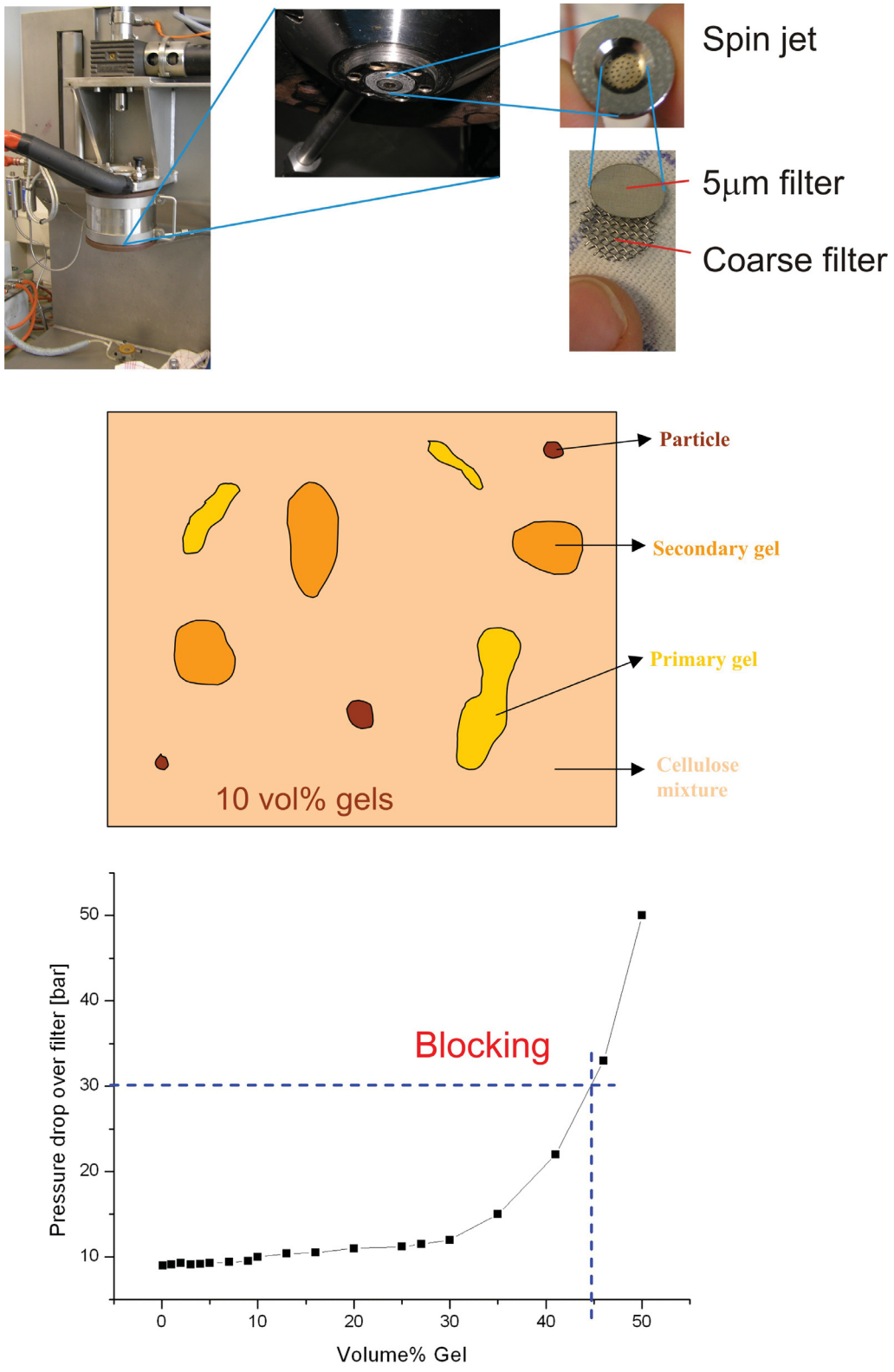

Figure 3.1: Testing range (top) with details of spin jets and filters, sketch of dope containing solid and gel particles (middle) with estimate of pressure rise due to gel particles (bottom)

3.2.1.2 Experiment

The mixture used in the Lyocell process consists of different kinds of cellulose, the solvent NMMO and H_2O. The ratio of each material decides if the solution is good (no gels) or bad (gels). The exact ratios used for this experiment can be found in table 3.1.

The high water percentage in the mixture causes the cellulose to dissolve badly by the NMMO and hence gels (undissolved cellulose) will occur in this mixture. All the gels created here are primary gels.

Table 3.1: Mixture ratios for experimental dope

Material		%	%
Cellulose		11	
	Low molecular (<300 DP)		85
	High molecular (>1200 DP)		15
NMMO		75	
H_2O		14	

During one hour, the mixture is pressed slowly through the filter and the jet. It is assumed that the gels do not flow as easy through the filter as the pure cellulose, hence causing the filter to block. This causes the pressure over the filter to rise.

At several pressure levels (10 bar, 30 bar and 50 bar), samples of the mixture at the outlet of the jet are taken. These samples are then studied under a microscope in order to look at the gel percentage after the mixture has passed the filter.

Figure 3.2 shows a photo of the mixture leaving the jet at the testing range. Note that the fibre leaving the test range has no smooth surface. For a good dissolved cellulose mixture, this should be the case. The rough surface comes from air bubbles that burst at the exit of the jet or gels.

3.2.1.3 Results

Pressure Graph Figure 3.2 shows a a graph showing the pressure over the filter in time. It can be seen that the pressure over the filter rises enormously. For the 5μm filter, the pressure rises even so high, that the filter was torn.

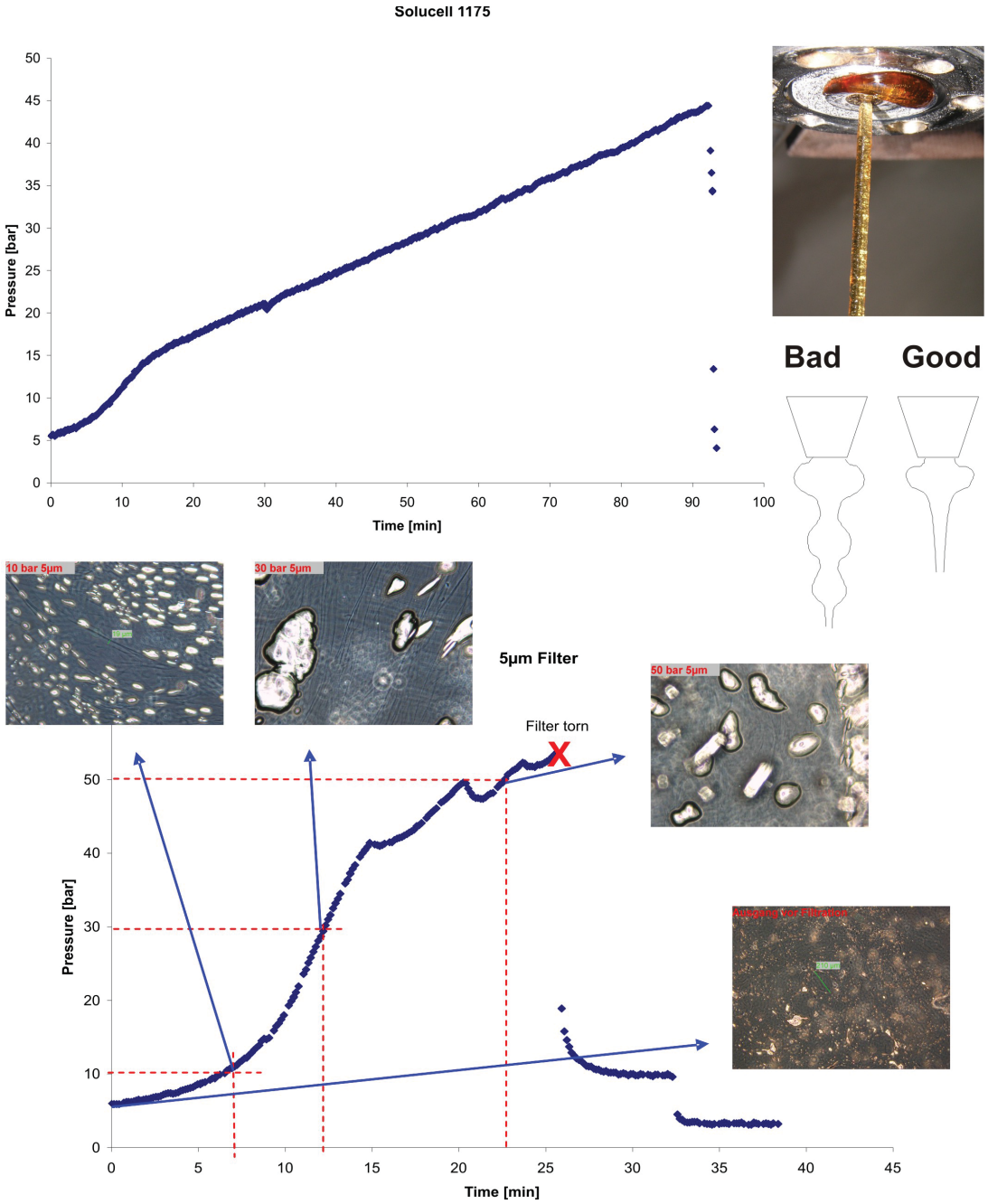

Figure 3.2: Detail of dope at jet outlet (top right) and a graph showing the pressure rise for a clean cellulose mixture (top left) and a mixture containing a lot of gels (bottom) with optical microscope images of samples taken at 10, 30 and 50 bar.

Comparing these results to the pressure rise over a filter using a good dissolved mixture indicates the influence of the presence of gels. For a good dissolved mixture, the pressure also rises over the filter, but far slower and less dramatic as for the mixture containing gels. It can therefore be concluded that the gels play an important role in the blocking of the filters, although this blocking is not sudden as it might be for solid particles, but more gradually.

Visual Results Using a microscope with polarized light and a phase microscope, images of the Lyocell mixture are made at several moments in time during the experiment. The idea was to generally look at the state of the gels in the mixture and more in detail, to estimate the gel percentage in the mixture before and after the filter.

Figure 3.2 shows the pressure graph for the 5μm filter with images of the state of the mixture before the filter, after a pressure rise of 10 bar, 30 bar and 50 bar.

One of the major events that could be seen was the aligning of the gels in the direction of the flow. It can be seen in figure 3.2 that less gels exit the testing range at the a steep pressure rise over the filter. It was assumed that most gels got passed the filter, nevertheless with a delay due to their viscous (sticking) properties, hence increasing the pressure over the filter.

This experiments showed a clear influence of the presence of gels on the spinning process. Due to the gels, the pressure rises dramatically over the filters which might even torn the finer filters.

3.2.2 Control Window

The cellulose plant contains a cell where the cellulose solution passes through a narrow glass plate (*control window*) that is filmed . Here, the quality of the solution can be checked.

A cellulose solution with a lot of gels has been sent through the plant. This way, a lot of gels passed the control window, which has been filmed. Because all boundary conditions (flow velocity, cell size, amount of gels, size of gels) were

known to a fairly good extend, the situation could be simulated. Results and conclusions are discussed in chapter 6.

The dimensions of the control window in the film are given in figure 3.3. The mass flow through the cell was approximately 0.48g/min. Note that due to the very low dimension in height (71μm), wall effects become very important [30].

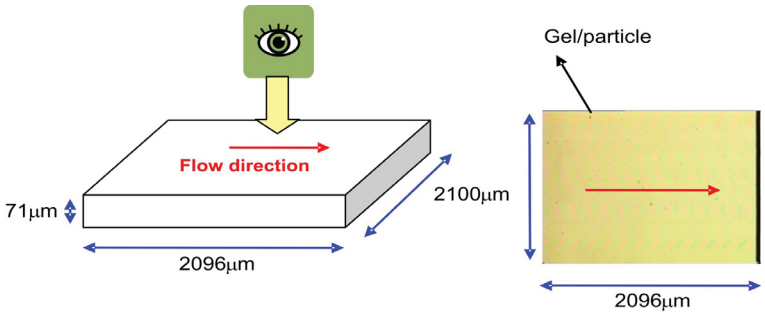

Figure 3.3: Sketch of the control window experiment

3.3 Particles

In order to get a deeper insight in what the solid particles in the dope are and how they can block the jets or the filters, some basic investigations were conducted. First, blocked filters are studied using several microscopic techniques (see appendix A). Second, a large scale experiment has been set up to study the behaviour of solid particles inside the complete Lyocell process.

3.3.1 Optical Microscopy (OM)

Originally it was thought that only sand or quartz (SiO) particles are present in the Lyocell dope (see paragraph 2.3.1). Also, these particles are considered to be smaller than 50μm due to the filtering by the KREY and the DHS filters. Since all jets are at least 100μm in diameter, these quartz particles should not cause any trouble at the spinneret.

In order to study these assumptions, used DHS and DES filters have been ashed (burned) and their remains have been investigated under an optical micro-

scope. A few images seen through the microscope are summarized in figure 3.4.

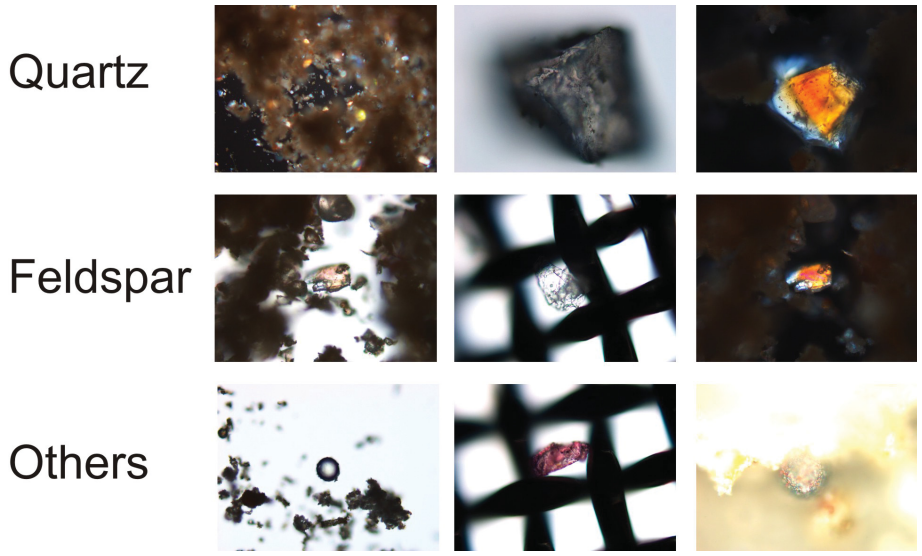

Figure 3.4: Typical examples of quartz, feldspar and other particles found in the ashed and dirty DHS and DES filters

After the optical microscope investigation of the ashed DHS and DES filters, it became clear that the original assumptions were not entirely correct.

First of all, abundant particles larger than 50μm were seen. These particles prove that the KREY and DHS filter do not function optimally and that solid particles can cause blocking at the 100μm diameter jets.

Secondly, as can be seen in figure 3.4, quite a lot of different organic and anorganic particles are present, such as wood, feldspar and glassy elements. These minerals can react with each other or even dissolve, depending on the acidity of the dope. In an acidic environment for example, $CaCO3$ will dissolve. In a basic environment with a pH >10, silicates can dissolve [40, 41, 46].

Note that the glassy particles are probably not natural, but they are more likely the result of burned (ashed) clay minerals. The quartz particles are the only minerals that will not be affected by the ashing of the filters, nor by the acidity of the environment. This is probably the explanation why, after ashing

the filters, quartz minerals are seen abundantly and hence it has been thought that only quartz particles are present in the dope.

In order to rule out the vanishing of minerals present in the dope due to ashing, a second microscopic method has been applied to investigate the used filters directly without ashing them, i.e. Raman spectroscopy.

3.3.2 Raman Spectroscopy (RS)

Raman spectroscopy is a good alternative to optical microscopy when looking at the mineralogical properties of even the smallest particles captured inside the cellulose. Raman spectroscopy is a spectroscopic technique used in condensed matter physics and chemistry to study vibrational, rotational, and other low-frequency modes in a system (see appendix A).

For the experiments on the used DHS and DES filters, the used laser is an Argon 532nm laser (green light). The energy that is transported onto the surface is about 30mW. The enlargement (or focus) was set to 100x. Both enlargement and excitation energy made it possible to look into the cellulose up to a depth of 0.3mm [12].

Figure 3.5 shows the results of some measurements at random positions on the filter parts. The Raman spectrum of cellulose was determined. The minerals quartz and feldspar have been identified by standard spectra of the pure minerals.

It can be concluded that the minerals inside the cellulose can be identified using Raman spectroscopy. However, Raman spectroscopy has some limitations concerning the investigation of the dope:

1. Using Raman spectroscopy for opaque minerals caused the cellulose surrounding the minerals to burn. This can be explained by the fact that opaque minerals can adsorb the incoming energy and heat up really swift. The molten cellulose around such an opaque mineral shows the spectrum of glass.

2. If the particles are too deep inside the cellulose, it is not possible to detect them using the Raman spectroscopy, simply because the excitation energy is not high enough.
3. The intensity of the peaks depends on the orientation of the crystal inside the cellulose.

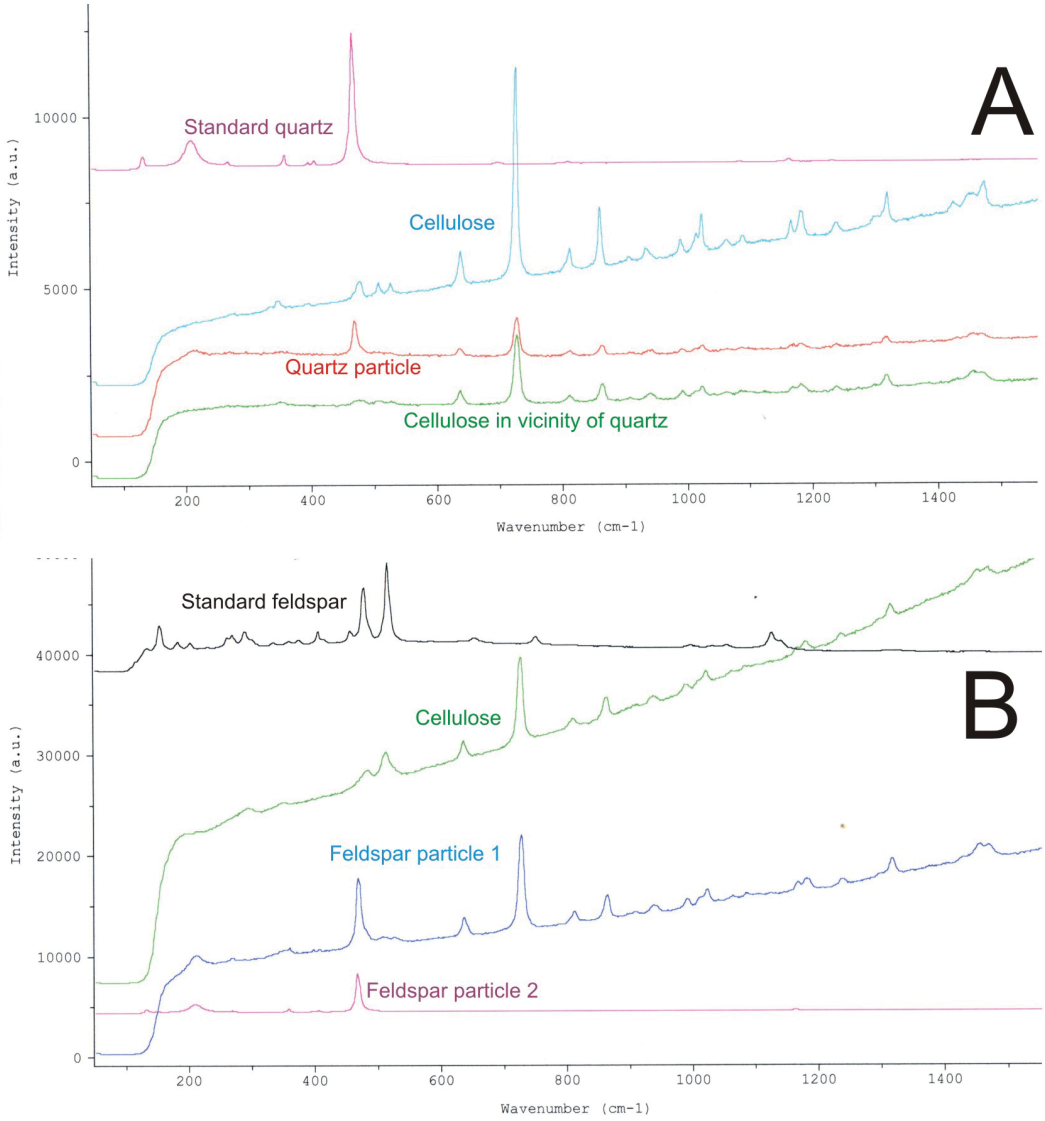

Figure 3.5: Raman spectrum for pure cellulose, cellulose in the vicinity of quartz, a quartz particle and standard quartz (A) and standard feldspar and two different feldspar particles in the cellulose (B)

3.3.3 Scanning Electron Microscopy (SEM)

Using a Scanning Electron Microscope (SEM), the particles can be looked at optically up to a μm scale. The maximum height difference that can be measured by the SEM is 15μm. This way, the surfaces of the solid particles can be studied. Also, the chemical composition of each particle can be measured. All measurements must be performed at room temperature.

Probes from both the ashed DHS and DES filters have been investigated to study the particle morphology as well as the chemical composition of the particles. Figure 3.6 shows a typical result for the solid particles on the DHS and DES filter. Looking at both probes, it was clearly seen that a lot of particles were larger than 50μm. Most real particles have a rod like or plate like morphology, rather than an ideal spherical one. Most particles consist of silicon (Si), however, iron (Fe) and calcium (Ca) elements have been found as well. The iron could be an abrasive by-product from the Lyocell plant rather than part of the dope mixture.

Note that the particle distribution on the DHS filter is far more continuous than that of the DES filter. Also, more particles were found on the DHS filter. As will be explained in chapter 7, this is a consequence of the filter size and structure.

The microscopy experiments clearly showed that larger particles than allowed (>50μm) are present in the vicinity of the spinneret. Also, quartz is not the only mineral present and other minerals can cause other interactions between the plant, the dope and the gels or the particles amongst each other. In order to check whether these particles actually travel from the start of the process (wood pulp) through the KREY, DHS and DES to the spinneret, a large scale doping experiment of the Lyocell plant has been conducted. This is described in the following paragraph.

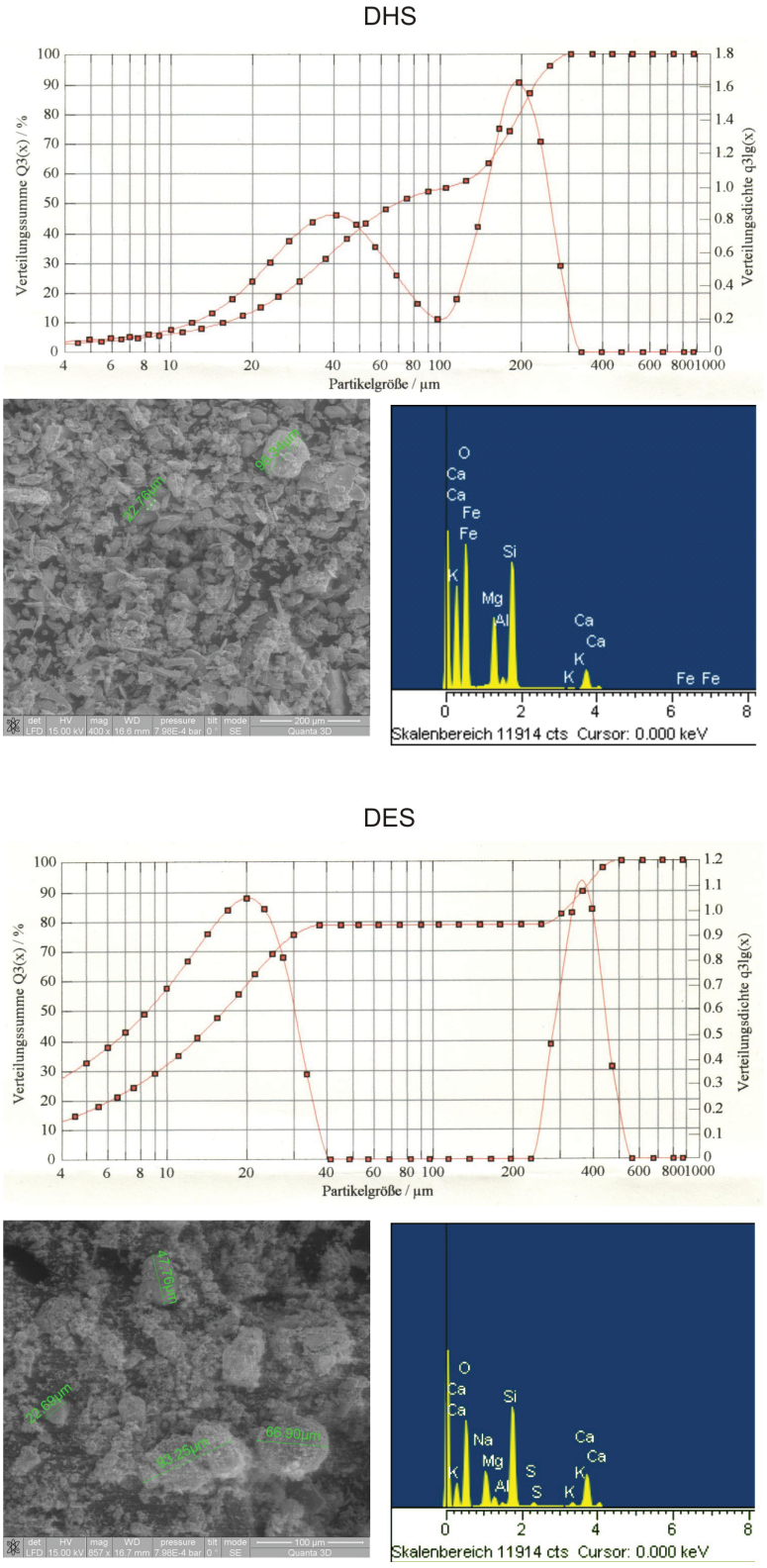

Figure 3.6: Particle size distributions for DHS (top) and DES (bottom) together with examples of SEM images and the compositional spectrum

3.3.4 Doping experiment

In order to get a more basic understanding of the cause of the blocking of the filters in the Lyocell plant, one fundamental experiment has been conducted. This experiment deals with the influence of solid particles in the dope on the permeability of the filters in the Lyocell plant. In theory, all the particles larger than the filter meshes should be stopped at the filters:

- KREY at the start of the spinning process, quadratic mesh of 15μm
- DHS after the dividing ring, quadratic mesh of 35μm
- DES right before the jets, quadratic mesh of 64μm

Hence only very small particles ($<\sqrt{2}.15\mu$m) should reach the jets at the end of the spinning process. These small particles can not cause any blocking, unless they agglomerate to form larger particles that can block a jet (see chapter 4).

However, microscopic investigations showed that very large particles (larger than any mesh in the system) are present at the DHS and DES filter. These large particles might cause direct blocking of the filters or even the jets in the spinneret.

It has been decided to mix tracer particles inside the dope to see where these particles are caught or how far they can travel through the Lyocell process. These tracer particles should be easy to find inside the filters or in the end product and must be easily distinguished from any other particles after the experiment. They should not react with the NMMO-cellulose mixture and they should be injected in different size fractions.

There has been looked at different possibilities for tracer elements. From the Raman experiments (section 3.3.2) it became clear that the dope is not fluorescent. A tracer that is fluorescent might be easy to find on the filters and in the end product. Commercial fluorescent tracer particles can be obtained, but are very expensive. A natural fluorescent mineral, scheelite , is also fluorescent and was available at the Montanuniversity of Leoben (MUL). The raw material was donated by the mine Mittersill and was refined at the MUL by Mr Bouwman.

3.3.4.1 Scheelite

The company Mittersill handed over 18 kg of scheelite ($CaWO4$) concentrate, containing up to 45% $CaWO4$. In order to use this scheelite as a tracer in the Lyocell plant of the company Lenzing AG, it needed to be purified (processed). This was done at the MUL as described in [16].

Mineralogy of scheelite The scheelite mineral has a tetragonal crystallography. It has a white colour and is translucent. Scheelite will fluoresce with blush white colour in short ultraviolet radiation (UVC). It has a high specific gravity [40].

The security risks of the scheelite particles in the cellulose mixture have been conducted by Lenzing AG. It was assured that the scheelite causes no safety risks when doped in the cellulose.

Refining of scheelite Using a combination of different refining techniques, the 18 kg or raw scheelite were reduced to about 2.5 kg of 99% pure scheelite. Figure 3.8 sketches the complete refining process as well as the exact quantitative intermediate and end products of the refining [16, 47, 48]. In total, three scheelite fractions have been created, each fraction representing the spacing of a filter mesh.

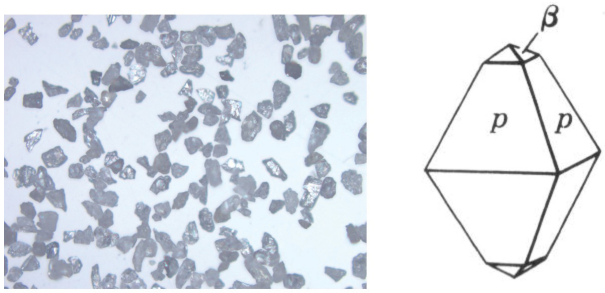

Figure 3.7: Purified scheelite, fraction 32-71μm, 1:100, image width 1.77mm (left) and a sketch of the scheelite crystal, dipyramids (right)

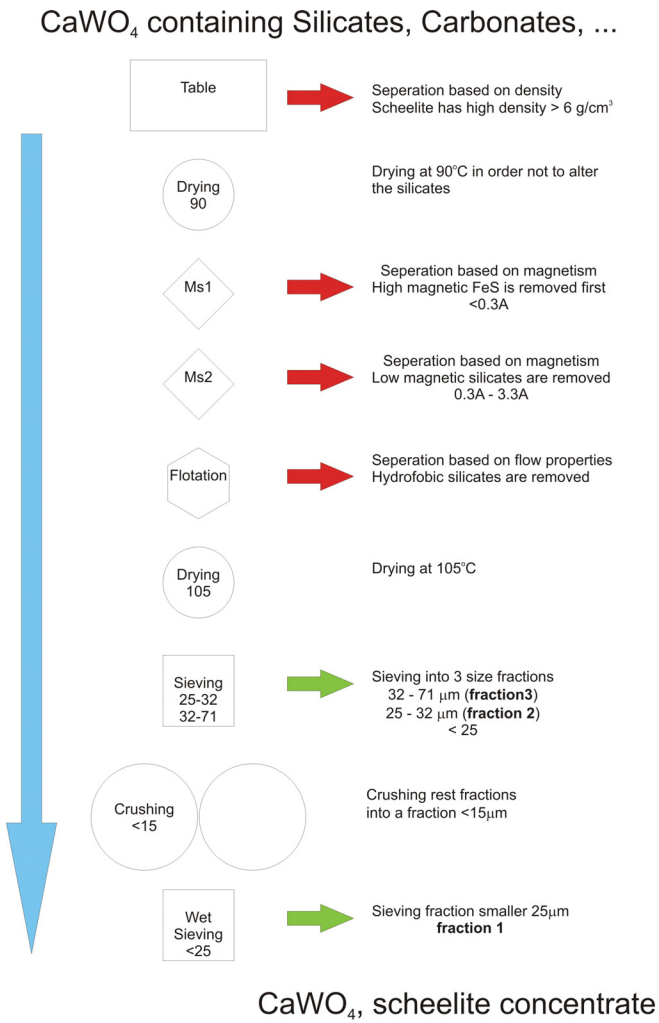

				Mass [g]	Density [g/cm3]	Percentage [%]
	Table					
Concentrate	**MS1 & 2**					
Scheelite		B1	< 0.3A	55.75		0.3
			0.3 – 3A	73.90		0.4
			> 3A	**1106.00**	5.852	6.1
			Sum	1235.65		6.8
		B2	< 0.3A	70.60		0.4
			0.3 – 3A	136.35		0.7
			> 3A	**1606.00**	5.867	8.8
			Sum	1812.95		9.9
		B3	< 0.3A	107.53		0.6
			0.3 – 3A	161.92		0.9
			> 3A	**2132.00**	5.863	11.7
			Sum	2401.45		13.2
			Sum B1+B2+B3 >3A	**4844.00**		
Berge				12750.00	3.459	70.1
			Sum	18200.05		100
Super conc.	**Flotation**					
Hyper conc.	**Sieving**					
			> 100µm	1899.00	5.7938	45.3
			71-100µm	1253.00	5.946	29.9
			32-71µm	758.00	5.983	18.1
			25-32µm	250.00	5.986	6.0
			< 25µm	30.25	5.99	0.7
			Sum	4190.25		100
	Crushing (65 RPM)					
			0-100µm	1550.00		3 hours
			> 100µm	1550.00		1.5 hours
			Rest > 100µm	640.75		
	Wet sieving					
			< 25µm	2500		
			> 25µm	600		
CaWO4	**Fraction 3**		32-71µm	200	5.98	
	Fraction 2		25-32µm	250	5.99	
	Fraction 1		< 25 (15)µm	2500	5.97	

Figure 3.8: Sketch of the complete processing of the scheelite concentrate (left) and a summary of the processing data (right)

3.3.4.2 Remarks on doping experiment

The three fractions are injected in different concentrations and at different times. The capacity of cellulose mixture used in the test plant should equal the capacity of the actual Lyocell plant, which is 20.000 tons pa. This equals 111 kg/h for the testing plant. This means that an initial dose of 0.05% agrees with 50 gr of scheelite.

Note the order in which the filters are replaced. Only the first two of four KREY filters are replaced during all the fraction injections. The DHS and DES filters above the jets are replaced one by one after each step in the doping experiment. This way, it is possible to study the influence on the filters of each step of the experiment.

Probes of the dope will be taken at four points of the process. The first probe is taken at the KREY filter, the second at the DHS, the third at the DES and the final probe is taken from the final product. These probes will be investigated after completion of the experiment by the use of several microscopic methods as described above. In order to study the actual state of the filters, the probes should be taken with the greatest of care, without the loss of any possible information.

3.3.4.3 Conclusions

The general observations during the experiment can be summarized as follows:

- Fraction 1 ($<25\mu$m) showed a time effect: the longer the doping goes on, the more problems arise. This indicates that small particles can accumulate in the system, hence causing problems after a critical concentration.
- Fraction 2 (25 to 35μm) caused a pressure rise at the KREY filter. However, it is believed that the same problems might arise as for fraction 1, because larger particles than the mesh of the KREY filter seem to get passed the KREY filter. Since the fraction has only been injected for 2 hours (instead of 17 as for fraction 1) it is difficult to confirm this.
- Fraction 3 (32 to 71μm) is practically stopped at KREY. Those that do get passed KREY (by leaking) do not seem to cause any trouble at all further down the process.

One day after the termination the experiment, an abnormal pressure rise over the filters was still detected. This indicates that scheelite particles are still trapped at the filters, although none have been injected any more. This can only mean that the scheelite particles somehow got trapped in dead zones of the Lyocell plant and slowly migrated towards the filters.

In the following paragraphs, the DHS filter, the DES filter, the rejected spin mass and the spin fibres (end product) are studied with regard to the injected scheelite minerals. For the investigations of the filters, symmetry of the system has been assumed. This made it possible to only study the half of the filters in detail. Each filter half has been cut into 6 pieces, according to the first six hours as depicted in figure 3.9. Each hour has then been divided into 64 parts (A1-8 and R1-8) that have been studied in detail. There has been looked at the number and the overall size of the scheelite minerals as well as special events such as other minerals or gel particles.

Little scheelite is found on the DHS filter. The particles that are found are larger than the mesh and should be stopped by the filter. The DHS filter lies on a plate with large holes in it. No high velocity gradients exist on small areas and not many dead zones are created. This is not the case for the DES filter that lies directly above the 70.000 jet inlets of the spinneret. Here, a lot of dead zones and high velocity gradients exist.

Figure 3.10 shows a representative example of a detailed study of a DES filter. The figure on the left hand side shows the location of so called special events. These are locations where other than scheelite particles were found (quartz, gels, etc.). The figure in the middle shows the estimated number of particles in the investigated section. Note that these numbers are estimated and should be looked at qualitatively instead of quantitatively. The figure on the right shows the size of the particles.

It is clear that there are not only preferred locations for particles in general (dark spots in the number figure), but also preferred locations for different size

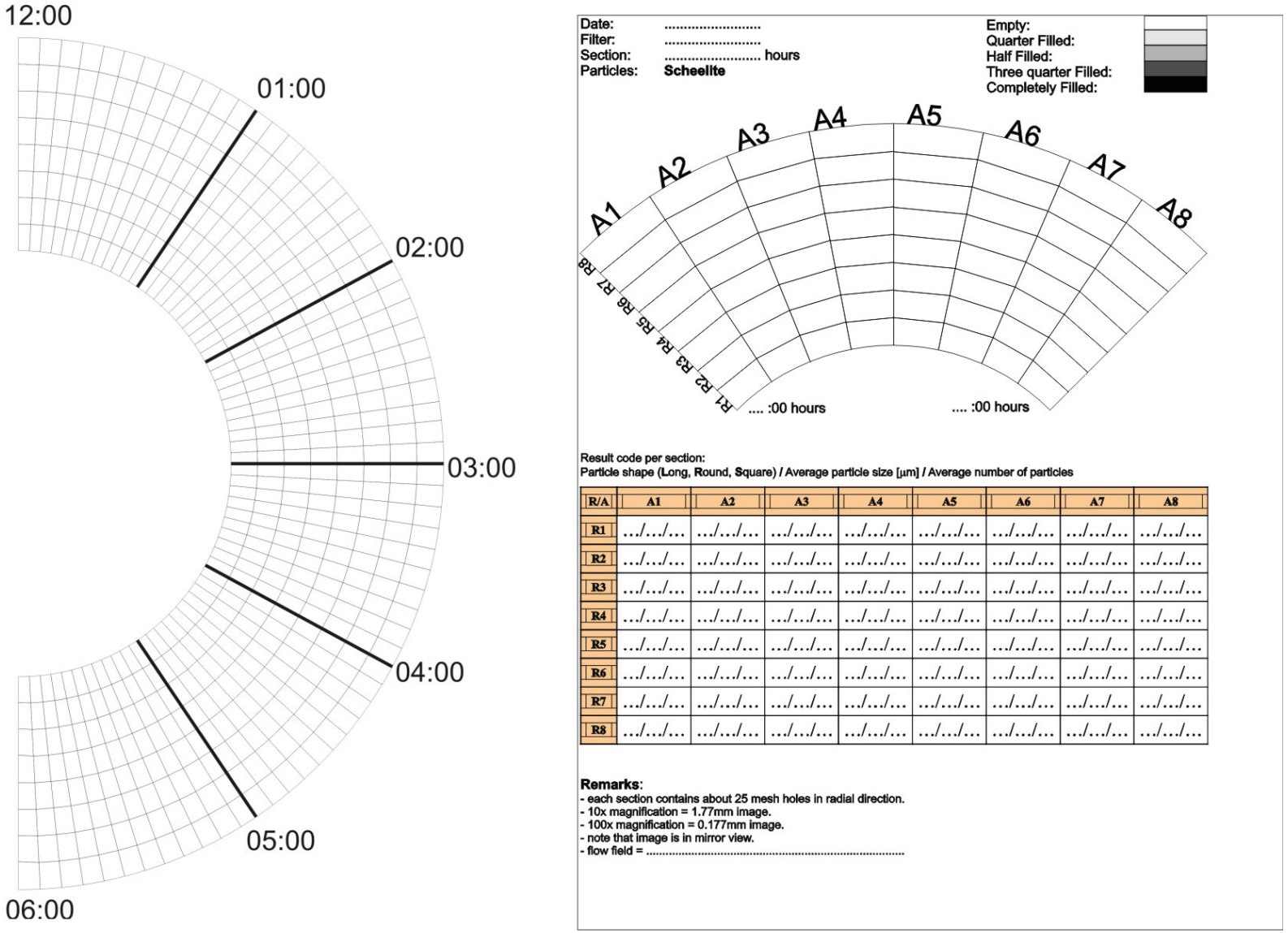

Figure 3.9: Sketch of filter division for the doping experiment

Figure 3.10: Detailed study of the DES filter on special events (A), number of particles (B) and particle size (C). On the right is a sketch of the dividing ring above the DHS filter (D) that imprints a flow pattern on the flow up to the jets which can be seen in the detailed studies.

of particles. This would mean that the deposition of the particles is strongly dependant on the size, the number and the location of particles. It seemed that the flow pattern introduced by the dividing ring above the DHS filter is transported through the Lyocell plant up to the jet inlet (DES filter).

Based on these results, an important conclusion can be drawn regarding the flow pattern above the jets: the flow above and through the DES filter is not homogeneous. This non-homogeneity causes different particles to deposit differently at different locations, hence causing different flow regimes through the jets.

By taking a closer look at the pattern of deposition along the filter, it has been found that the inner rings (R4-7 in figure 3.9) show a more circular deposition around the jet entrance whereas the outer rings show a more linear pattern. This is illustrated in figure 3.11. The linear pattern comes from an irregular flattening of the filter mesh where as the circular pattern comes from a flow driven deposition region.

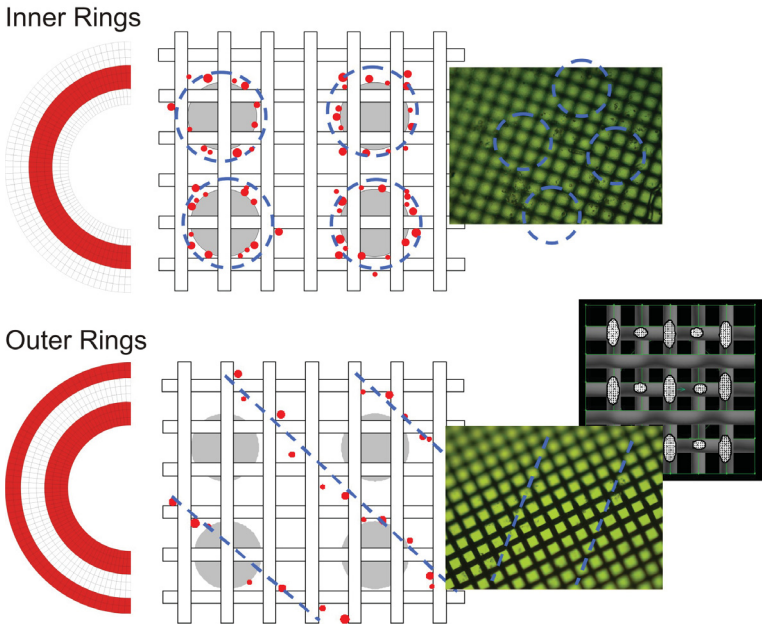

Figure 3.11: Flow patterns in inner (top) and outer rings (bottom), the onset shows a sketch of the irregular flattening of the filter surface

Finally some general remarks can be made for the DES filter:

- There are quite some particles larger than $\sqrt{2}2.35\mu$m present. In theory these should have been stopped by the KREY and DHS filter.
- The deposition of the small particles is mainly underneath the wires of the filter mesh.
- The particles seem to be deposited in different patterns depending on the location of the deposition.
- In the centre of the ring, the particles are deposited in clear groups around the jet holes (circular deposition). At the edges of the ring, the particles are more spread out (line deposition).
- Almost no particles are deposited at the absolute edges of the ring. This could be misinterpreted because of the handling of the filters after they have been taken out of the Lyocell plant but it could also be a sign for the deposition mechanism.

These remarks and conclusions will be tested and verified using Computational Fluid Dynamics (CFD) simulations as described in chapter 5 and 6.

Note that this experiment was aimed at investigating solely the particle blocking. However, gels are always created and present in the system, hence it can not be excluded that they play an important role in the blocking.

3.4 Conclusion

From the elementary studies of the gel and solid particles in the dope, it should be clear that quite some possibilities for blocking of the spinneret are possible. It is very likely that nor the individual solid particles by them selves nor the individual gel particles cause the blocking of the filters, but rather their combination.

In the next chapter, there will be a thorough discussion on all possible blocking mechanisms for both the gels, the solid particles and their combination that will than be tested using CFD simulations in chapter 6.

Chapter 4

Blocking

Based on the experiments described in the previous chapter, theories on possible blocking mechanisms were set up. Basically, two different actors are thought to cause blocking, i.e. the general flow mechanisms and particles.

Still very little is known about the gel particles and it is extremely difficult to have a look inside the Lyocell plant to study the general flow through the plant. It has therefore been decided to develop possible blocking theories that describe the interaction between the dope and the particles as well as the flow over and through the filters and the spinneret. These can be verified using CFD simulations (see chapter 6) in order to find ways to optimize the Lyocell process to prevent blocking.

4.1 General blocking mechanisms

In complex industrial plants where fluids are processed, very often the fluid flow through the plant is not very well understood. The lack of information on the exact flow patterns through the plant might cause a loss in efficiency or even a malfunction of the plant.

The same is true for the Lyocell process, where the fluid flow through the filters and the spinneret is not completely determined. The experiments as described in chapter 3 showed possibilities of how local flow conditions can cause blocking of the spinneret. These are discussed in the following paragraphs.

4.1.1 Flow dead zone

Experiments conducted by Mrs Honeger-Gruber as part of Mr Grubers PhD thesis clearly showed the existence of large recirculation zones between the jets of the spinneret [33]. In these recirculation zones , or so called *dead zones*, particles might get trapped. If a critical amount of particles comes together in such a dead zone, they might get glued together. A large enough clustered particle can move out of the dead zone again, blocking the free path above a jet as illustrated in figure 4.1. These dead zones can occur anywhere in the process where the diameter of the pipes changes abrupt.

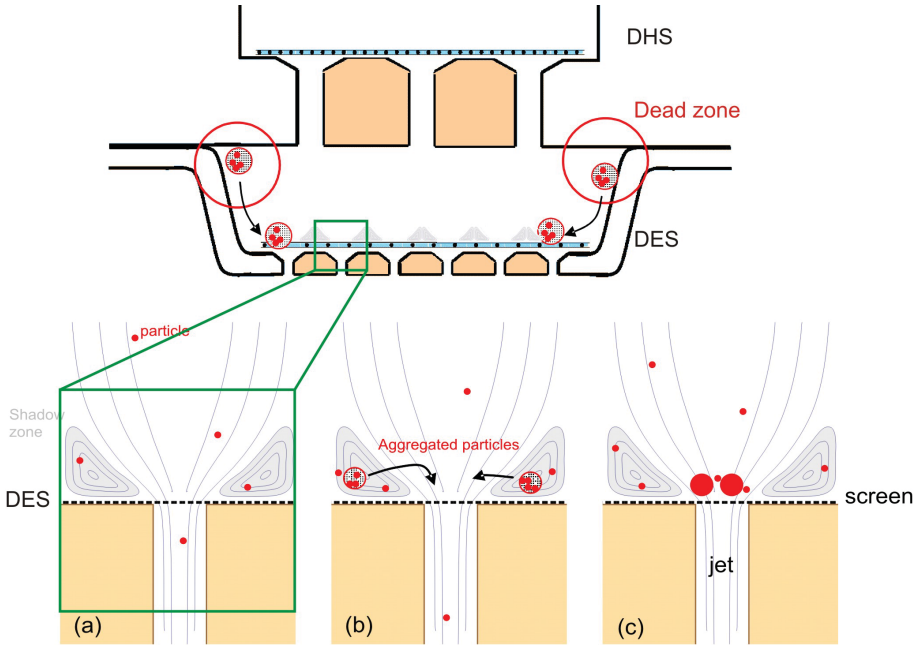

Figure 4.1: Top: Small particles can cluster in dead zones between DHS and DES filters and form larger particles that can block the DES filter. Bottom: (a) Particles in the flow, (b) particles are trapped in the shadow zone and aggregate, (c) large aggregated particle migrates back into the flow and blocks the screen

4.1.2 Static electricity

Very small particles, such as cellulose particles and some mineral particles, are in general negatively charged. Further it is assumed that the gel particles are

positively charged. It is also known that NMMO is a dipole. All these charged elements inside the flow can cause particles to change their charge after which they can aggregate. Note that at the border between two metal types, a potential could exist. This potential might be strong enough to trap these charged particles. Since experiments or verifications of this theory were practically impossible, no further attention has been paid to this theory.

4.1.3 Filter patterns

There were found patterns in the deposition of the scheelite particles. The flow pattern created by the dividing ring above the DHS filter is imprinted in the flow through the Lyocell plant up to the the spinneret, which is proved by the deposition patterns of the DES filter as described in paragraph 3.3.4 (see figure 3.10). Improving the flow through the plant in order to prevent blocking of the spinneret might therefore simply mean improving the dividing ring.

Also, the flow above and through the DES filter is not homogeneous. This non-homogeneity causes different particles to deposit differently at different locations. By taking a closer look at the pattern of deposition along the filter, it has been found that the inner rings show a more circular deposition around the jet entrance whereas the outer rings show a more linear pattern. The flow in the centre of the ring is more homogeneous and uniform causing the dead zones between the jets to be the main deposition factor, hence the deposition around the (circular) jet inlets. For the outer rings, local differences in filter surface are more dominant than the flow trough the jets. The DES filter is flattened (walsed) by the manufacturer, leaving a rough inhomogeneous surface. This roughness causes the flow right above the filter to be aligned along the longer walsed surfaces, hence giving rise to a linear deposition regime and causing the particles to deposit linearly.

4.2 Particles

There are two kinds of particles that can block the filters or the spinneret, gel (fluid) particles and solid particles. Both have their own characterizing influence on the flow through the filters.

4.2.1 Gel particles

Basically, fluid particles dispersed in another fluid do not block the flow. Due to their deformability, they will always flow through any narrow passage or obstruction. However, since the gels have a very clear phase transition with the cellulose solution, the situation slightly alters as soon as the gel particles become a very high surface tension. This can be the case if the membrane, separating the gels from the cellulose dope, is very rigid, i.e. no flux from one fluid to the other.

If gel particles become very small, the surface tension rises as well. At very high surface tensions ($\sigma > 1N/m$), the gels might even behave as solid particles and block the filter structures in the plant. Very small gels might be formed in the dissolving process. However, it is more likely that the very fine KREY filter cuts larger gels into very small ones (1-100μm). This is also illustrated in section 6.4.2.

These practically rigid gels can still deform to a small extend. This way, they can fill up filter meshes or jets, adapt to the shape of the object they fill and then, due to the high surface tension, block that part of the process.

Coagulation of gels is also a process that will take place more easily than the clustering of solid particles. The gels do not need any *glue* to hold them together. Merely the surface tension will do.

Surfactants can stiffen the gels, creating the same situation as high surface tensions. However, gels with stiff surfaces due to surfactants can be larger than those with high surface tensions, causing more trouble in the Lyocell process [2, 51, 64, 66].

Summarised, it can be said that very small gel particles (<10μm) will have a high enough surface tension to behave like solid particles. However, unless they coagulate with other gels (which lowers their surface tension), they do not form any blocking danger for the filters (mesh >30μm) nor the jets (diameter 100μm) (**a.**). Intermediate to large gel particles have a rather normal surface tension ($\sigma = 0.01N/m$). They will deform and be pressed through any kind of filter or jet, possibly with some delay. This delay might cause blocking if solid dirt particles are trapped inside the gel at the same time. However, with only small

amounts of dirt particles present and 70.000 jets, chances are rather small (**b.**). Finally, if intermediate and larger gel particles stay in the system for longer times, they might trap more and more surfactants at their surface. These gels are also called secondary gels [11, 14]. These surfactants might raise the surface tension, hence making the gels less deformable, more rigid). This kind of particles might block the filter or even the jet and cause the Lyocell spinning process to fail (**c.**). These three situations are illustrated in figure 4.2.

Gels cause the pressure to rise over a filter (see section 3.2.1), but they do not block immediately like large solid particles do. In time, the pressure will simply rise too high so that production over the jet slows down dramatically. However, this is not a fast blocking of the jet and can be anticipated on during the spinning process.

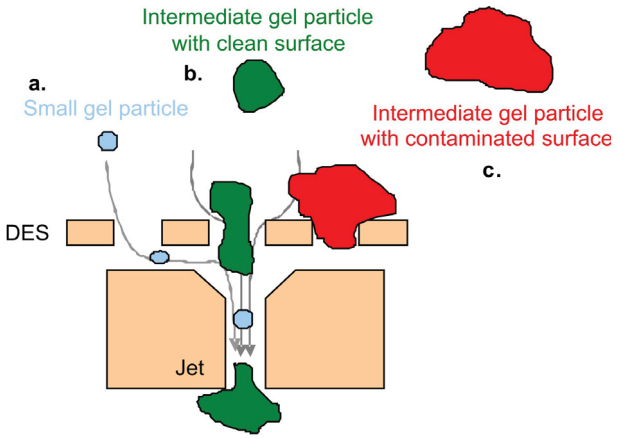

Figure 4.2: Sketch of possible gel-filter interactions

4.2.2 Solid particles

In theory, no larger particles than $\sqrt{2}.15\mu$m should reach the DES filter and the spinneret. The KREY filter should take all larger particles out of the system and these small particles should not cause any problems at the jets of the spinneret (diameter 100μm). However, larger particles have been found on the DHS and DES filters (see section 3.3) and the spinneret does get blocked occasionally by larger particles as is illustrated in figure 4.3.

Only particles larger than the jet opening (agglomerates or single large ones) might cause problems (**A**). These should be filtered out by the KREY or the DHS filter. The high velocity gradients in the flow above the jets make it quite impossible for the particles to agglomerate (**B**). In the shadow zones, particles might aggregate. There is time and the velocity gradients are low. These aggregated particles will not easily migrate out of the shadow zone into the general flow. Even if they might be able to migrate out of the shadow zone, the high velocity gradients at the jet inlet might cause the aggregation to dissolve again (**C**). Statistical chances that particles arrive on exactly the same time at one of the 70.000 jet inlets to cause bridging (**D**) or similar phenomena are very small.

The morphology of the particles also plays a role in the blocking process. An ideal spherical particle behaves different than a real rod shaped or a plate shaped particle (see right of figure 4.3).

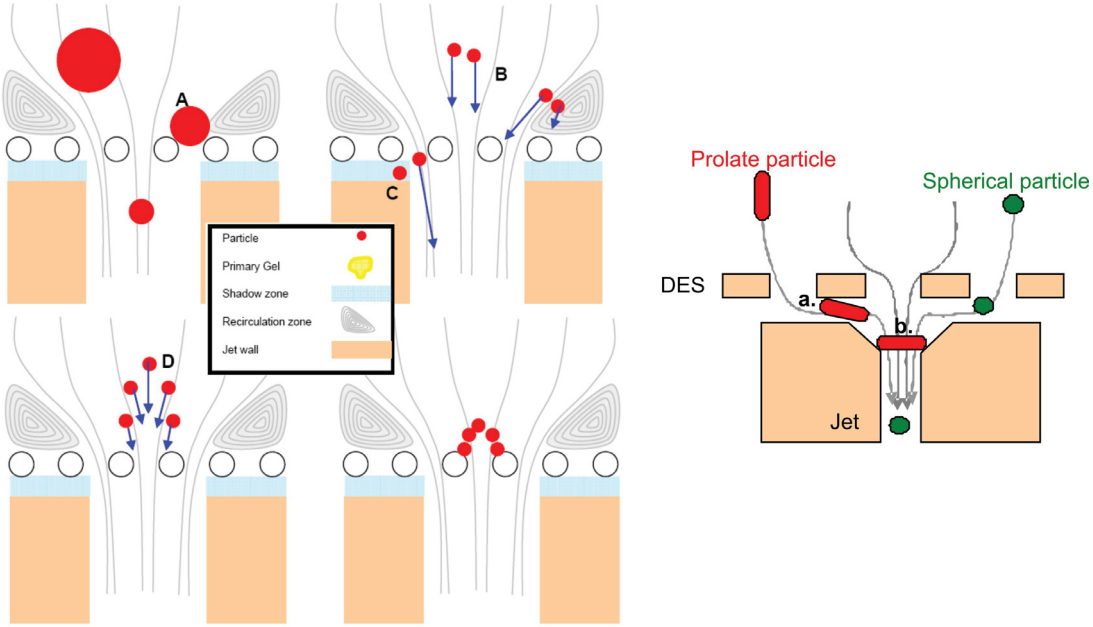

Figure 4.3: Left: Large particles can directly block the jet inlet (A), high velocity gradients make agglomerates unlikely (B,C), bridging is very unlikely (D). Right: Flow behaviour of ideal and real (prolate) particles

Different blocking mechanisms by larger particles (fluid or solid) have clear influences on the spinning product. A large particle blocking only part of a jet causes the spin fibre to bend and maybe even get attached to neighbouring fibres and hence damaging the end product (**1**). If a group of large particles is able to block a large part of the jet, too little spin mass flows through the jet hence causing the fibre to thin out under its own weight (**2**). Finally, if a large particle is able to prevent abundant dope to flow through the jet, the fibre breaks under its own weight (**3**). These three situations are illustrated in figure 4.4. All these effects are seen in the real Lyocell process.

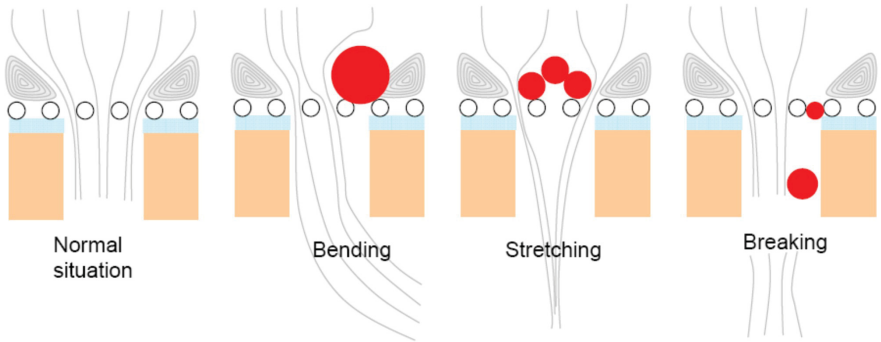

Figure 4.4: Blocking effects of large particles on spinning output: bending, stretching and breaking

Finally, clear differences between the deposition and hence blocking regimes of the DHS and DES filter have been observed during the doping experiment (section 3.3.4). Only a small amount of particles was found on the DHS filter. The flow over the filter is very uniform. There is no dividing ring above it and there are only a few large holes below the filter to let the dope flow into the dividing ring.

The flow over the DES filter is not uniform due to different mass fluxes as prescribed by the dividing ring. This has a major influence on the deposition of particles as described in section 3.3.4.3. Also, a landscape of 70.000 jets after the filter create a lot of dead zones that can trap particles.

4.2.3 Combination

The first serious experiments on how the solid and gel particles in the cellulose mixture can block the filters in the Lyocell plant have shown that both solid and gel particles play an important role. Single particles can only block the filters if they are large enough or if they agglomerate to form larger particles. The particles smaller than the filter and the jet inlet might get deposited at shadow zones, but they will not directly block the Lyocell spinning process. Gels can lower the permeability of filters. However, their effect on the flow is gradual. No immediate blocking is caused by the gels.

After examining the filters used in the solid particle experiment, evidence has been found that a combination of particles surrounded by gels can completely block a jet instantaneously. The particles most likely make the gels more rigid, so that they behave as if they were solid bodies larger than the jet entrance rather than fluids. At the same time, the gels function as glue for the solid particles to form large agglomerates.

It can therefore be concluded that either the single small solid particles or gels do not cause immediate blocking of the filters. However, a combination of the sticky gels and the rigid particles might cause the filters to block instantaneously (see figure 4.5).

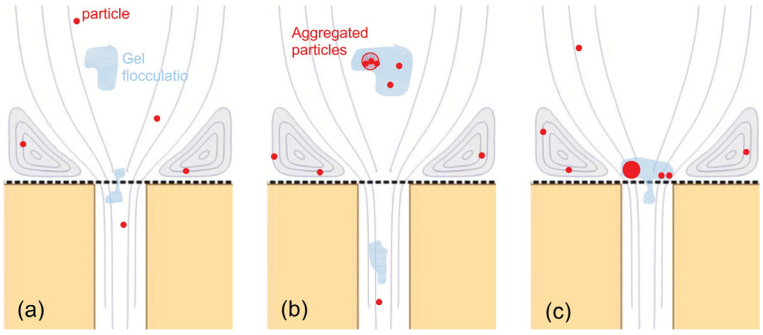

Figure 4.5: (a) Particles and gel flocculations in the flow, (b) particles are trapped in the gel flocculation and might aggregate, (c) gel-particle mixture flows towards the screen and blocks it.

4.3 Conclusion

The above described theories were either constructed on observations made in the experiments or the experiments confirmed what was stated in earlier theories. However, it is difficult to work with experiments alone, since the flow regimes or details are difficult to obtain from the complete Lyocell plant.

Computer simulations such as CFD simulations can help enormously to get a better insight in the situations at hand in order to improve or alter them. It has therefore been decided to use advanced CFD techniques to simulate the stated theories to test their validation.

The next chapter explains the basic theory of CFD as well as some high-end applications. Chapter 6 and 7 show how CFD has been used to study and optimise the Lyocell spinning process.

Chapter 5

CFD

The use of Computational Fluid Dynamics (CFD) makes it possible to study multiphase fluid flows in complex geometries. In order to conduct a CFD simulation, the following tools are needed. A computational mesh or grid that defines the geometry, an algorithm or solver that solves the mathematical equations of the physical situation and a post-processing tool that visualises the simulated results.

In this thesis, the meshing tool GAMBIT has been used to create all the simulated geometries. GAMBIT is a registered trademark of Fluent Inc. For the particular case of the Lyocell process, the phases to be simulated are the dope, the gels and the solid dirt particles in the dope. The mathematical equations that describe the interaction between the dope and the gels are simulated using the so called Volume of Fluid (VoF) method [32, 42]. The simulation of solid particles in a fluid is simulated using the Lagrangian approach.

Basically, any software tool can be used to simulate the VoF or Lagrangian approach. Most commercial software packages, like FLUENT and CFX, have the VoF solver implemented. However, it is difficult to adapt these solvers to specific needs. The Lagrangian particle, also called Large Particle [4, 5], model is not implemented in any commercial code so far. This solver was written by G. Boiger for the Open Source CFD software OpenFOAM [4, 5, 44].

The CFD program OpenFOAM has many advantages over commercial software. It is free available, the source code (C++) can be completely adapted to any wanted situation and it comes with the Open Source post-processing software

ParaView[54]. Both OpenFOAM and ParaView have been used throughout this thesis.

This chapter briefly discusses the software OpenFOAM, the basics of fluid flow and CFD as well as the theoretical background of VoF and Large Particle simulations.

5.1 OpenFOAM

The Open Source Field Operation and Manipulation (OpenFOAM) code is first and foremost a C++ library, used primarily to create executables, known as applications. The applications fall into two categories: *solvers*, that are each designed to solve a specific problem in continuum mechanics; and *utilities*, that are designed to perform tasks that involve data manipulation. The OpenFOAM distribution contains numerous solvers and utilities covering a wide range of problems [45]. One of the strengths of OpenFOAM is that new solvers and utilities can be created by its users with some prerequisite knowledge of the underlying method, physics and programming techniques involved [44].

A central theme of the OpenFOAM design is that the solver applications, written using the OpenFOAM classes, have a syntax that closely resembles the partial differential equations being solved. For example the equation

$$\frac{\delta \rho \boldsymbol{U}}{\delta t} + \nabla \cdot \phi \boldsymbol{U} - \nabla \cdot \mu \nabla \boldsymbol{U} = -\nabla p \tag{5.1}$$

is written directly in OpenFOAM as (highlighted by grey background)

```
solve
(
  fvm::ddt(rho, U)
+ fvm::div(phi, U)
- fvm::laplacian(mu, U)
  ==
- fvc::grad(p)
);
```

This and other requirements demand that the principal programming language of OpenFOAM has object-oriented features such as inheritance, template classes, virtual functions and operator overloading. These features are not available in many languages that purport to be object-orientated but actually have very limited object-orientated capability, such as FORTRAN-90. C++, however, possesses all these features while having the additional advantage that it is widely used with a standard specification so that reliable compilers are available that produce efficient executables. It is therefore the primary language of OpenFOAM [44, 45, 53].

5.2 Fluid Flow

Before turning to specific simulation solvers like VoF, it is appropriate to discuss fluid flow in general and how to simulate it. Here the basic equations governing fluid flow and associated phenomena will be presented. These equations are mainly based on a previous thesis [6], but they can be found in numerous more standard texts on fluid mechanics [25, 35, 44, 55].

5.2.1 Conservation principles

Conservation laws can be derived by considering a given quantity of matter or Control Mass (CM) and its extensive properties, such as mass, momentum and energy. This approach is used to study the dynamics of solid bodies, where the CM is easily identified. In fluids, however, it is difficult to follow a parcel of matter. It is more convenient to deal with the flow within a certain spatial region that is called a Control Volume (CV), rather than in a parcel of matter which quickly passes trough the region of interest. Two extensive properties, mass and momentum, are considered here.

For mass, which is neither created nor destroyed in flows of engineering interest, the conservation equation can be written as

$$\frac{\mathrm{d}m}{\mathrm{d}t} = 0 \tag{5.2}$$

On the other hand, momentum can be changed by the action of forces and its conservation equation is Newton's second law of motion:

$$\frac{\mathrm{d}(m\boldsymbol{U})}{\mathrm{d}t} = \sum \boldsymbol{F} \tag{5.3}$$

Where t stands for time, m for mass, U for the velocity, and F for forces acting on the control mass.

In general it is convenient to approach the conservation principles as follows. If ϕ is any conserved intensive property, then the corresponding extensive property Φ can be expressed as:

$$\Phi = \int_{\Omega_{CM}} \rho\phi \mathrm{d}\Omega \tag{5.4}$$

where Ω stands for a volume, Ω_{CM} for the volume occupied by the CM and ρ for the density of the fluid. Using this definition, the left hand side of each conservation equation for a control volume can be written (Reynolds transport theorem):

$$\frac{\mathrm{d}}{\mathrm{d}t}\int_{\Omega_{CM}} \rho\phi \mathrm{d}\Omega = \frac{\mathrm{d}}{\mathrm{d}t}\int_{\Omega_{CV}} \rho\phi \mathrm{d}\Omega + \int_{S_{CV}} \rho\phi(\boldsymbol{U} - \boldsymbol{U}_b)\cdot\boldsymbol{n}\mathrm{d}S \tag{5.5}$$

Where Ω_{CV} is the CV volume, S_{CV} is the surface enclosing CV, $\mathbf{n}$ is the unit vector orthogonal to S_{CV} and directed outwards, $\mathbf{v}$ is the fluid velocity vector and $\mathbf{v}_b$ is the velocity vector with which the CV surface is moving. This equation states that the rate of change of the amount of the property in the control mass, Φ, is the rate of change of the property within the control volume plus the net flux of it through the CV boundary due to the fluid motion relative to CV boundary [25]. Note that vectors are denoted in **bold** characters.

5.2.1.1 Mass conservation

The integral form of the mass conservation (continuity) equation follows directly from the control volume equation 5.5, by setting $\phi = 1$:

$$\frac{\partial}{\partial t}\int_{\Omega} \rho \mathrm{d}\Omega + \int_{S} \rho\boldsymbol{U}\cdot\boldsymbol{n}\mathrm{d}S = 0 \tag{5.6}$$

By applying the Gauss' divergence theorem to the convection term, the surface integral can be transformed into a volume integral. Allowing the control volume to become infinitesimally small leads to a differential coordinate-free form of the continuity equation:

$$\frac{\partial \rho}{\partial t} + \mathrm{div}(\rho \boldsymbol{U}) = 0 \tag{5.7}$$

This form can be transformed into a form specific to a given coordinate system by providing the expression for the divergence operator in that system.

In many applications the fluid density may be assumed constant. This is true not only for flows of liquids, whose compressibility may indeed be neglected, but also for gases if the Mach number is below 0.3. Such flows are said to be incompressible. In this thesis, only incompressible flows will be considered.In that case, the mass conservation equations reduces to [25]:

$$\mathrm{div}\ \boldsymbol{U} = 0 \tag{5.8}$$

or written in a Cartesian coordinate system as applied in OpenFOAM [44]:

$$\nabla \cdot\ \mathbf{U} = 0 \tag{5.9}$$

```
div(U) ;
```

5.2.1.2 Momentum conservation

There are several ways of deriving the momentum conservation equation. One approach is to use the control volume described in section 5.2.1. In this method, use is being made of equations 5.3 and 5.5 in which ϕ is replaced by $\mathbf{U}$, e.g. for a fixed fluid containing volume of space:

$$\frac{\partial}{\partial t}\int_{\Omega} \rho \boldsymbol{U}\mathrm{d}\Omega + \int_{S} \rho \boldsymbol{U}\boldsymbol{U}\cdot\boldsymbol{n}\mathrm{d}D = \sum \boldsymbol{F} \tag{5.10}$$

To express the right hand side in terms of intensive properties, one has to consider the forces which may act on the fluid in a CV:

- surface forces $\boldsymbol{T}$(pressure, normal and shear stresses, surface tension etc.);
- body forces $\boldsymbol{b}$ (gravity, electromagnetic forces, etc.)

A coordinate free vector form of the momentum conservation equation is readily obtained by applying Gauss' divergence theorem to the convective and diffusive flux terms:

$$\frac{\partial \boldsymbol{U}}{\partial t} + \text{div}(\rho \boldsymbol{U}\boldsymbol{U}) = \text{div}\boldsymbol{T} + \rho \boldsymbol{b} \tag{5.11}$$

where $\boldsymbol{b}$ is the body force and $\boldsymbol{T}$ is the stress tensor, which is the molecular rate of transport of momentum and for Newtonian fluids can be written as

$$\boldsymbol{T} = -\left(p + \frac{2}{3}\mu \text{div}\ \boldsymbol{U}\right)\boldsymbol{I} + 2\mu \boldsymbol{D} \tag{5.12}$$

where μ is the dynamic viscosity, $\boldsymbol{I}$ is the unit tensor, p is the static pressure and $\boldsymbol{D}$ is the rate of strain (deformation) tensor. The corresponding equation for the ith Cartesian component is:

$$\frac{\partial(\rho u_i)}{\partial t} + \text{div}(\rho u_i \boldsymbol{U}) = \text{div}t_i + \rho b_i \tag{5.13}$$

Again, when the fluid density is assumed to be constant, this equation can be simplified. For this thesis, the simulated flows are also isothermal, so the viscosity is constant. If any source terms are neglected, the momentum conservation equation reduces to:

$$\frac{\partial u_i}{\partial t} + \text{div}(u_i \boldsymbol{U}) = \text{div}(\mu \text{grad} u_i) - \frac{1}{\rho}\text{div}(p\ \mathbf{i}_i) + b_i \tag{5.14}$$

where $\boldsymbol{i}_i$ is the Cartesian unit vector in the direction of the coordinate x_i. In OpenFOAM, the source term b_i is neglected and the equation reads as:

$$\frac{\delta \rho \boldsymbol{U}}{\delta t} + \nabla \cdot \phi \boldsymbol{U} = \nabla \cdot \mu \nabla \boldsymbol{U} - \frac{1}{\rho}\nabla p \tag{5.15}$$

```
    fvm::ddt(rho, U)
  + fvm::div(phi, U)
    ==
  + fvm::laplacian(mu, U)
  - fvc::grad(rho, p) ;
```

The continuity and momentum equations are usually called *Navier-Stokes* equations.

5.2.2 Navier-Stokes equations

The simplified equations governing the conservation of mass (equation 5.8) and momentum (equation 5.14) in a viscous, Newtonian fluid were deducted in paragraph 5.2.1 and can be summarized as

$$\frac{\partial}{\partial x_j}(\rho u_j) = 0 \tag{5.16}$$

$$\frac{\partial u_i}{\partial t} + \frac{\partial}{\partial x_j}(u_i u_j) = \frac{\partial}{\partial x_j}\left[\mu\left(2D_{ij} - \frac{2}{3}\delta_{ij}D_{kk}\right)\right] - \frac{1}{\rho}\frac{\partial p}{\partial x_i} \tag{5.17}$$

where u_i is the velocity in the i^{th} direction, p the pressure, ρ the density of the fluid, μ the dynamic viscosity and D_{ij} is the strain-rate tensor:

$$D_{ij} = \frac{1}{2}\left(\frac{\partial u_i}{\partial x_j} + \frac{\partial u_j}{\partial x_i}\right) \tag{5.18}$$

Conservation of energy can be formulated in a similar way, but is ignored in this thesis since all simulations will be considered isothermal. An equation of state and a relationship that gives the viscosity as a function of the other state variables close the system [56]. Possible viscosity models, available in OpenFOAM, will be discussed in the next paragraph.

5.2.3 Viscosity

The complexity of the rheological behavior of the cellulose has already been studied in great detail in the past by M. Gruber [28]. Several very complex viscoelastic

constitutive equations have been implemented and tested, such as the Phan-Thien-Tanner (PTT) and Giesekus models (see section 3.1). To implement these models in OpenFOAM would go beyond the scope this thesis. However, OpenFOAM contains a few more simple viscosity models that can close the previously mentioned Navier-Stokes equations. Standard, the Newtonian model is applied. In this model, the kinematic viscosity is a constant:

$$\nu = \nu_0 \tag{5.19}$$

```
nu_ = nu0_ ;
```

Note that the dynamic viscosity μ is the product of the density ρ with the kinematic viscosity ν, i.e. $\mu = \rho\nu$. For incompressible fluids, the dynamic viscosity is normally used. For generalization of the viscosity models, the definition using the kinematic viscosity is presented here. Two non-Newtonian models for the viscosity are available. The so called Cross Power Law model:

$$\nu = \frac{(\nu_0 - \nu_\infty)}{1 + [\mathrm{m}\dot{\gamma}]^n} + \nu_\infty \tag{5.20}$$

```
(nu0_ - nuInf_)/(scalar(1) + pow(m_*strainRate(), n_)) + nuInf_ ;
```

And the Bird Carreau model:

$$\nu = \nu_\infty + (\nu_0 - \nu_\infty)\left[1 + \sqrt{k\dot{\gamma}}\right]^{\frac{(n-1)}{2}} \tag{5.21}$$

```
nuInf_
+ (nu0_ - nuInf_)
*pow(scalar(1) + sqr(k_*strainRate()), (n_ - 1.0)/2.0) ;
```

With the viscosity ν limited by ν_0 and ν_∞ at high shear rates, m is the consistency index which is a measure of the average viscosity of the fluid, k is a time constant and n is the power law index which is a measure of the deviation of the flow from Newtonian behaviour. For $n \to 0$, the Cross Power Law model approaches the Newtonian viscosity ν_0, where for $n \to 1$ the Bird Carreau model behaves Newtonian. These equations have been directly extracted from the OpenFOAM source code and are illustrated in figure 5.1.

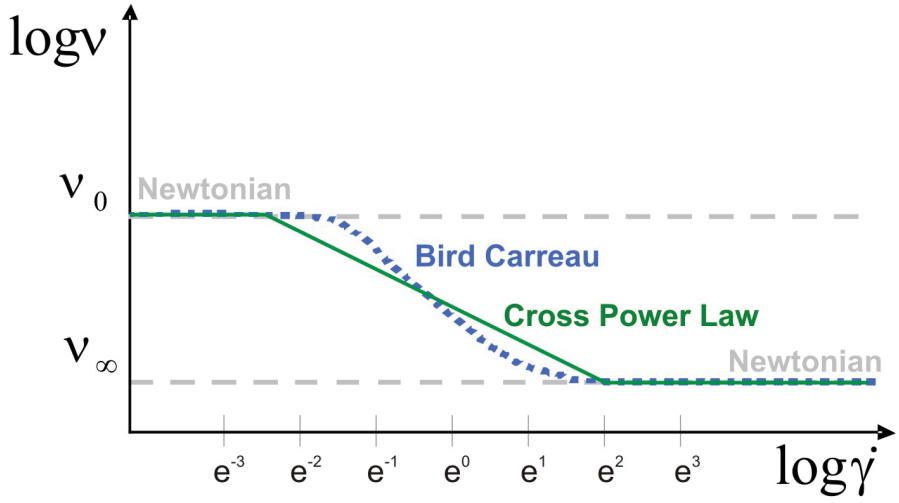

Figure 5.1: Variation of the viscosity ν with the strain rate $\dot{\gamma}$ according to the non-Newtonian Cross Power Law model (green) and the Bird Carreau model (blue).

5.2.4 Laminar flow

The flow through the Lyocell plant is mainly a laminar flow. In fluid dynamics, laminar flow occurs when a fluid flows in parallel layers, with no disruption between the layers. It is the opposite of turbulent flow. In nonscientific terms laminar flow is "smooth", while turbulent flow is "rough".

The dimensionless Reynolds number Re is an important parameter to describe whether flow conditions lead to laminar or turbulent flow. Reynolds numbers of less than 2300 are generally considered to be of a laminar type.

$$\mathrm{Re} = \frac{U_m \cdot L}{\nu} \tag{5.22}$$

Where U_m is the average flow velocity and L a characteristic length of the flow.

5.3 Discretisation

The mathematical Navier-Stokes equations as described in the previous section must be solved in order to find the solution of the flow situation at hand. It should be clear that these complex equations are not easy to solve analytically, if possible at all. It is however possible to solve these equations using a computer algorithm in a CFD software tool. In order to solve analytical equations using a computer algorithm, these equations should be discretised. The discretisation as applied in OpenFOAM is described briefly in this paragraph and is based mainly on the documentation in the OpenFOAM Programmer's Guide [44].

The term discretisation means approximation of a problem into discrete quantities. The Finite Volume (FV) method and others, such as the Finite Element (FE) and Finite Difference (FD) methods, all discretise the problem as follows:

- **Spatial discretisation** Defining the solution domain by a set of points that fill and bound a region of space when connected,
- **Temporal discretisation** (For transient problems) dividing the time domain into a finite number of time intervals, or steps,
- **Equation discretisation** Generating a system of algebraic equations in terms of discrete quantities defined at specific locations in the domain, from the PDEs that characterize the problem.

5.3.1 Spatial and temporal discretisation

Discretisation of the solution domain is shown in figure 5.2. The space domain is discretised into computational mesh on which the PDE's are subsequently discretised. Discretisation of time, if required, is simple: it is broken into a set of time steps Δt that may change during a numerical simulation, perhaps depending on some condition calculated during the simulation.

On a more detailed level, discretisation of space requires the subdivision of the domain into a number of cells, or control volumes. The cells are contiguous,

i.e. they do not overlap one another and completely fill the domain. A typical cell is shown in figure 5.2.

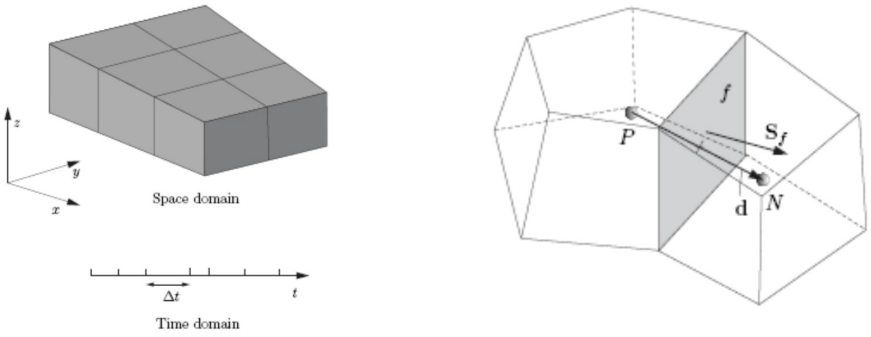

Figure 5.2: Example of the spatial discretisation of the solution domain (left), and the parameters in finite volume discretisation (right) [44].

Dependent variables and other properties are principally stored at the cell centroid P although they may be stored on faces or vertices. The cell is bounded by a set of flat faces, given the generic label f. In OpenFOAM there is no limitation on the number of faces bounding each cell, nor any restriction on the alignment of each face. This kind of mesh is often referred to as *arbitrarily unstructured* to differentiate it from meshes in which the cell faces have a prescribed alignment, typically with the coordinate axes. Whilst most properties are defined at the cell centroids, some are defined at cell faces. There are two types of cell faces.

- **Internal faces** Those faces that connect two cells (and it can never be more than two). For each internal face, OpenFOAM designates one adjoining cell to be the face owner and the other to be the neighbour
- **Boundary faces** Those belonging to one cell since they coincide with the boundary of the domain. These faces simply have an owner cell.

All solution domains (models) in this thesis are meshed or discretised using GAMBIT and all simulations are transient.

5.3.2 Equation discretisation

Consider the integral form of the generic equation describing conservation of a scalar quantity ϕ, without body forces or source terms:

$$\underbrace{\frac{\partial}{\partial t}\int \Omega\rho\phi \mathrm{d}\Omega}_{temporal} + \underbrace{\int S\rho\phi\boldsymbol{U}\cdot\boldsymbol{n}\mathrm{d}S}_{convective} = \underbrace{\int S\Gamma \mathrm{grad}\phi\cdot\boldsymbol{n}\mathrm{d}S}_{diffusive} \tag{5.23}$$

Each term in this equation is discretized its own way.

5.3.2.1 Discretisation of temporal term

The term is discretised by simple differencing in time using:

- **new values** $\phi^n = \phi(t + \Delta t)$ at the time step we are solving for
- **old values** $\phi^o = \phi(t)$ that were stored from the previous time step

In this thesis, the Euler implicit scheme, that is first order accurate in time, is used:

$$\frac{\partial}{\partial t}\int \Omega\rho\phi \mathrm{d}\Omega = \frac{(\rho_P\phi_P\Omega)^n - (\rho_P\phi_P\Omega)^o}{\Delta t} \tag{5.24}$$

Implicit means that the final point in estimating the integral is used. Contrary, an explicit method can be used where the integral is estimated using the value of the integrand at the initial point.

5.3.2.2 Discretisation of convective term

The convection term is linearised as follows:

$$\int S\rho\phi\boldsymbol{U}\cdot\boldsymbol{n}\mathrm{d}S = \sum_f \boldsymbol{S}_f\cdot(\rho\boldsymbol{U})_f\phi_f = \sum_f F\phi_f \tag{5.25}$$

The face field ϕ_f can be evaluated in OpenFOAM using a variety of schemes such as the Central Differencing (CD), the Upwind Differencing (UD) and the Blended

Differencing (BD) scheme. Throughout this work, only the CD scheme has been applied. It is second order, but unbounded:

$$\phi_f = f_x \phi_P + (1 - f_x)\phi_N \tag{5.26}$$

where $f_x = \overline{fN}/\overline{PN}$ where $\overline{fN}$ is the distance between f and the cell center N and $\overline{PN}$ is thze distance between the cell centers P and N.

5.3.2.3 Discretisation of diffusive term

The Laplacian term is linearised as follows:

$$\int S\Gamma \text{grad}\phi \cdot \boldsymbol{n} \text{d}S = \sum_f \Gamma_f \boldsymbol{S}_f \cdot (\nabla\phi)_f \tag{5.27}$$

The face gradient discretisation is implicit when the length vector $\mathbf{d}$ between the centre of the cell of interest P and the centre of a neighbouring cell N is orthogonal to the face plane, i.e. parallel to $\boldsymbol{s}_f$:

$$\boldsymbol{S}_f \cdot (\nabla\phi)_f = |S_f| \frac{\phi_N - \phi_P}{|\mathbf{d}|} \tag{5.28}$$

In the case of non-orthogonal meshes, an additional explicit term is introduced which is evaluated by interpolating cell centre gradients, themselves calculated by central differencing cell centre values.

5.3.3 PISO

As the pressure appears as an explicit source term in the momentum equations, a governing equation describing the evolution of this principle variable is needed to obtain the velocity field. By considering that the continuity constraint can be satisfied only by the correct pressure field, a modified continuity equation serves as an implicit governing equation for pressure.

The most commonly applied algorithms for pressure-velocity coupling using the continuity constraint include the Semi-Implicit Method for Pressure Linked Equations (SIMPLE) and its variants, such as SIMPLEC or PISO. The basic idea

behind these methods is to compute an initial velocity field using the momentum equations with old pressure values and to correct pressure and velocity fields applying an iterative procedure on the modified continuity equation until mass conservation is enforced [28, 55]. For all simulations described in this thesis, the PISO method is applied.

5.4 Multiphase Flows

When simulating the cellulose-particle interactions, dispersed two-phase flows are of main interest. One phase exists in discrete regions of space, completely surrounded by the other continuous phase. This is the case for both the solid particle-dope mixture as well as for the gel particle-dope mixture.

The simulation of solid and gel particles require a multiphase flow modeling approach. Basically, two different approaches for the tracking of interfaces are used, i.e. the Euler-Lagrange (or Lagrangian) and the Euler-Euler (or Euler) method [31, 38]. In both methods, the cellulose is considered as the fluid phase whereas the solid or the gel particles are called the dispersed phase. In CFD techniques, two approaches are applied to track the interfaces of either the gel or the solid particles:

- **Lagrangian** This methodology is often used when dispersed flow problems are in consideration. In this approach the fluid phase is considered as a continuum by solving the Navier-Stokes equations, while the dispersed phase is examined by tracking a large number of bubbles, particles, or droplets through the flow field. Exchange of mass, momentum and energy between the dispersed and the continuous phase is possible. In the Lagrangian approach, individual dispersed phase *elements* (i.e. particles, droplets or bubbles) are tracked through the flow domain. The conservation equations of momentum and energy for each element are expressed in a coordinate frame of reference which follows its trajectory. The conservation equation of momentum for a particle is called the particle equation of motion. This equation simply relates the rate of change of the particle's velocity to the

sum of forces acting upon it. The advantage of this approach is the direct physical interpretation of the inter-phase forces on the motion of the dispersed phase. Another advantage is that there is only one equation of motion for each particle, which makes it relatively easy to account for a distribution of particle sizes.

- **Euler** In the Euler approach, both the continuous and dispersed phases are described using Eulerian conservation equations written in fixed coordinates. Each phase is treated as a continuous medium, each inter-penetrating the other, and is represented by macroscopic conservation equations, one set for each phase, which are valid throughout the entire flow domain. In this methodology the different phases are treated as interpenetrating continua. The volume fraction describes the fraction of each phase within a computational cell and the sum of all volume fractions equals one. Corresponding conservation equations are solved for each phase. Because of the wide variety of practices, a commonly accepted set of fundamental two fluid equations (i.e. before any modelling is introduced) does not exist. It is therefore necessary to have a good physical understanding of the problem in order to describe it correctly. Herein lays the biggest disadvantage of the Eulerian approach. The advantage of the Eulerian two-fluid approach is that it is the most appropriate for general engineering flow studies. The two-fluid approach can encompass a wide variety of two-phase flow regimes, is more computationally efficient than the Lagrange alternative and is more capable of handling numerical problems arising during the solution of the coupled two-phase flow equations.

From the above, it should be clear that the small number of coarse solid particles is best simulated using the Lagrangian approach [1], whereas the gels are best simulated using the Eulerian approach. The *icoLagrangianFoam* solver has been developed especially for ideal and real Lagrangian particles in Newtonian fluids [4, 5] and will be discussed in paragraph 5.4.2. The generally used solver for the gel-dope situation is the Volume of Fluid (VoF) solver. In OpenFOAM, this solver is called *interFoam* and is discussed in the following paragraph.

Note that in the further discussions, the continuous cellulose phase is considered to be an incompressible, Newtonian fluid.

5.4.1 interFoam

The interFoam solver is designed for two or more incompressible, isothermal immiscible fluids using a VOF (Volume of Fluid) phase-fraction based interface capturing approach. The momentum and other fluid properties are of the mixture and a single set of momentum equations is solved. In this model the volume fraction of each of the fluids in each mesh cell is tracked. Stratified flows, free-surface flows, and the motion of large bubbles in a liquid are some application areas for this model [35].

The tracking of the interface between the phases is accomplished by the solution of a continuity equation for the volume fraction of one (or more) of the phases. For the i^{th} phase, this equation has the following form:

$$\frac{1}{\rho_i}\left[\frac{\partial}{\partial t}(\alpha_i\rho_i) + \nabla\cdot(\alpha_i\rho_i\boldsymbol{U}_i) = S_{\alpha_i} + \sum_{j=1}^{n}(\dot{m}_{ji} - \dot{m}_{ij})\right] \tag{5.29}$$

where $\dot{m}_{ij}$ is the mass transfer from phase i to phase j and $\dot{m}_{ji}$ is the mass transfer from phase j to phase i and α_i is the i^{th} fluid's volume fraction in a cell $(0 < \alpha_i < 1)$.

The volume fraction equation will not be solved for the primary phase; the primary-phase volume fraction will be computed based on the following constraint:

$$\sum_{i=1}^{n}\alpha_i = 1 \tag{5.30}$$

The properties appearing in the transport equations are determined by the presence of the component phases in each control volume. In a two-phase system, like the gel-dope mixture, if the phases are represented by the subscripts 1 and 2, and if the volume fraction of the second of these is being tracked, the density in each cell is given by

$$\rho = \alpha_2 \rho_2 + (1 - \alpha_2)\rho_1 \tag{5.31}$$

In OpenFOAM, α_i is translated as *gamma*, and the equation is translated as

```
MULES::explicitSolve(gamma, phi, phiGamma, 1, 0) ;
rhoPhi = phiGamma*(rho1 - rho2) + phi*rho2 ;
```

In the first line, the multidimensional Universal Limiter for Explicit Solution (MULES) is called upon. It is a significant improvement, particularly for interface capturing. The basic principle being that it is possible to create an iterative update sequence to correct a limiter such that phase fraction boundedness for two phase Volume of Fluid (VoF) problems is guaranteed even for unstructured meshes and multi-dimensional flow.

5.4.2 icoLagrangianFoam

In the Euler model the particle equation of motion describes the behaviour of the dispersed particles in the continuous cellulose phase. In the following paragraphs, this equation of motion is analysed for three different interactions, i.e.

- Particle - fluid
- Particle - particle
- Particle - wall

Using conditional averaging methods [31], the conservation of mass and conservation of linear momentum equations can be grouped in order to become the total momentum transfer from or to phase i. The basic conditional averaged two-phase flow equations in the absence of mass transfer and for incompressible phases, read [69]

$$\frac{\partial \alpha_i \rho_i}{\partial t} + \nabla \cdot \alpha_i \rho_i u_i = 0 \tag{5.32}$$

$$\begin{aligned} \frac{\partial}{\partial t}\alpha_i \rho_i u_i + \nabla \cdot \alpha_i \rho_i u_i u_i &= -\alpha_i \nabla p_i + \nabla \cdot \alpha_i \tau_i + \nabla \cdot \alpha_i \sigma_i^t + \alpha_i \rho_i g \\ &\quad + \left(\widetilde{p_{ij}} - \overline{p_i} \right) \nabla \alpha_i + \widetilde{p_{ij} n_i} \sum - \widetilde{\tau_{ij} \cdot n_i} \sum \end{aligned} \tag{5.33}$$

Grouping the interfacial terms on the right hand side of conditional averaged momentum equation, we have

$$M_i = \left(\widetilde{p_{ij}} - \overline{p_k}\right) \nabla \alpha_i + \widetilde{p_{ij} n_i} \sum - \widetilde{\tau_{ij} \cdot n_i} \sum \tag{5.34}$$

Where M_i is the total momentum transfer from or to phase i. Neglecting the surface tension terms, which are expected to be small in comparison with other forces, the momentum jump conditions over the interface imply that $M_c = -M_d$, where the subscripts d and c denote the dispersed (solid particles, gels) and continuous (dope) phase respectively.

This is a restatement of Newton's third law and provides a convenient basis for the formulation of the interfacial momentum transfer models since we need only consider the forces acting on one of the phases. It is convenient to consider the forces acting on the dispersed phase since the total force on the dispersed phase may be naturally decomposed into its components, since Newton's second law implies

$$M_d = \sum F \tag{5.35}$$

The forces acting on the dispersed phase usually comprise the drag force F_d, the virtual mass force F_{vm}, the lift force F_l and the Basset force F_b. Hence, symbolically we have

$$M_d = F_d + F_{vm} + F_l + F_b \tag{5.36}$$

In short, these forces account for

- The relative motion between a submerged body and the surrounding fluid gives rise to the so-called **drag force**
- The **virtual mass force** or added mass force is the additional force required to accelerate a particle due to the mass of the fluid in its vicinity, which also needs to be accelerated.
- The **lift force** describes the lateral force experienced by a particle subjected to a shearing flow or due to the rotation of the particle itself. For solid-liquid flows the lift force is negligible compared with other forces [1].

- The **Basset force** represents the influence of the time dependent development of the boundary layer on the particle surface in accelerating flows.

Note that the approach via conditional averaging is a very general method of describing multiphase flows. Its generality makes this method more and more attractive. For the large particles, however, a more basic approach can be used that makes more direct use of the Lagrange properties of the particles.

The particles are looked at as single Lagrange objects, whose behaviour (acceleration, velocity and position) is completely dependent on the local conditions of the continuous flow. The particle tracks are determined through the simple Lagrangian equations of motion:

$$\frac{\mathrm{d}}{\mathrm{d}t}(\boldsymbol{x}_p) = \boldsymbol{u}_p \tag{5.37}$$

$$\frac{\mathrm{d}}{\mathrm{d}t}(\boldsymbol{u}_p) = \boldsymbol{a}_p \tag{5.38}$$

The actual coupling between the behaviour of the particles and the fluid flow field comes through the particle acceleration term a_p, which contains the force action of the local velocity field (fluid - particle interaction), the pressure field, the buoyancy and the particle-particle collisions.

$$\boldsymbol{a}_p = D_p(\boldsymbol{u}_f - \boldsymbol{u}_p) - \frac{1}{\rho_p}\nabla p_p + \left(1 - \frac{\rho_f}{\rho_p}\right) g + \boldsymbol{a}_{coll} + \boldsymbol{a}_{wall} = 0 \tag{5.39}$$

The essential coupling of particle behaviour to the particle surroundings is performed by the acceleration term $\boldsymbol{a}_p$. As can be seen in equation 5.39, it contains acceleration effects of the local fluid velocity field, buoyancy force, particle collision effects $\boldsymbol{a}_{coll}$ and particle-wall interaction $\boldsymbol{a}_{wall}$. Both ideal and real particles can be simulated using the model developed by G. Boiger. The exact implementation of the ideal and real particle model can be found in his PhD thesis and several articles on the subject [4, 5].

At this point, all simulation tools are described and can be used to study the Lyocell process in more detail. This is done in the next two chapters.

Chapter 6

CFD Case Studies

Basic CFD simulations have been carried out in order to test all the solvers and tools as described in chapter 5. With these tests, limitations of the solvers became apparent and could be treated appropriately in order to stabilise all solvers and make them operational for larger and more complex geometries. Simulations were conducted on simplified imaginary models as well as on real filter and jet configurations up to the extreme complex geometry of the KREY filter [18].

The material properties are the same for all simulations, unless stated otherwise. The main fluid is the cellulose solution with a density of 1.200 kg/m^3 and a constant kinematic viscosity ν of 1e^{-4} Pa.s. The gels have a density of 1.500 kg/m^3 and a constant kinematic viscosity ν of 1e^{-4} Pa.s. The solid particles have a density of 1.500 kg/m^3. All fluids are considered to be incompressible Newtonian fluids that flow in a laminar regime. Although the dope is basically a non-Newtonian fluid, the simulations have ignored this in order to focus completely on the blocking by gel and solid particles.

6.1 Basic simulations

During the project, several different solvers have been tested on their robustness and correctness when it comes to simulating the interaction between the gels (interFoam), the Large Particles (icoLagrangianFoam) and the dope in complex real geometries. Before simulations on complex geometries were conducted, all solvers

and situations were tested using basic simulations. These feasibility studies are described in the following two sections.

6.1.1 2D Models

The icoLagrangianFoam solver exists only in 3D. Therefore, no 2D models have been created for this solver. The interFoam solver can be applied to 2D models. Since 2D simulations are much faster than 3D, an intensive parameter study of the interFoam solver has been conducted on 2D models. These models are described in figure 6.1.

The main model is the *1-bubble-1-obstacle-2D* model which is used to see if a gel particle with diameter 50μm can get stuck in a narrow passage of 25μm in width. The characteristic flow velocity through the model is about 0.1m/s and the residence time is 0.01s.

Two more models have been constructed as can be seen in figure 6.1, i.e. *3-bubbles-3-obstacles* and *1-large-bubble-3-obstacles*. The purpose of these extra models was to investigate several possible extreme situations of gels approaching an obstacle such as a filter or a jet. The Reynolds number (see section 5.2.4) for all 2D models is approximately Re $\approx \frac{1.10^{-1}.150.10^{-6}}{10^{-4}} = 0.15$, i.e. the flow through the models is a laminar flow.

One major issue is that the interFoam solver should be able to simulate the blocking by the gels. This would mean that the gel particles can deform, but also can have a different flow velocity than the surrounding field. The main factor that determines whether a gel particle can get stuck is the surface tension σ. Simulations have been run where the surface tension is varied from 0.0007N/m up to 7000N/m. Note that the surface tension between water and air is about 0.07N/m. All simulations ran stable. The results looked the most plausible for $\sigma = 0.007N/m$ and $\sigma = 7N/m$. These results are plotted in figure 6.2 and figure 6.3.

Model			1_bubble_1_obstacle_2D	
		Value	*Unit*	*Sketch*
Dim.	H x W	1000 x 150	µm	
	Obstacle square edge	100	µm	
	Gel circle diameter	50	µm	
BC	Inlet Velocity Inlet	0.1	m/s	
	Outlet Pressure Outlet	0	Pa	
	Wall No slip wall			
Mesh	Number of cells	~6.000		
Solver	interFoam			
Goal	Parameter study of interFoam solver in 2D			

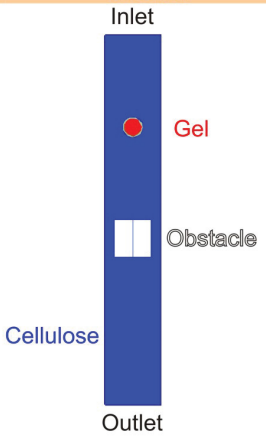

Model			3_bubbles_3_obstacles	
		Value	*Unit*	*Sketch*
Dim.	H x W	1000 x 450	µm	
	Obstacle square edge	100	µm	
	Gel circle diameter	50	µm	
BC	Inlet Velocity Inlet	0.1	m/s	
	Outlet Pressure Outlet	0	Pa	
	Wall No slip wall			
Mesh	Number of cells	~18.000		
Solver	interFoam			
Goal	Parameter study of interFoam solver in 2D			

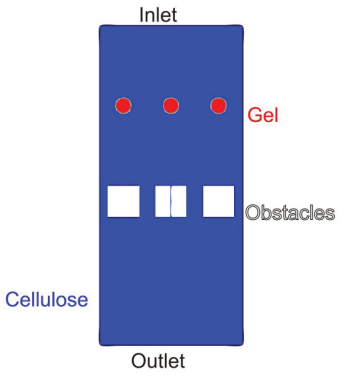

Model			1_large_bubble_3_obstacles	
		Value	*Unit*	*Sketch*
Dim.	H x W	1000 x 450	µm	
	Obstacle square edge	100	µm	
	Gel circle diameter	200	µm	
BC	Inlet Velocity Inlet	0.1	m/s	
	Outlet Pressure Outlet	0	Pa	
	Wall No slip wall			
Mesh	Number of cells	~18.000		
Solver	interFoam			
Goal	Parameter study of interFoam solver in 2D			

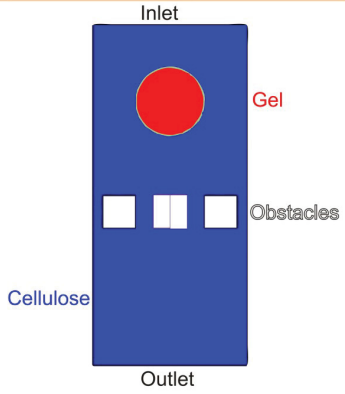

Figure 6.1: 2D models used for basic simulations of interFoam solver

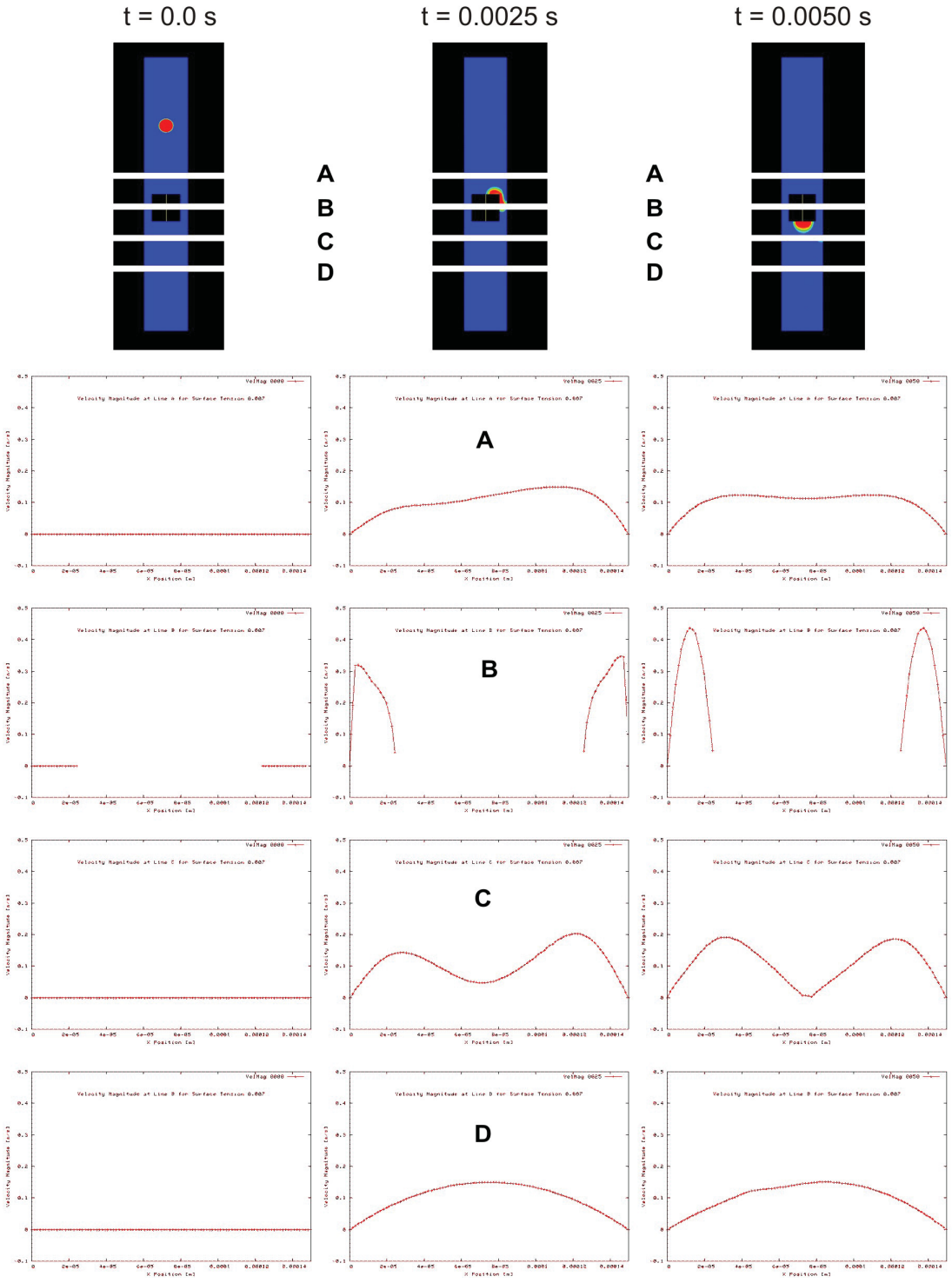

Figure 6.2: Flow of a gel particle through a narrow passage, $\sigma = 0.007 N/m$, contour plot of gel fraction (red) in cellulose fluid (blue) at the top, below velocity magnitude at lines A, B, C and D at three different times t=0s (left), t=0.0025s (middle) and t=0.0050s (right).

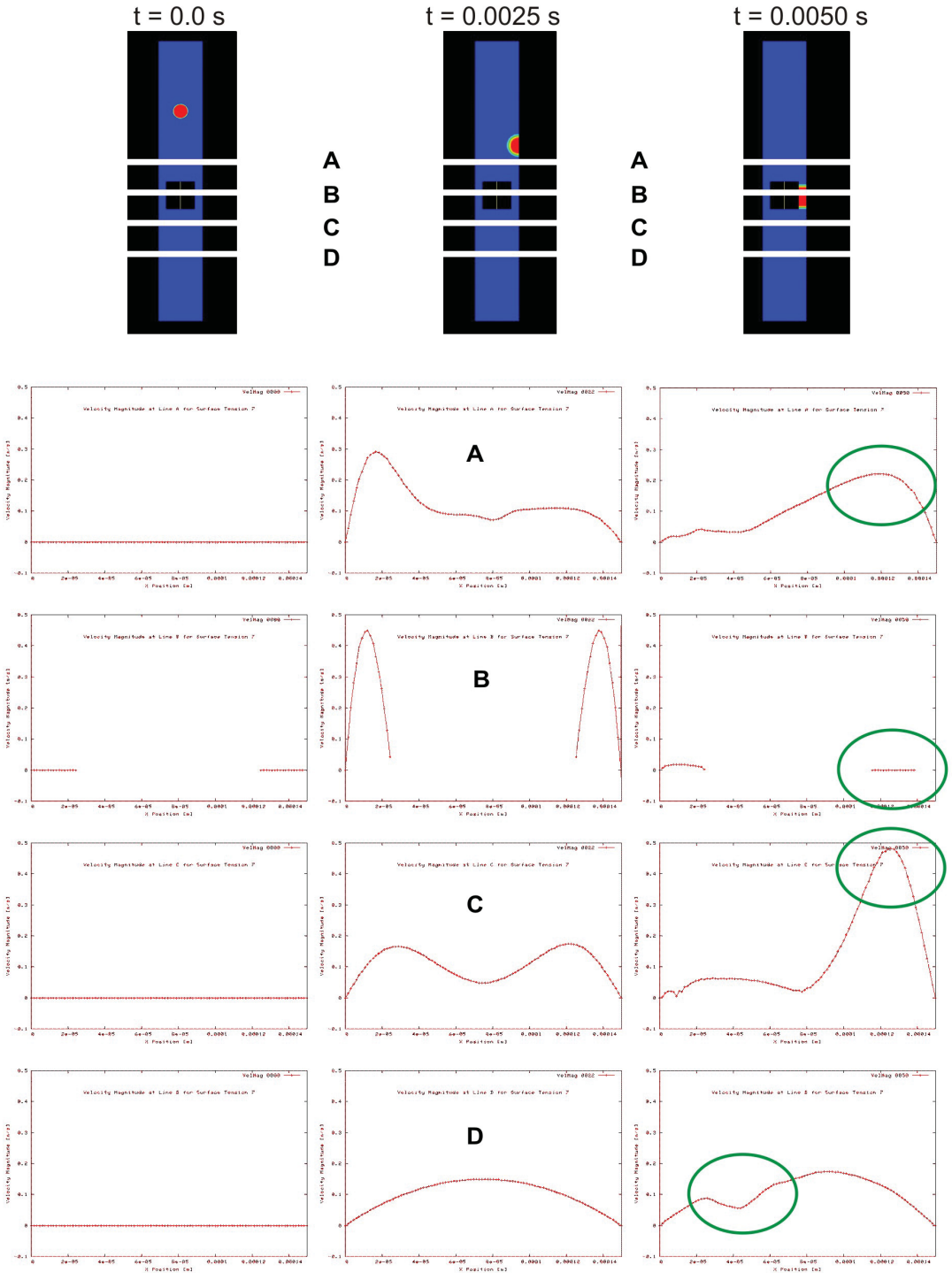

Figure 6.3: Flow of a gel particle through a narrow passage, $\sigma = 7N/m$, contour plot of gel fraction (red) in cellulose fluid (blue) at the top, below velocity magnitude at lines A, B, C and D at three different times t=0s (left), t=0.0025s (middle) and t=0.0050s (right).

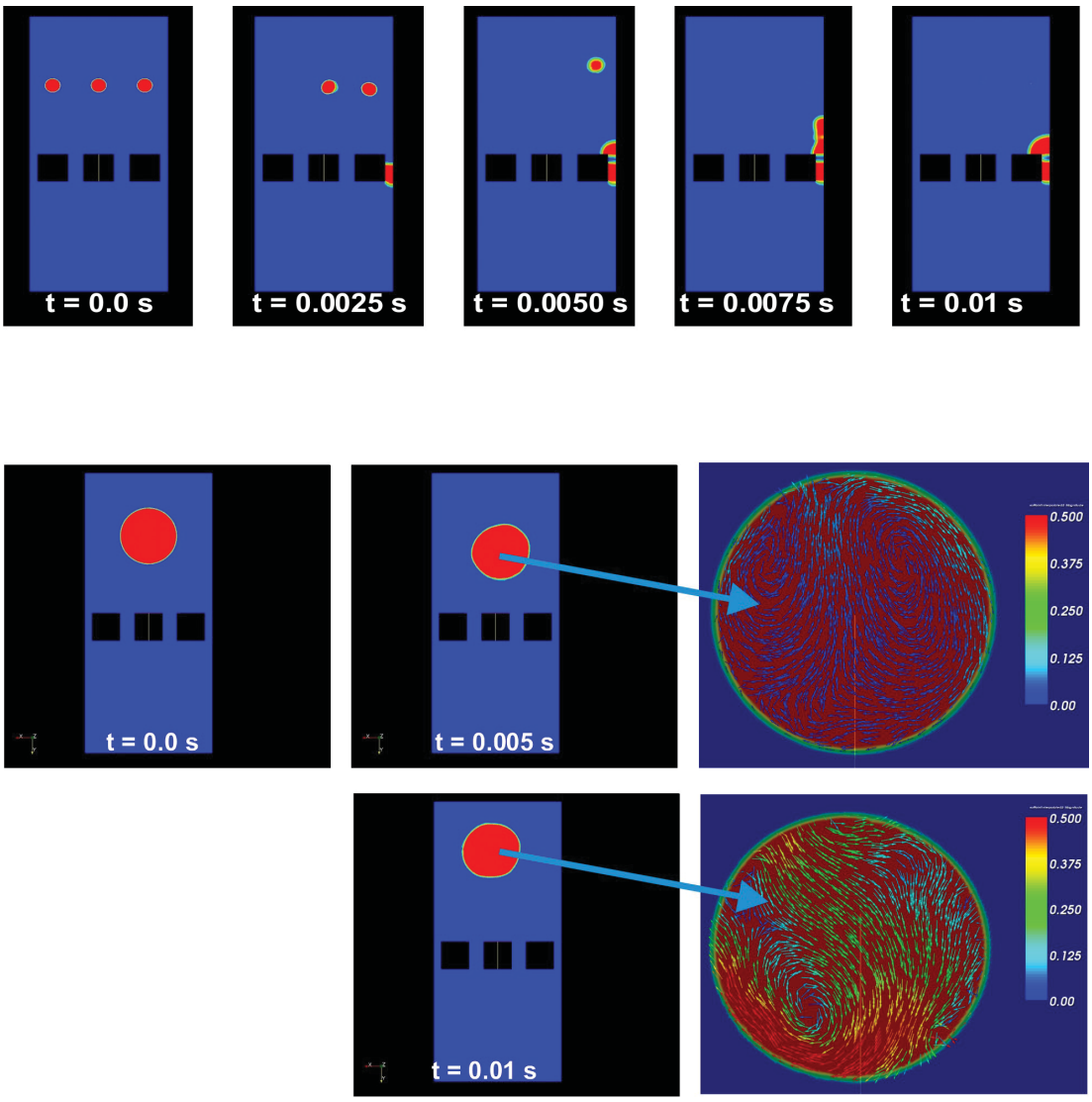

Figure 6.4: Simulation of 2D gel models, 3-bubbles-3-obstacles (top) and 1-large-bubble-3-obstacles with vector plots of the internal flow inside the large bubble (bottom)

According to these results, it is clear what the influence of the surface tension on the flow behaviour of gel particles and the flow field in general is. Gel particles with low surface tensions have a temporarily effect, but since they do not get stuck, the influence is minimal. Gel particles with high surface tensions on the other hand have a larger effect on the flow field. As soon as they block a passage, the influence becomes even more apparent and permanent. This effect can not be neglected.

Similar tests have been conducted on different geometries in order to see the effect of more complex situations. Some interesting qualitative results are plotted in figure 6.4. The *3-bubbles-3-obstacles* model shows unexpected flow patterns in that the gel particles flow sideways as well as repulsion and coagulation of the gel particles. Note that for this simulation an extreme high surface tension of 70N/m has been used.

Finally, the model *1-large-bubble-3-obstacles* shows the movements of a very large gel particle, again with a high surface tension (70N/m). This situation might occur if a lot of surfactants are caught on the interface of a large gel particle and the cellulose. The internal circulation inside the gel particle (see figure 6.4) causes the particle to *float* in the cellulose [34, 63].

6.1.2 3D Models

Both the interFoam as well as the icoLagrangianFoam solvers have been extensively tested on 3D models. These models are illustrated and described in figure 6.5. The dimensions of the models give rise to characteristic velocities of about 0.5m/s and a residence time of 0.01s. In the *1-bubble-1-obstacle* and the *Small-Holes* model, the narrow passage has a dimension of 25μm. For the *JetConfig-9* model, the real diameters of the jets have been taken, i.e. 150μm at the jet inlet. Again, the Reynolds number of these models is approximately 0.15, indicating that the flow is a true laminar flow.

These models were mainly created to verify the tests conducted in 2D as well as to do some preliminary tests on the icoLagrangianFoam solver.

Model					1_bubble_1_obstacle
			Value	*Unit*	*Sketch*
Dim.	H x W x D		1000 x 150 x 150	µm	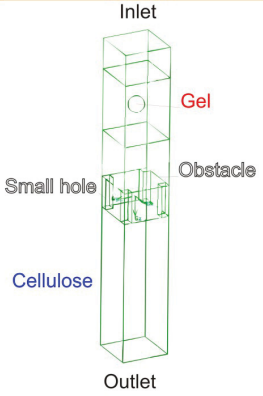
	Obstacle	square edge	100	µm	
	Gel	circle diameter	50	µm	
BC	Inlet	Velocity Inlet	0.1	m/s	
	Outlet	Pressure Outlet	0	Pa	
	Wall	No slip wall			
Mesh	Number of cells		~180.000		
Solver	interFoam				
Goal	Parameter study of interFoam solver in 3D				

Model					SmallHoles
			Value	*Unit*	*Sketch*
Dim.	H x W x D		1000 x 150 x 150	µm	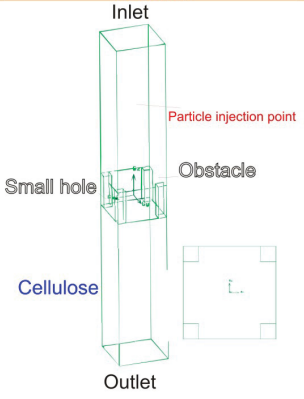
	Obstacle	square edge	100	µm	
	Particle	mean diameter	20 ± 10	µm	
BC	Inlet	Velocity Inlet	0.1	m/s	
	Outlet	Pressure Outlet	0	Pa	
	Wall	No slip wall			
Mesh	Number of cells		~180.000		
Solver	icoLagrangianFoam				
Goal	Parameter study of icoLagrangianFoam solver				

Model					JetConfig_9
			Value	*Unit*	*Sketch*
Dim.	H x W x D		1500 x 1050 x 1050	µm	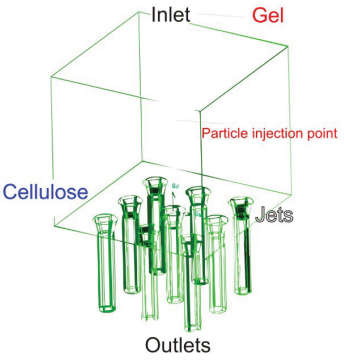
	Gel	Injection at inlet			
	Particle	mean diameter	25 ± 25	µm	
BC	Inlet	Velocity Inlet	0.1	m/s	
	Outlet	Pressure Outlet	0	Pa	
	Wall	No slip wall			
Mesh	Number of cells		~300.000		
Solver	icoLagrangianFoam, interFoam				
Goal	Study of gels and particles in jet system				

Figure 6.5: 3D models used for basic tests on interFoam and icoLagrangianFoam solvers

The simple simulations for the interFoam solver as described in paragraph 6.1.1 are repeated in 3D with a surface tension of 0.07 for the *1-bubble-1-obstacle* model and with a surface tension of 0.7 for the *JetConfig-9* model. The qualitative results are shown in figure 6.6. The influence of a low surface tension is clearly demonstrated. The model *JetConfig-9* shows that, although most of the large gel is pressed slowly through the jets, smaller gels remain in the dead zones (red circles). These gels can trap solid particles or dirt that can than block the filter or jet system.

Basic 3D tests on the ideal particle model [5] have been conducted in order to test all implemented interactions between particles and particles and particles and walls. For the tests on the ideal particle solver, the *SmallHoles* model is used. Figure 6.7 clearly shows that even if ideal particles get stuck, the flow can pass. There is never a complete stop of the fluid flow in the jets. The velocity through the jets only drops a few percent as soon as a particle blocks the jet.

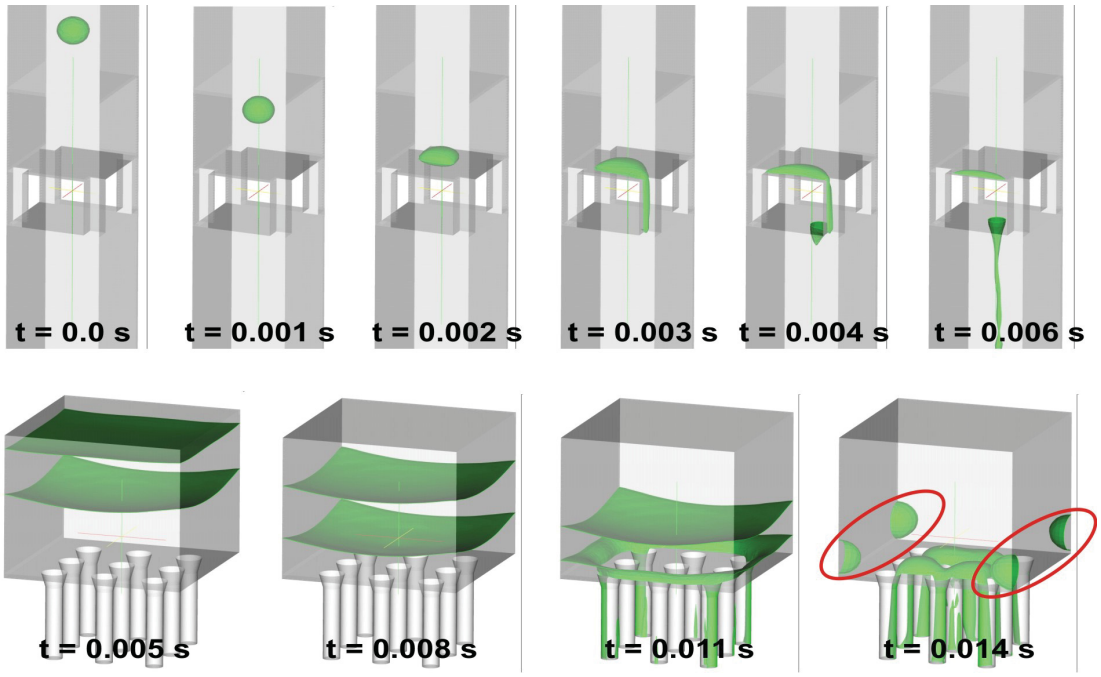

Figure 6.6: Simulation of 3D gel models, 1-bubble-1-obstacle (top) and JetConfig-9 (bottom)

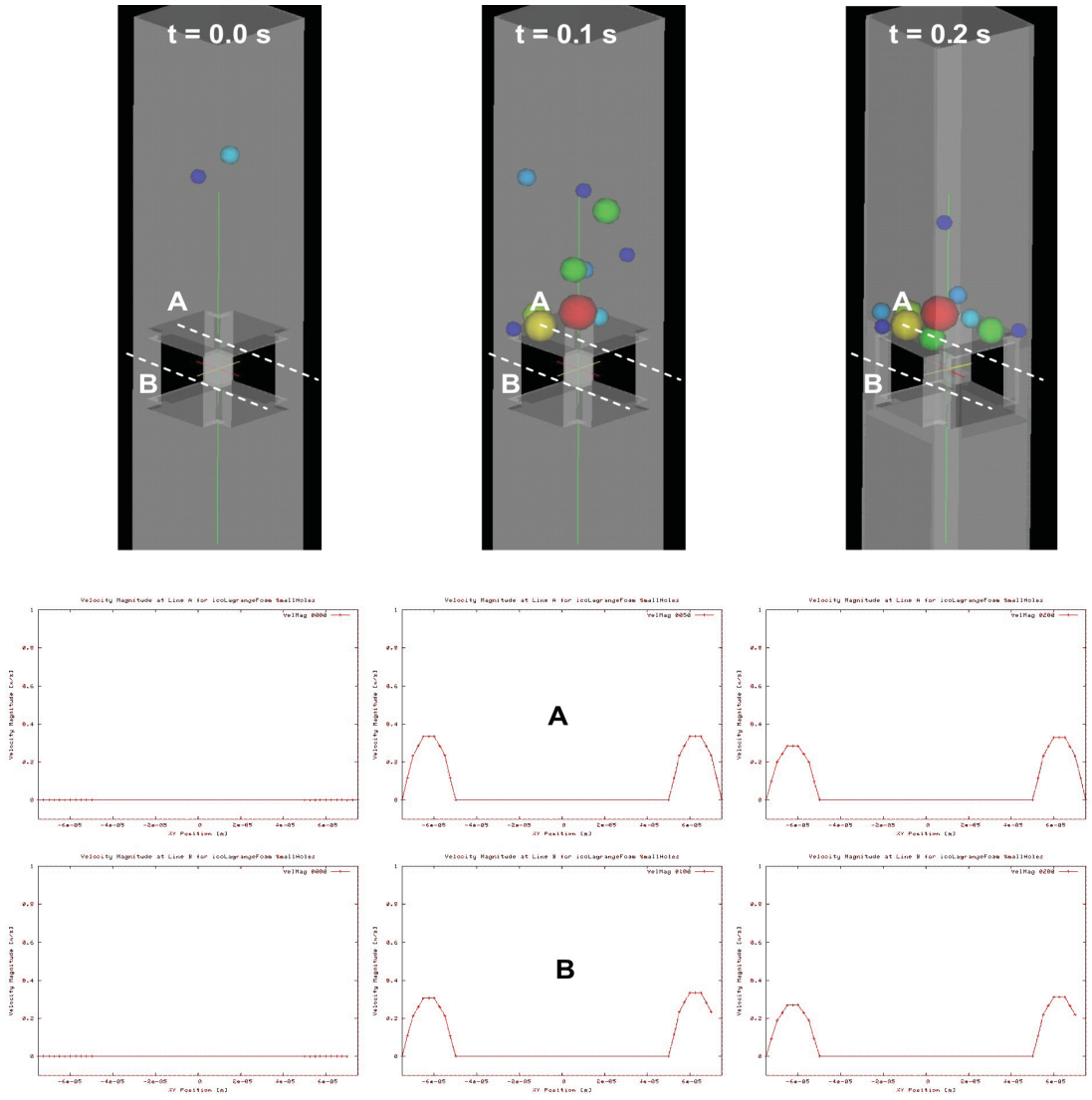

Figure 6.7: Flow of solid ideal particles through four narrow passages, plot of particle diameter at the top, below velocity magnitude at lines A and B at three different times $t = 0s$ (left), $t = 0.1s$ (middle) and $t = 0.2s$ (right).

6.2 Gel flow

The following two paragraphs describe complex simulations on real geometries as they occur in the Lyocell plant. Paragraph 6.2.1 studies the influence of large gels with different surface tensions on the DHS and DES filter configurations. Paragraph 6.2.2 describes the influence of non-Newtonian viscosity models by simulating the control window experiment (see section 3.2.2).

The CFD models used for these simulations and their dimensions are depicted in figure 6.8. The jet inlet has a diameter of 150μm which diminishes to 100μm (jet inlet cone). The woven structure of the filters has not been taken into account for these simulations in order to have a structured hexahedral mesh with a low number of cells which speeds up the simulations. Note the difference in filter configuration between the DES and the DHS model. In the real Lyocell plant, there are no jets after the DHS. Since the goal of the project is to study filter systems in general, there has been made abstract of this and both the DHS and the DES filter are placed right on top of the jet system. This way, the influence of double filters (DHS) can also be studied. Only the DES model is shown with the exact initial position of the injected gels (*DES-75-53-interFoam*). The situation is similar for the DHS model where initial gels are simulated.

The characteristic velocity through the models is 0.5m/s, which returns a flowthrough or residence time of 0.004s. The overall Reynolds number is about 0.75. The flow is laminar.

6.2.1 Influence of surface tension

The results of the simulations of gels on the DHS and DES models using the interFoam solver are plotted in figure 6.9 and figure 6.10. The models with low surface tension (0.07N/m) show that the small gels flow through the filter-jet system without any problems. The larger plate shaped gel at the inlet slowly moves towards the filter and flows through. Note that the large gel moves slower in the DES and DHS models than for the JetConfig-9 model. The filters obviously cause the gels to pass slower through the jets. This might cause problems if a lot of dirt particles are present.

Model			Value	Unit	DH_35_30 Sketch
Dim.	H x W x D		2030 x 945 x 1020	µm	
	Filter	wire thickness	30	µm	
		mesh size	35	µm	
	Particle	mean diameter	25 ± 25	µm	
BC	Inlet	Velocity Inlet	0.1	m/s	
	Outlet	Pressure Outlet	0	Pa	
	Wall	No slip wall			
Mesh	Number of cells		~140.000		
Solver	icoLagrangianFoam				
Goal	Study of particles and filter in jet system similar model for DH_63_40				

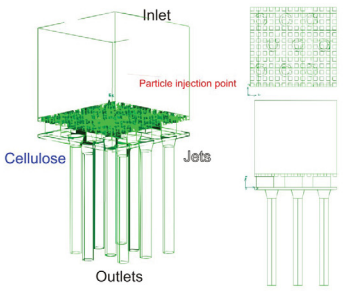

Model			Value	Unit	DES_75_53 Sketch
Dim.	H x W x D		2030 x 945 x 1020	µm	
	Filter	wire thickness	53	µm	
		mesh size	75	µm	
	Particle	mean diameter	25 ± 25	µm	
BC	Inlet	Velocity Inlet	0.1	m/s	
	Outlet	Pressure Outlet	0	Pa	
	Wall	No slip wall			
Mesh	Number of cells		~120.000		
Solver	interFoam, multiphaseInterFoam				
Goal	Study of particles and filter in jet system				

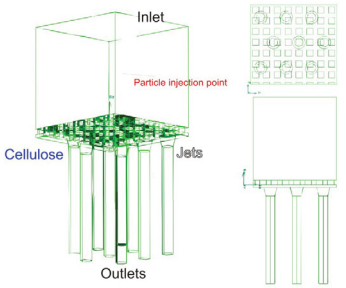

Model			Value	Unit	DES_75_53_interFoam Sketch
Dim.	H x W x D		2030 x 945 x 1020	µm	
	Filter	wire thickness	53	µm	
		mesh size	75	µm	
	Gel	circle diameter	50, 100 and 150	µm	
BC	Inlet	Velocity Inlet	0.1	m/s	
	Outlet	Pressure Outlet	0	Pa	
	Wall	No slip wall			
Mesh	Number of cells		~800.000		
Solver	interFoam, multiphaseInterFoam				
Goal	Study of gels and filter in jet system				

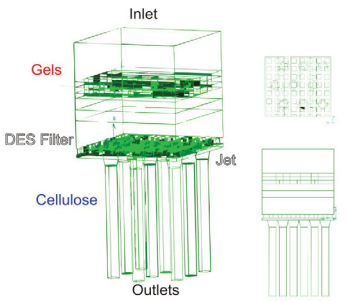

Figure 6.8: 3D models used for real simulations of the Lyocell process

All gels in the models with the high surface tension (7N/m) immediately coagulate to form larger particles. These particles move very slowly towards the filter. This is due to forces acting inside the gel bubble [34]. Even after a relatively long time (twice the residence time) the gels are still not through the filter-jet system. Compared with the resident time of the solid particles (about 0.005s, see paragraph 6.3), it should be clear that the gels can help the solid particles to cluster and to block the filter-jet system even more.

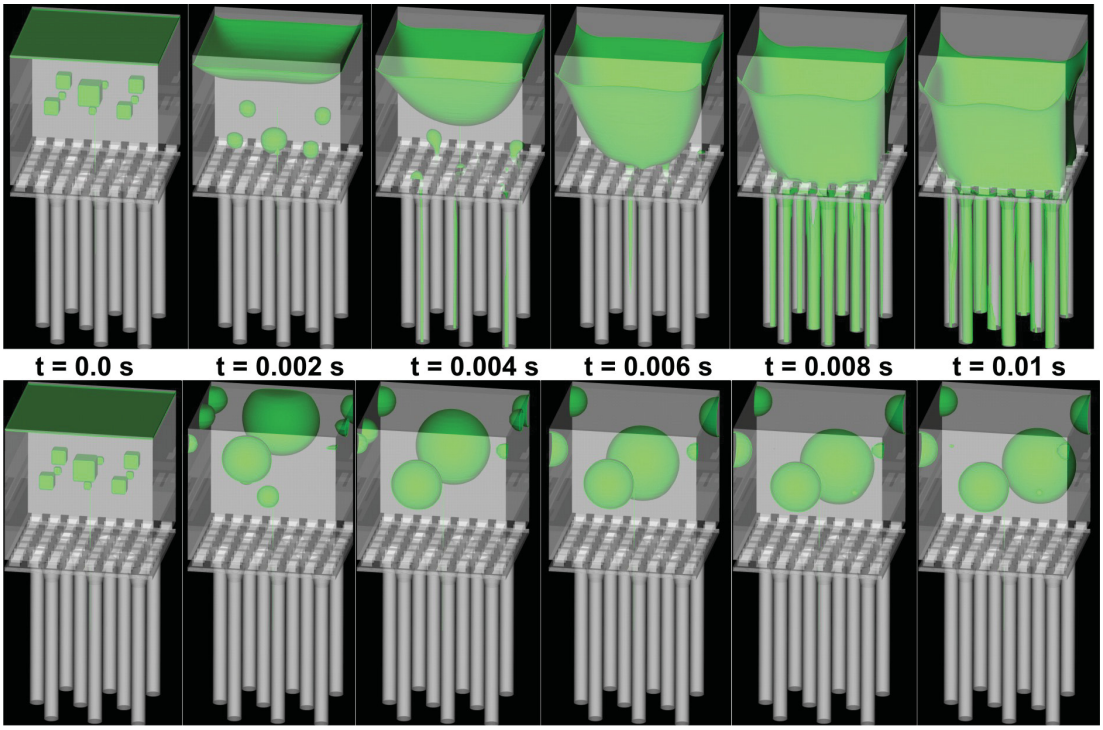

Figure 6.9: Simulation of gels passing the filter-jet system for $\sigma = 0.07$ (top) and $\sigma = 7$ (bottom) for the DES-75-53 model

Figure 6.10: Simulation of gels passing the filter-jet system for $\sigma = 0.07$ (top) and $\sigma = 7$ (bottom) for the DHS-35-30 model

6.2.2 Influence of viscosity model

So far, all the simulations are carried out using Newtonian materials. Since the cellulose is a highly non-Newtonian material, this approach induces errors. The complexity of the rheological behaviour of the cellulose has already been studied in the past [28]. It was impossible during this project to implement these created models for FLUENT in OpenFOAM. However, OpenFOAM contains a few more simple viscosity models (see section 5.2.3). These will not completely cover the complex non-Newtonian behaviour of the cellulose and the gels, but they might be a better approach of reality.

In order to test the viscosity models present in OpenFOAM, the control window cell experiment (see paragraph 3.2.2) is simulated. The simulation model is described in figure 6.11. The inlet velocity has been calculated from the velocity at which particles moved by the control volume cell. This velocity is set to 0.00184 m/s. Hence, the residence time is approximately 3.4s. The flow is laminar.

Model					**Cell_3D**
			Value	*Unit*	*Sketch*
Dim.	H x W x D		71 x 2096 x 6280	µm	
	Gel	rectangular	71 x 70, 35.5 x 70, and 17.75 x 70	µm	
BC	Inlet	Velocity Inlet	0.00184	m/s	
	Outlet	Pressure Outlet	0	Pa	
	Wall	No slip wall			
Mesh	Number of cells		~420.000		
Solver	interFoam				
Goal	Study of real geometry, Newtonian models				

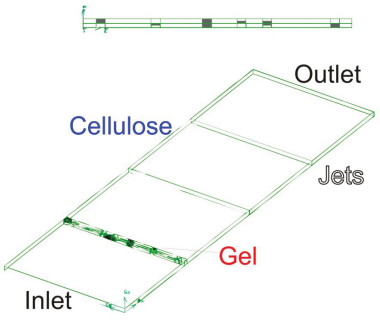

Figure 6.11: Sketch of the control window model used to simulate different viscosity models

In the model, six gel particles of different rectangular size are predefined. Their behaviour in the control window cell is simulated using a constant viscosity of 1Pa.s and 10.000Pa.s (Newtonian model) and two non-Newtonian viscosity models, Cross Power Law and Bird Carreau (see paragraph 5.2.3). The quantitative results of these simulations is seen in figure 6.12 to figure 6.14.

The Newtonian fluid simulations show little difference between a low ($1e^0$) and a high ($1e^4$) viscosity. The gel particles seem to be cut into slices due to the high velocity gradient. It is clear that the walls have a significant influence on these simulations [30].

From paragraph 5.2.3, it is clear that for the Bird Carreau simulations, the fluid is a Newtonian for $n = 1$ and for $n < 1$, the fluid behaves more and more non-Newtonian. The Bird Carreau simulations for $n = 0.1$ show a completely different behaviour compared to the Newtonian fluid simulations. The gel particles move slowly through the cell and do not get cut into slices as badly as the Newtonian gels do, mainly because the velocity gradients are not as high as for the Newtonian simulations and because the gels are strongly held together. It can also be seen that the gels have an influence on the flow field in the cell.

For the Cross Power Law mode, these results are exactly vice versa. For $n = 0$, the flow behaves like a Newtonian fluid. For $n = 1.1$, the situation is completely different. The gels do not get cut into slices at all, however, the influence of the gels on the flow field is less pronounced as it is for the Bird Carreau $n = 0.1$ simulations. Note that it is shown in figure 5.1 that the Bird Carreau and the Cross Power Law model only show a behaviour different from Newtonian models in a particular bandwidth of strain rate $\dot{\gamma}$. Outside this bandwidth, the material behaves completely Newtonian, albeit with a relatively low ($\nu_\infty = 1e^0$) or high ($\nu_0 = 1e^4$) viscosity.

It can be concluded that the choice of the viscoelastic constitutive equations can have an influence on the simulation of gels, especially in the vicinity of the walls. However, for relatively low kinematic viscosities as used in all previous simulations ($\nu == 1e^{-4}$), the assumption that the material behaves in a Newtonian way can be justified.

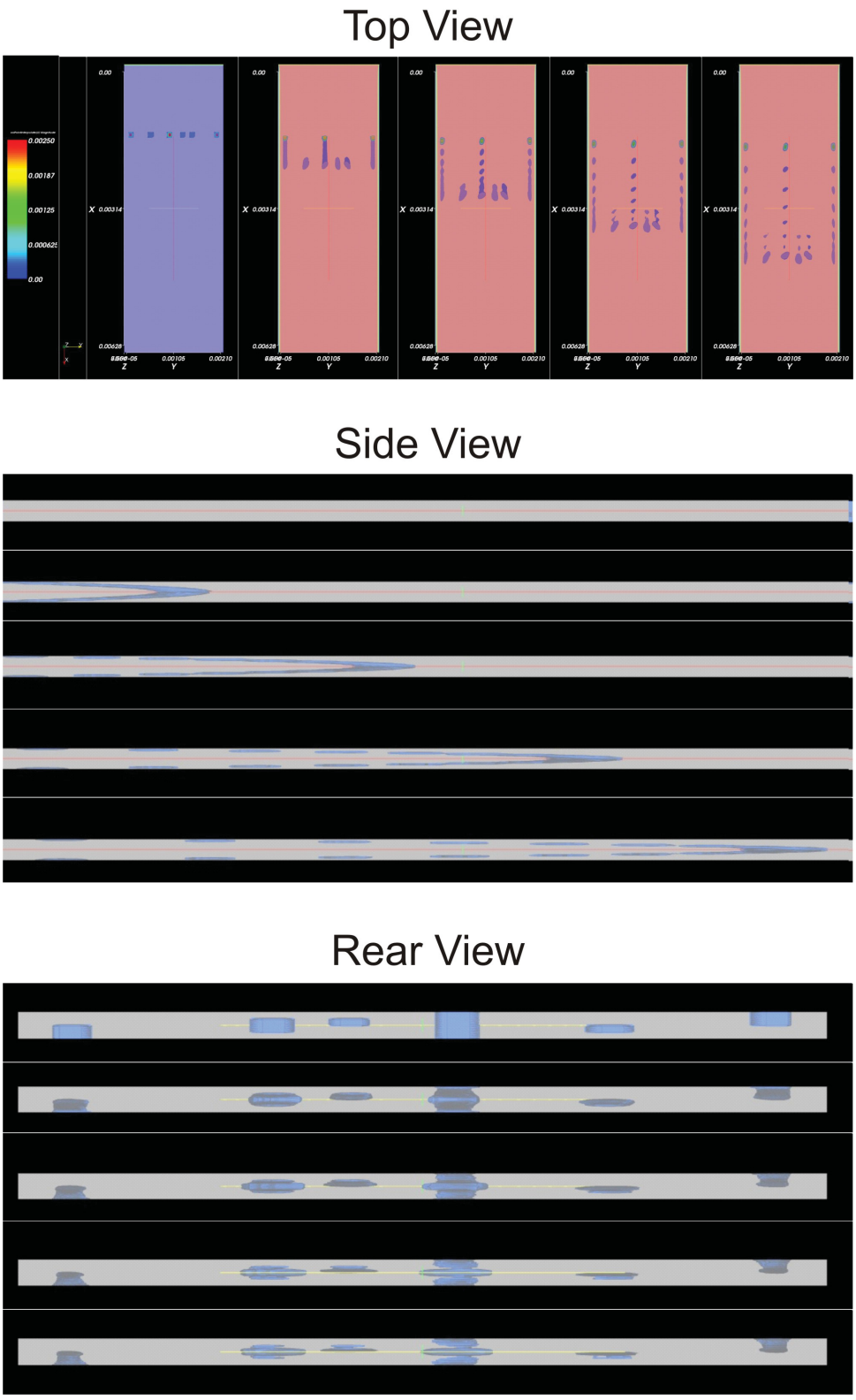

Figure 6.12: Control window cell simulation, top view (top), side view (middle) and rear view (bottom), Newtonian fluid, $\nu = 1e^0$. The quantitative results look the same for $\nu = 1e^4$.

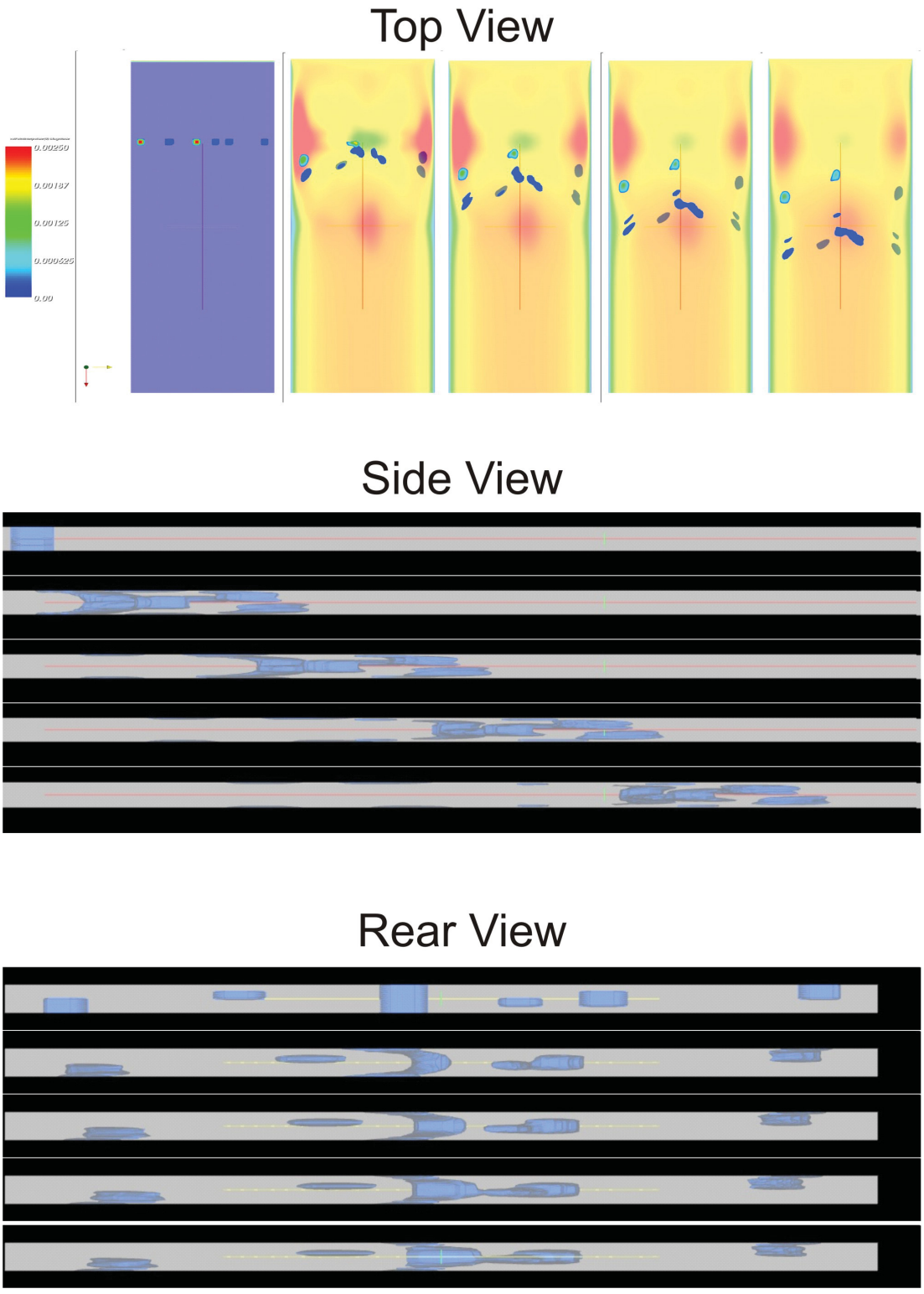

Figure 6.13: Control window cell, top view (top), side view (middle) and rear view (bottom), Bird Carreau fluid, $n = 0.1$

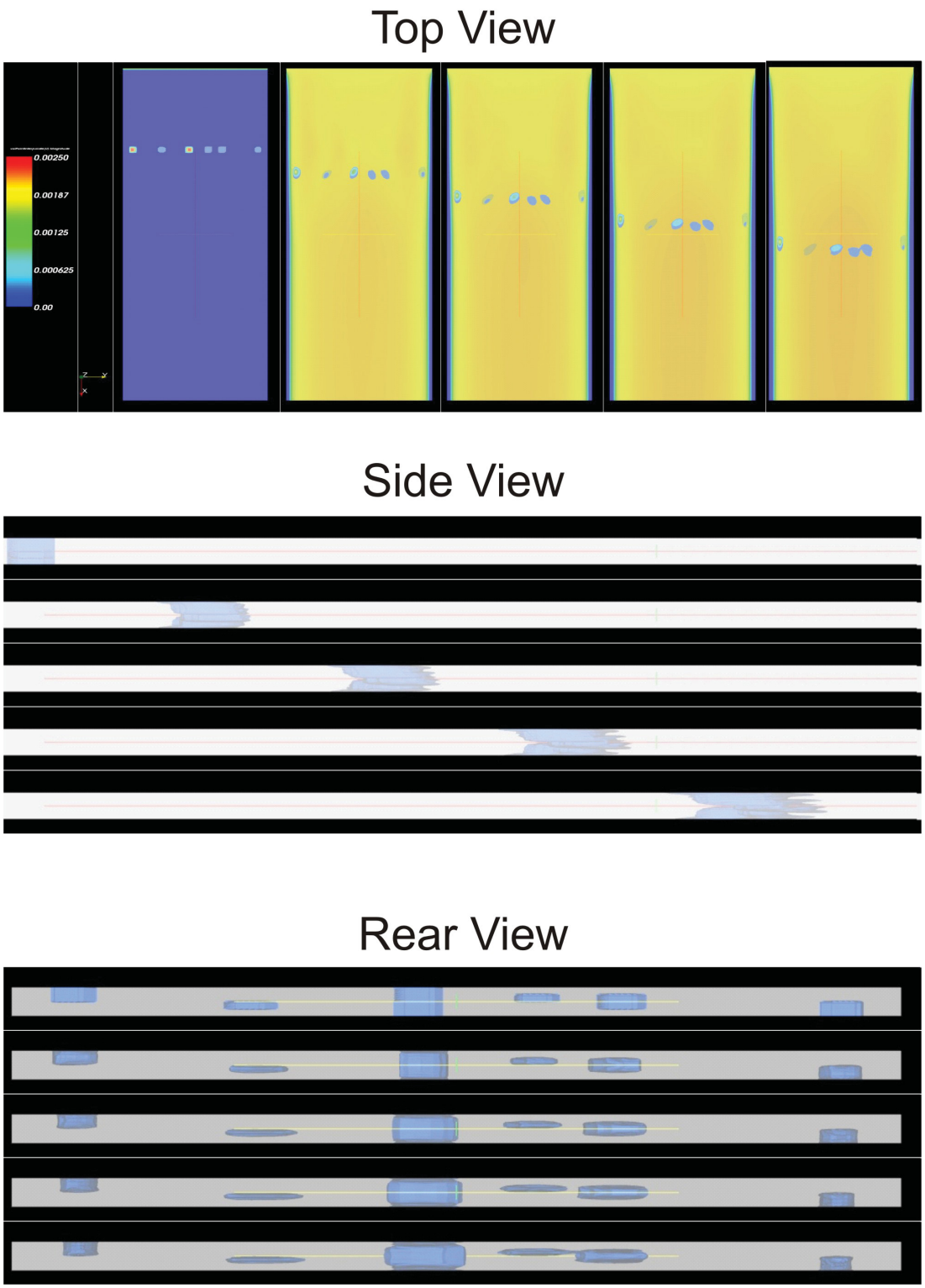

Figure 6.14: Control window cell simulation, top view (top), side view (middle) and rear view (bottom), Cross Power Law fluid, $n = 1.1$

6.3 Large particle flow

The following two paragraphs describe the simulation of the ideal and real particles in the CFD models of the real Lyocell process (see figure 6.8). The ideal particles are spherical particles with an average diameter of 25μm and a standard deviation of 25μm. The real particles are ellipsoids with three principal axes that have an average diameter of 25μm and a standard deviation of 25μm. For both the ideal and the real particles, the icoLagrangianFoam solver changes the diameters at random in the interval [0,50].

6.3.1 Ideal particles

The simulations of the DES filter, using the DES-75-53 CFD model (figure 6.15), show that all of the ideal particles with a diameter smaller than the mesh spacing pass the filter. However, some particles get stuck between the filter and the jet plate (red circles). This can happen if the filter mesh is larger than the distance from the filter to the jets. From the 15 initially injected particles, 2 stay behind. This can be expressed in a filter efficiency of about 13%, i.e. about 13% of the particles are stopped by the filter.

In figure 6.16, the results for the DHS-35-30 model are shown. Again, most particles pass the DHS and the second coarse filter. However, some particles are trapped in the large recirculation zones above the filter (red ellipsoid). In total 6 of the 15 injected particles are hanging in recirculation zones (about 35%). If only single particles are collected in the recirculation zones, they will not cause any problems, however if they can cluster to larger particles and leave the recirculation zone, they might block the filter or even the jets.

Summarised, it can be said that single ideal particles, smaller than the filter mesh spacing will not cause any blocking problems. Ideal particles larger than the filter mesh spacing will be stopped by the filter and hence cause no troubles inside the jets. The cellulose can always pass the blocking particles and so a continuous production of Lyocell fibres is guaranteed.

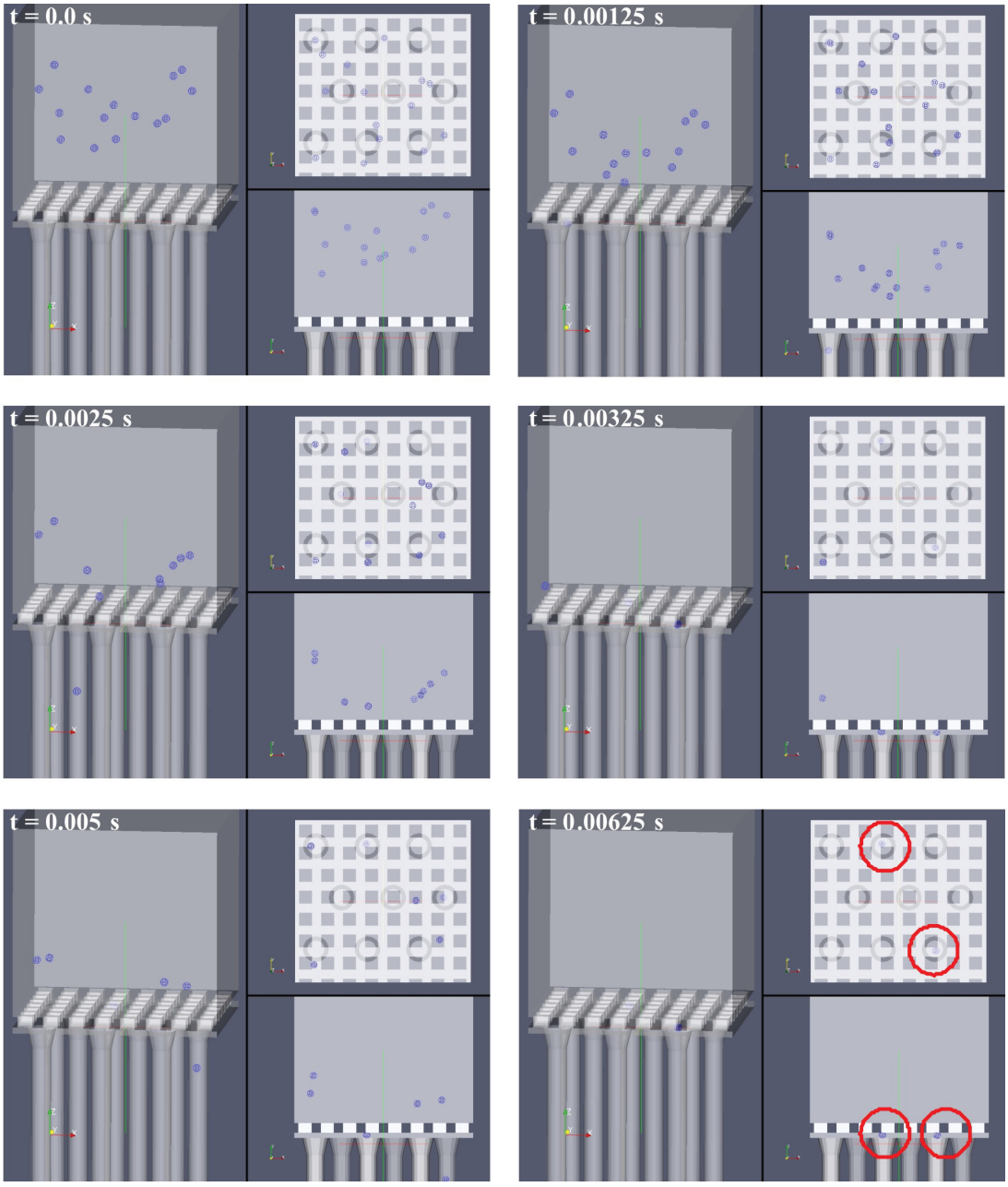

Figure 6.15: General flow of solid ideal particles through the DES and 9 jets, plot of particles in wireframe at 6 different timeframes in isometric view (left), top view (top right) and side view (bottom right).

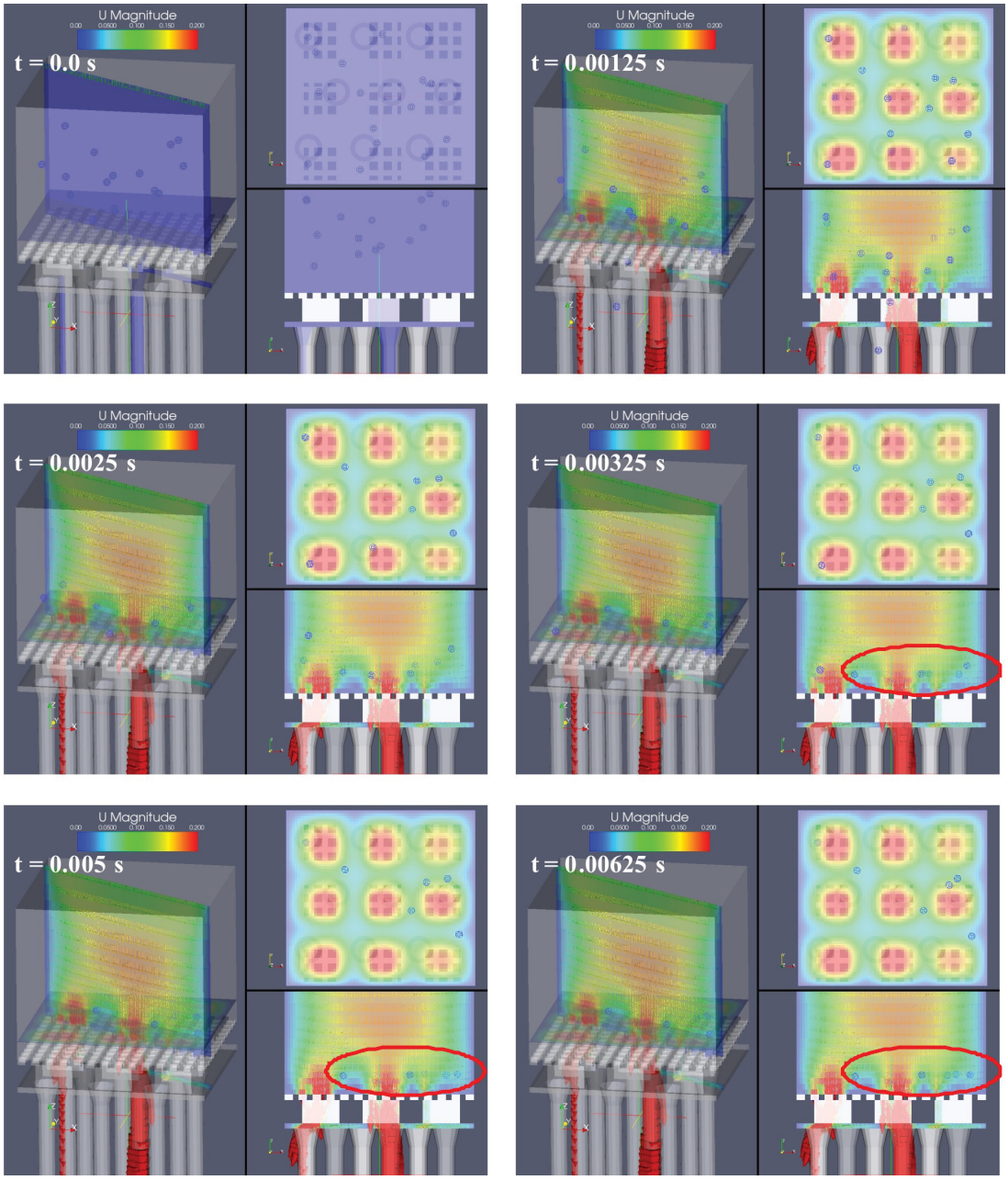

Figure 6.16: General flow of solid ideal particles through the DHS and 9 jets, plot of particles in wireframe at 6 different timeframes in isometric view (left), top view (top right) and side view (bottom right). Contour and vector plot of the velocity magnitude on a surface in Z-direction, contour plot of the velocity magnitude on a surface parallel to the filter.

6.3.2 Real particles

First, a simulation on the 9 jet model without filter (JetConfig-9) is conducted. The results can be found in figure 6.17. After 0.00625 seconds, no particle is left in the model. The residence time of the particles is hence slightly higher than the flowthrough time (0.004s as defined in paragraph 6.2). This is mainly due to the recirculation zones between the jets that slow down the more inert solid particles. At the same time, this indicates the role of filters in the blocking process. Without filters, there is no blocking.

The results for the DES-75-53 and the DHS-35-30 model are plotted in figure 6.18 and figure 6.19. Underneath the DES filter, quite some particles are stuck after 0.00625 seconds (red circles). This agrees very well with the experimental results (see section 3.3.4.3). From the 15 injected particles, 6 stay behind between the filter and the jet. That is about 35% and 3 times higher than for ideal particles. Compared to the ideal particle simulations it can be said that the real particles tend to get stuck underneath the DES filter more than the ideal particles.

As for the ideal particle simulations, the DHS filter traps a lot of particles in the recirculation zones above the filter. For the real particles, only 2 particles (about 13%) are trapped in a recirculation zone (red ellipsoid), but about 7 particles are stopped by the filter. This is almost 50%. In total this means that the DHS filter stops about 65% of the particles with a mean size of 25μm and a standard deviation of 25μm. Since hardly any ideal particles will be present in the cellulose solution [14, 18], it can be stated that the DHS filter works, but not for the full 100%. Note that the filter mesh (35μm^2) is a lot larger than the particles present, so 65% efficiency is not too bad.

Summarised the real particle simulations show that the behaviour of the particles is similar to that of the ideal particles concerning blocking mechanisms, however, the effects for the real particles are more pronounced than for the ideal particles. The DES filter has an efficiency of about 35%, where as the DHS filter has an efficiency of up to 65% for particles with a mean diameter of 25 $\pm$ 25μm.

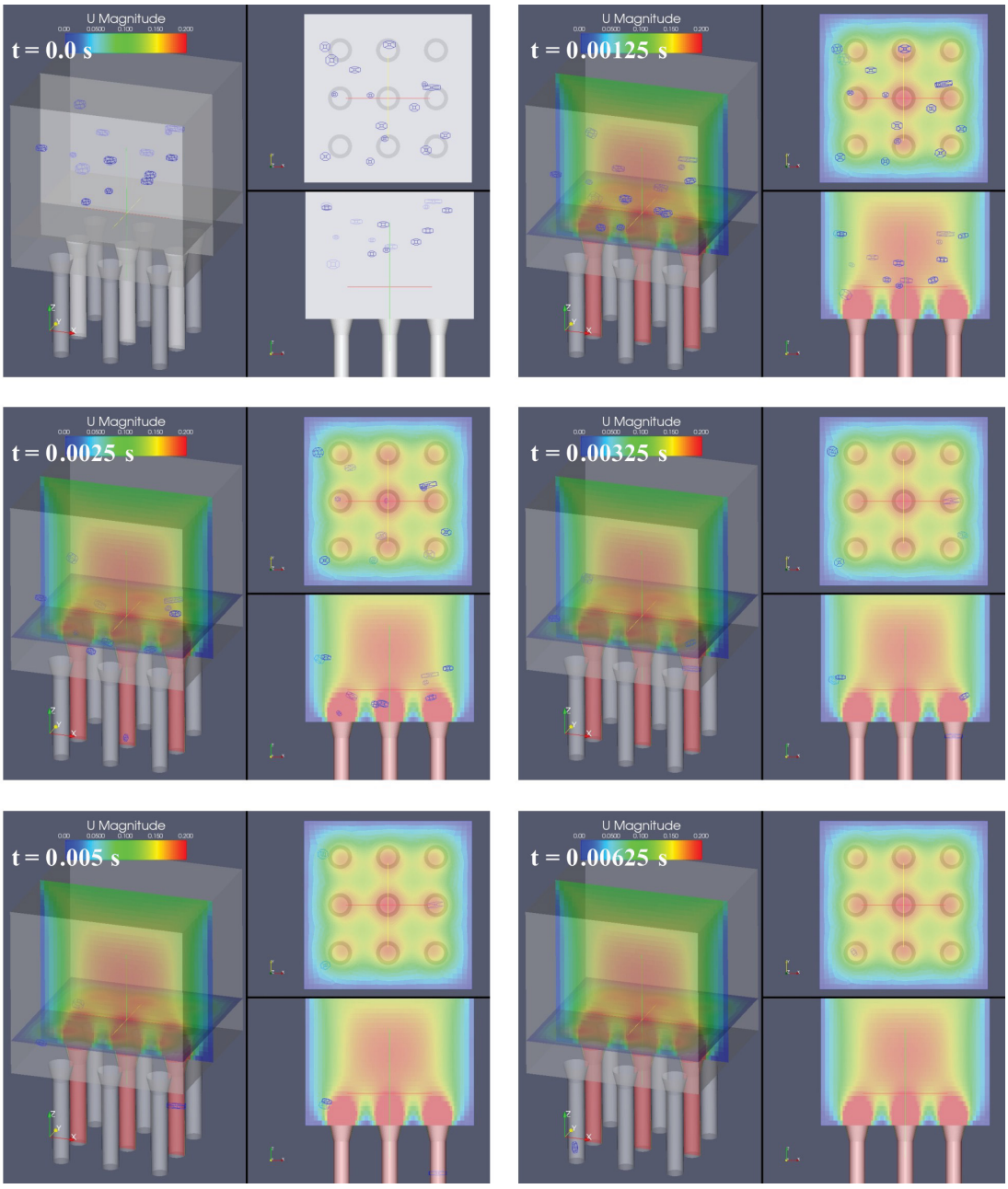

Figure 6.17: General flow of solid real particles through the JetConfig-9 model without filter, plot of particles in wireframe at 6 different timeframes in isometric view (left), top view (top right) and side view (bottom right). Contour plot of the velocity magnitude on a surface in Z-direction and on a surface parallel to the filter.

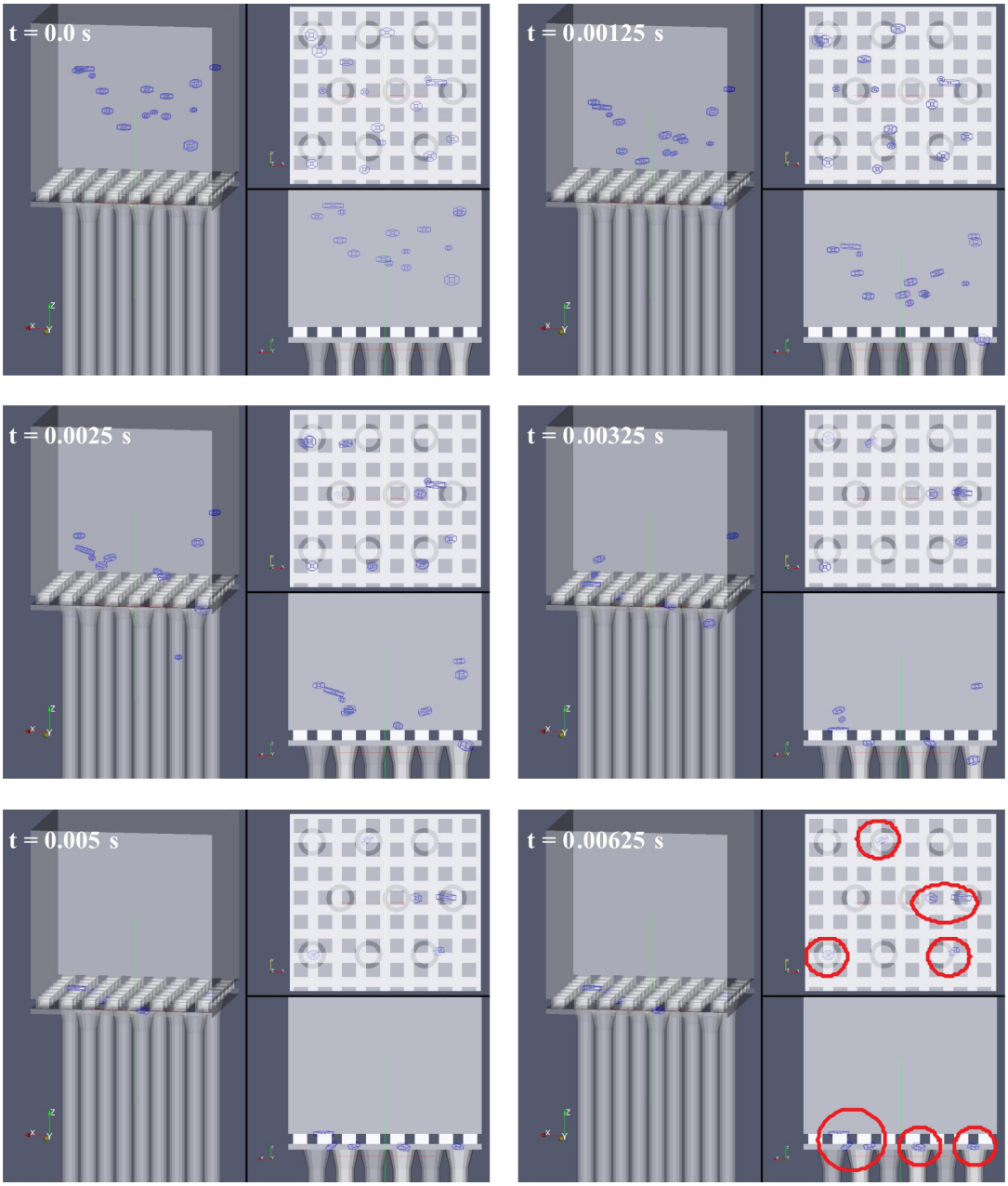

Figure 6.18: General flow of solid real particles through the DES and 9 jets, plot of particles in wireframe at 6 different timeframes in isometric view (left), top view (top right) and side view (bottom right).

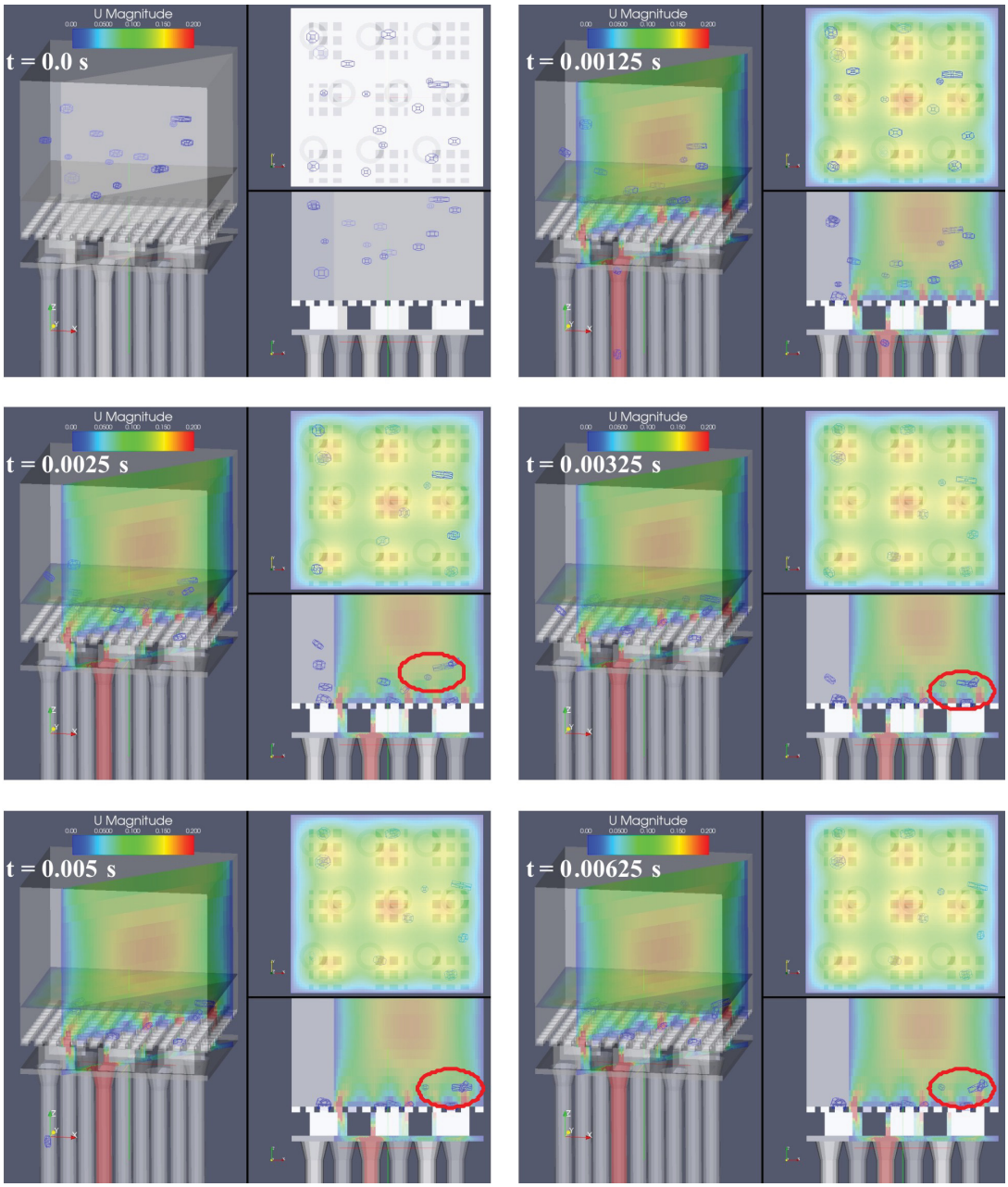

Figure 6.19: General flow of solid real particles through the DHS and 9 jets, plot of particles in wireframe at 6 different timeframes in isometric view (left), top view (top right) and side view (bottom right). Contour plot of the velocity magnitude on a surface in Z-direction and on a surface parallel to the filter.

6.4 KREY

From Computer Tomograph (CT) data, two exact CFD models are created using the reconstruction algorithm created by J. Leixnering (see paragraph 6.4.1)[43]. The first one contains all seven layers of the KREY filter; the second one ignores the very coarse layers at the outer sides of the filter. These models are called *KREY-full* and *KREY-sagital* respectively.

The main question the KREY simulations should answer, is whether the KREY filter takes out all of the particles above a certain size, assuming the filter has no flaws, and if particles that are trapped inside the finer filters can be washed out if the flow through the KREY is reversed. Furthermore, the influence of such complex filters on large gel particles is studied.

In the following paragraphs, first the digital reconstruction of the KREY filter is described. Second, gel particle simulations are shown, and finally the difficulties at simulating real solid particles in the KREY model are explained.

6.4.1 Reconstruction algorithm

The KREY filter exists of 7 filter layers, all of different mesh spacing and wire thickness as described in table 2.1. In figure 2.6 some images of the KREY filter at different positions are plotted. The finest mesh spacing in the centre of the filter is needed to filter out the small particles; the larger filters at both sides of the filter are needed to give the small filters enough strength to withstand the high pressures over the filter, up to 60 bar.

In order to simulate the exact complex geometry of the KREY filter, a Computer Tomograph (CT) scan was made of a clean filter. This scan was delivered in the form of a digital film. The resolution of the filter film was 7μm with 1000 pixels in every dimension. The high quality of the film allowed to perfectly reconstruct the exact filter structure using the reconstruction algorithm of DexaSIM [43].

6.4.1.1 DexaSIM

In the past, extensive research and software development on Diesel exhaust system modelling have been performed The result is the software called Diesel EXhaust gas Aftertreatment SIMulation, in short: *DexaSIM* [20, 21, 24, 29, 52, 58, 60, 61, 67, 68]. DexaSIM in its current experimentally validated development status permits the simulation of filter loading due to soot deposition on a microscopic material level and globally in the exhaust system.

6.4.1.2 Modelling on a microscopic scale

The micro structural geometry generator contained within DexaSIM permits the reconstruction of material samples from 2D Computer Tomography (CT) data. By using statistical functions material samples are mathematically characterised.

6.4.1.3 Anisotropic material reconstruction method

The algorithm used to digitise 2D CT-scans can be used to create anisotropic (real) 3D computational models of any material. The algorithm includes the following steps:

1. Obtain 2D grey-scale images of the material
2. Combine 2D images to one 3D grey-scale image
3. Digitise and reconstruct the 3D digital model or mesh

An example of the reconstruction algorithm is given by the two 3D CFD models of the anisotropic KREY filter created from the 3D CT images. The results are shown in figure 6.20.

A sketch of the CFD model and its boundary conditions is given in figure 6.21. The characteristic velocity is set to 0.5m/s which returns a residence time of 0.0484s. The Reynolds number is 0.1. The amount of cells is very high for both models since the reconstruction algorithm creates hexahedral meshes only, without local refinements. Due to the large differences in filter mesh spacings, which range from 20μm up to 630μm, the finest filter mesh (20μm) defines the maximum cell size. Each model contains about 4 million cells, which makes simulations very slow since parallelising is not possible.

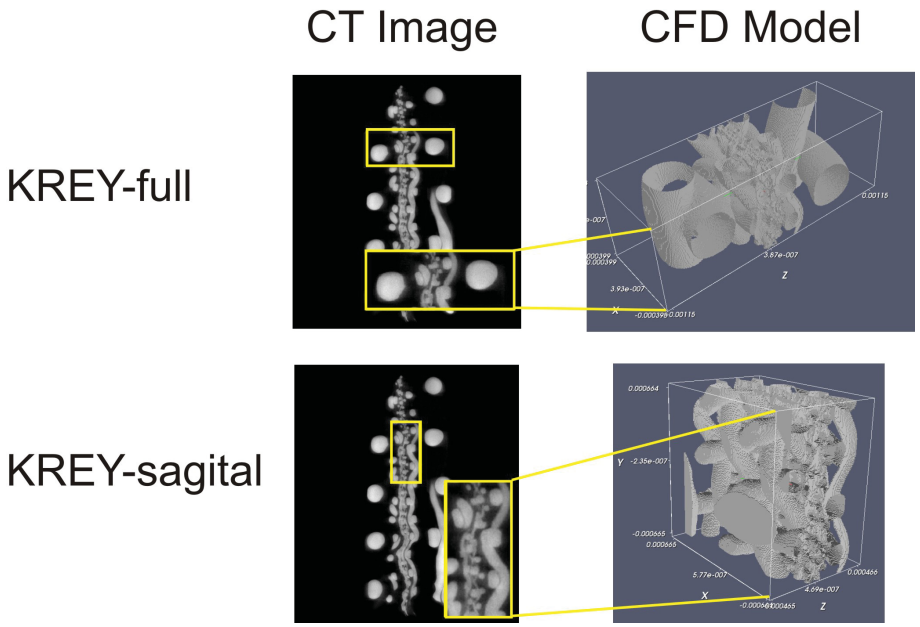

Figure 6.20: Two computational models (right) of 3D CT-scans (left) of the KREY filter

Model					KREY_sagital and KREY_full
			Value	*Unit*	*Sketch*
Dim.	H x W x D		2420 x 840 x 840	µm	
	Gel	Injection at inlet			
	Particle	mean diameter	25 ± 25	µm	
BC	Inlet	Velocity Inlet	0.1	m/s	
	Outlet	Pressure Outlet	0	Pa	
	Wall	No slip wall			
Mesh	Number of cells		~4.000.000		
Solver	icoLagrangianFoam, interFoam				
Goal	Study of complex real geometry				

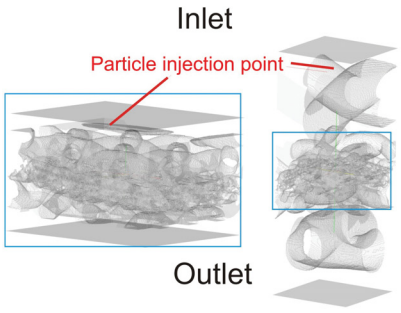

Figure 6.21: Sketch of the control window model used to simulate different viscosity models

The general velocity and pressure fields through both models is shown in figure 6.22 on a plane that cuts through the centre of the models. The effect of the different sized filters and the complex structure becomes very clear.

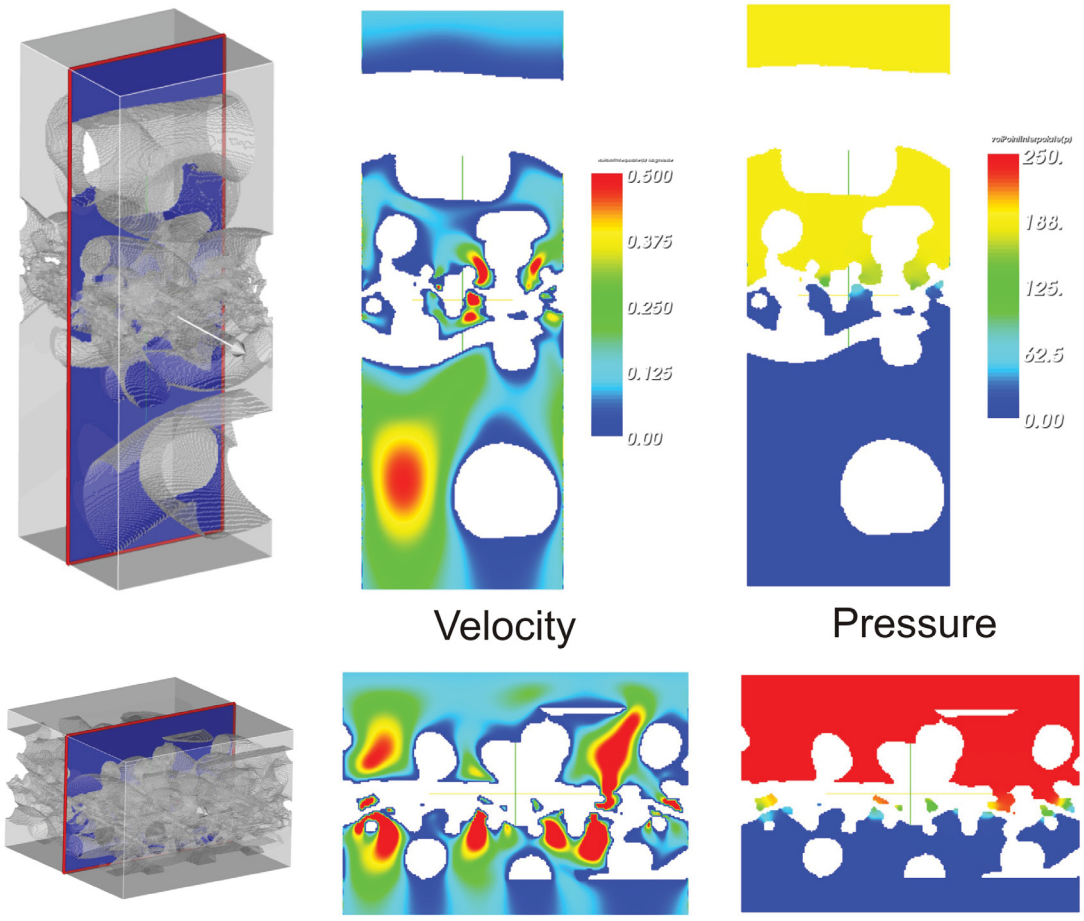

Figure 6.22: Contour plot of the velocity (middle) and pressure (right) fields inside the KREY-full (top) and the KREY-sagital (bottom) models

6.4.2 Gels

Concerning the interFoam solver, it is shown that large gels get cut into a lot of small gels which can cause trouble later on in the spinning process. Depending on the surface tension, more or less gels are stuck inside the KREY filter, causing a rapid pressure rise over the filter. This is illustrated in figure 6.23 and 6.24.

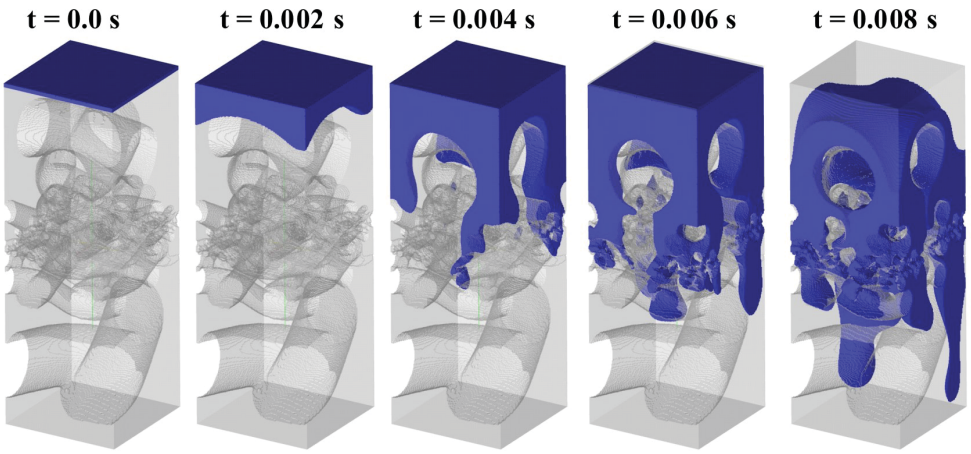

Figure 6.23: Simulation of large gel pressed through the KREY-full model, $\sigma = 0.07$

6.4.3 Large Particles

Since the icoLagrangianFoam solver is not yet parallelised, simulations take over one month on an AMD 2GHz opteron processor (64 bit). Also, since a restart of the solver is not yet possible, if errors were made in the set-up, these could not be detected before the end of the simulation. An example of this is given for the KREY-sagital simulation that is presented in figure 6.25. As soon as the particles reached the centre of the model, they disappeared. It turned out that there was an error in the mesh, but than already 2 months of mesh reconstruction and simulation time had passed.

Figure 6.26 shows the simulation of particles in the KREY-full model. The simulations were stable, but took over two months for 0.0012s of real time.

It can be concluded that simulations of the complex KREY filter with both the interFoam and the icoLagrangianFoam solver are possible. Simulations were stable and show realistic results. However, the simulation time is still too long for direct practical use. This can be improved by parallelising and by adding a restart option for the icoLagrangianFoam solver. For the interFoam solver, the models could be run on larger clusters to speed up the simulations. In this thesis, a maximum of four nodes has been applied.

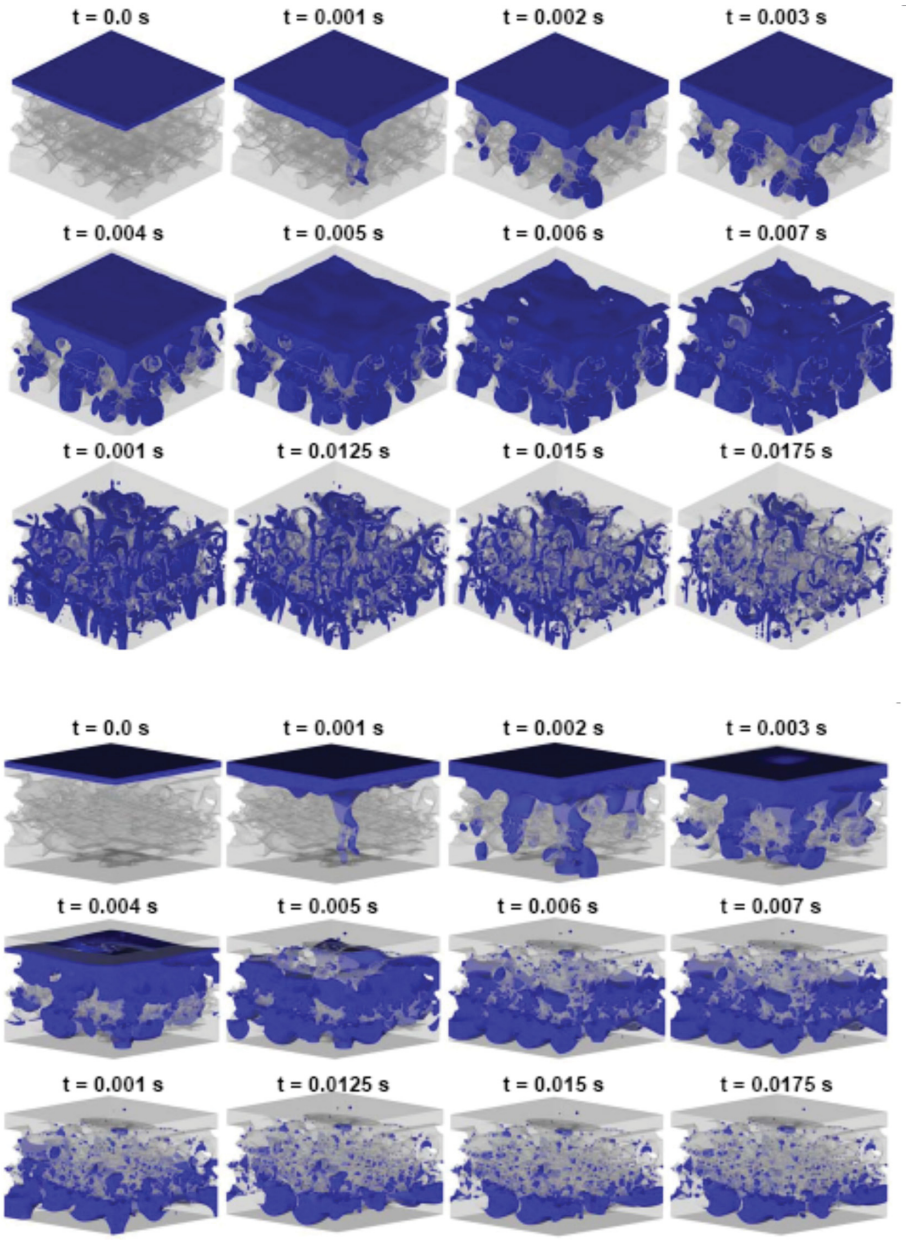

Figure 6.24: Simulation of large gel pressed through the KREY-sagital model for $\sigma = 0.07$ (top) and $\sigma = 7$ (bottom).

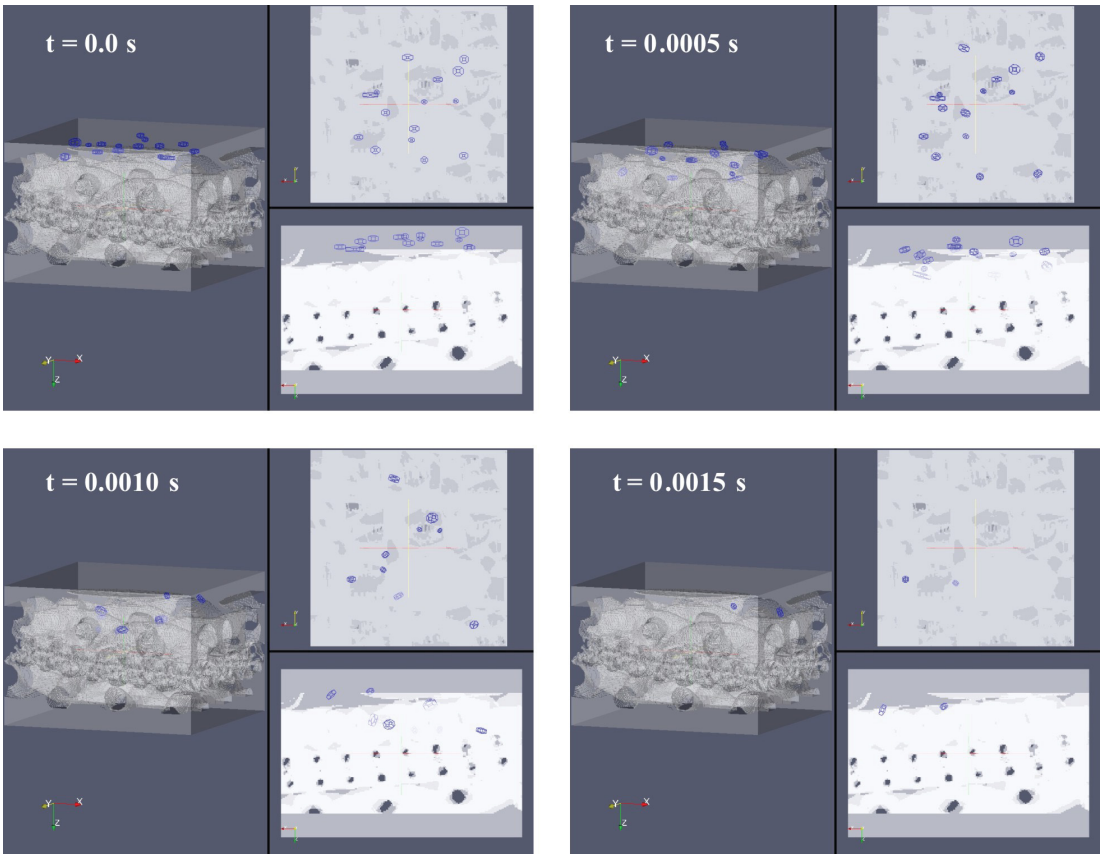

Figure 6.25: Particle simulation of the KREY-sagital model

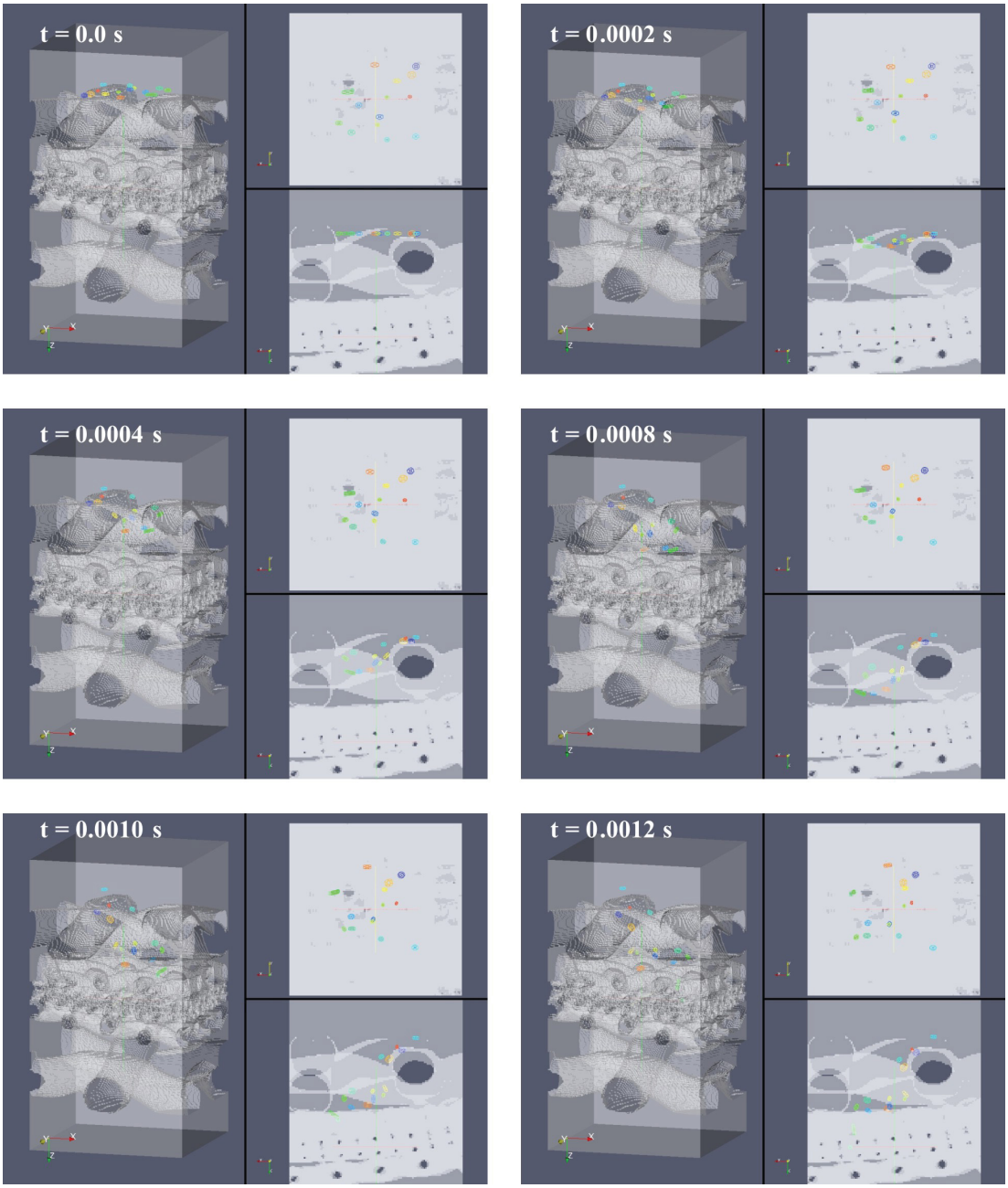

Figure 6.26: Particle simulation of the KREY-full model

Chapter 7

Optimisation

Based on the previous simulations using the interFoam and icoLagrangianFoam solver, the simplified DES and DHS filter and jet situation have been studied on their optimisation potential. The optimisation of these situations will be described in this chapter.

7.1 Study of flow field

For both the DES and DHS filter-jet combinations, the flow field is studied in a qualitative way. Figure 7.1 shows the position of three surfaces on which the velocity field has been plotted. The first two surfaces cut through the centre of the jets. One surface also cuts through a complete filter wire (Y1) whereas the other only cuts perpendicular through the filter wires (Y2). The third surface lies between the bottom of the filter and the inlet of the jets (Z).

From the velocity magnitude contour plots on these surfaces, it is seen that there are large differences in the flow pattern between the DES and the DHS filters (see figure 7.2). Also, the support filter underneath the DHS filters has a major influence on the flow field before, in and after the jet.

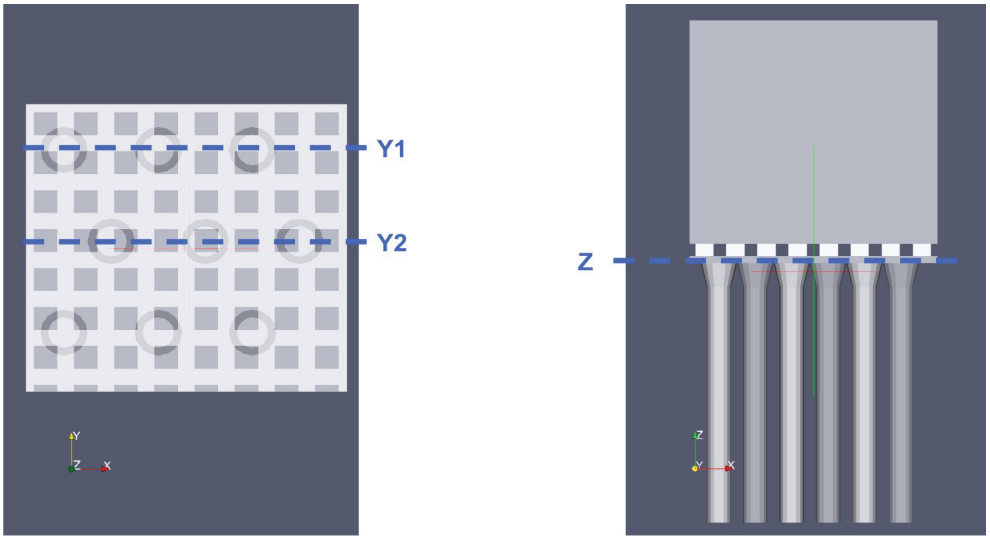

Figure 7.1: Sketch of the surfaces through the DES-75-53 model. Two surfaces cut through the jets. One through a complete filter wire (Y1) and one perpendicular to all filter wires (Y2). The third surface lies between the bottom of the filter and the top of the jet inlets (Z).

7.2 Optimal flow through filter and jet

Looking at figure 7.2, it is clear that the filter spacing and position above the jet has a major influence on the flow field through the filter as well as through the jet. These differences account for different particle and gel behaviour, which is important if searching for the optimal filter and jet shape.

Figure 7.3 and figure 7.4 show in more detail the influence of a filter on the flow field. From these sketches, it becomes very clear that an optimal flow through the filter and hence the jets can only be obtained if the open area above the jet is as large as possible. At the same time, single filters tend to have little influence on the flow field inside the jet and hence double or more complex filters are more suitable for the capturing of particles.

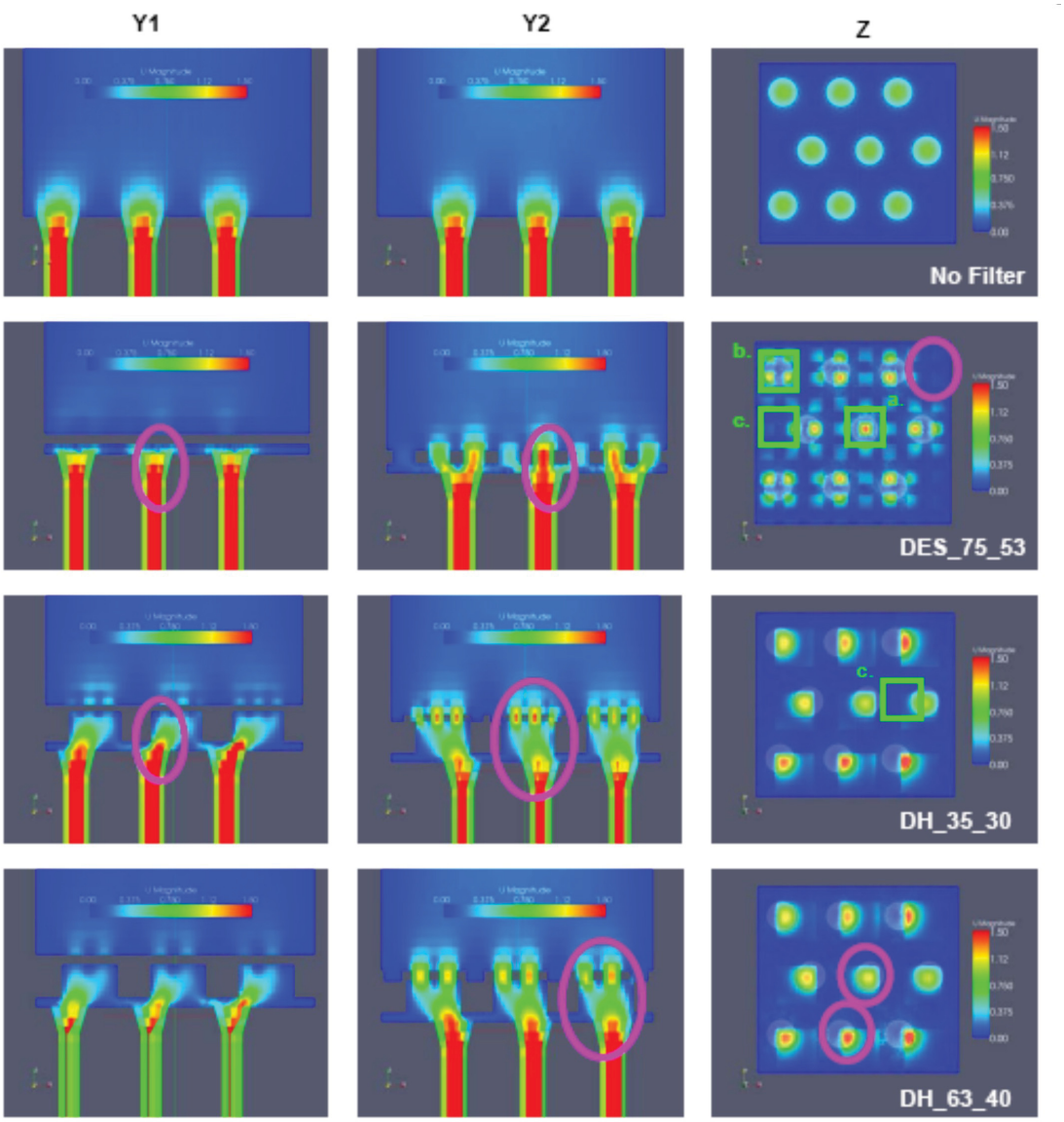

Figure 7.2: Contour plot of the velocity magnitude (flow field) of all three filter models along the three surfaces Y1, Y2 and Z. Zones of interest are marked by pink circles. The regions a., b. and c. inside the green squares are discussed in Figure 7.3.

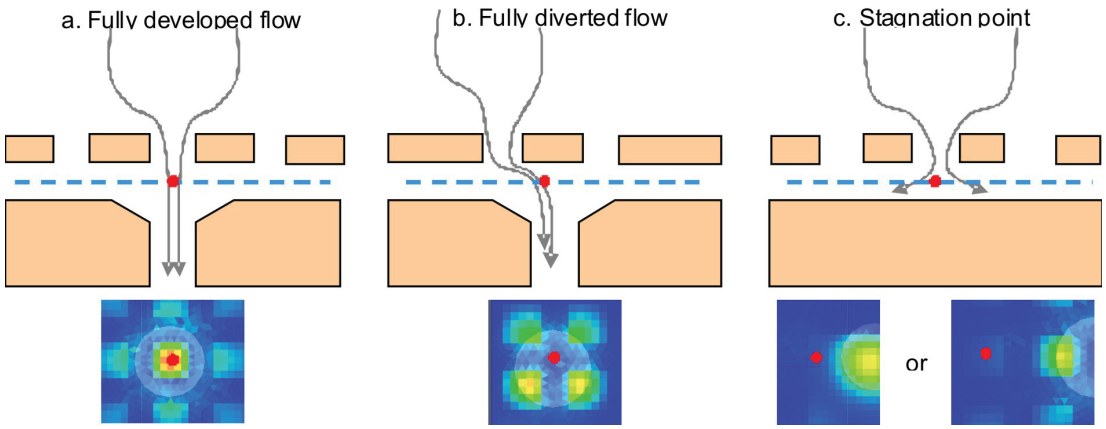

Figure 7.3: Simplified sketches of three extreme situations regarding to the flow field through the filters and the jets.

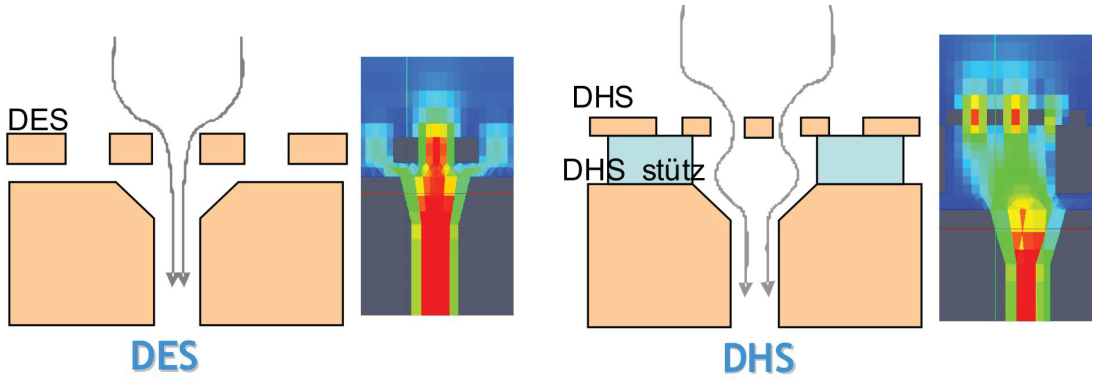

Figure 7.4: Simplified sketches of the influence of single or double filters on the flow through the jets

7.3 Optimisation potential

Looking at the results in chapter 6, large differences in the influence on the flow field are seen between the DES and the DHS filter. As described in section 6.3.2, the dynamics of real particles is quite different from that of ideal particles. Rod shaped particles (prolate particles) can flow through the filters depending on the local flow field, although one dimension is larger than the filter mesh. Real particles can *dance* on the filter, whereas ideal particles lie still as soon as they get stuck on the filter. This can have its influence on the flow field after the filter. Finally, due to the broken symmetry, real particles react more on the recirculation zones around the filters [14].

The DHS filter has a fairly good particle capturing efficiency (about 65%) when it comes to real particles with a mean size of 25μm and a standard deviation of 25μm (see section 6.3). However, it is still not waterproof. The filter efficiency should be improved so that hardly any solid particles will reach the DES filter where they easily can get stuck between the filter and the jets, hence causing spinning errors.

The DES has an efficiency of only 35%. Since this filter is not developed to stop particles, this is not a problem. Should particles get passed the DHS filter, the distance between the DES filter and the jet plate should at least be as large as the filter mesh in order to prevent real particles to get stuck between them.

Figure 7.5 schematically shows the relationship between filter mesh spacing, jet size and particle size concerning the blocking of the filter or the jet. It should be clear from all these situations that the optimization potential lies in the open area of the filter, i.e. d, h and j should be maximised for certain particle sizes (a, b and c). From these theoretical thoughts, the optimisation potential for the interaction between filters and real particles becomes clear:

- For the DHS, situation 1 and 4 are wanted; hence d should be as small as possible, i.e. smallest possible open area above jets.
- For the DES, situation 1, 2, 3, 4, 5 and 6 should be avoided; hence d and h should be as large as possible, i.e. largest possible open area above jets.

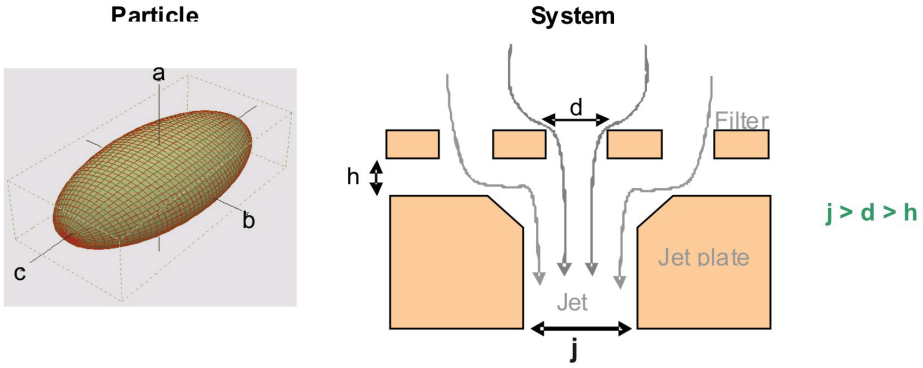

Situation	Condition			Consequence
	I	II	III	
1.	a=b=c > d			Particle blocks filter
2.	a=b=c < d	a=b=c > h		Particle stuck between filter and jet plate
3.		a=b=c < h		Particle passes filter and jet
4.	a=b > d			Particle blocks filter
5.	a=b < d	a=b > h		Particle *might* pass filter, Particle stuck between filter and jet plate
6.		a=b < h	c > j	Particle *might* pass filter, Particle *might* pass jet plate, Particle *might* block jet
7.			c < j	Particle *might* pass filter, Particle *might* pass jet plate, Particle passes jet

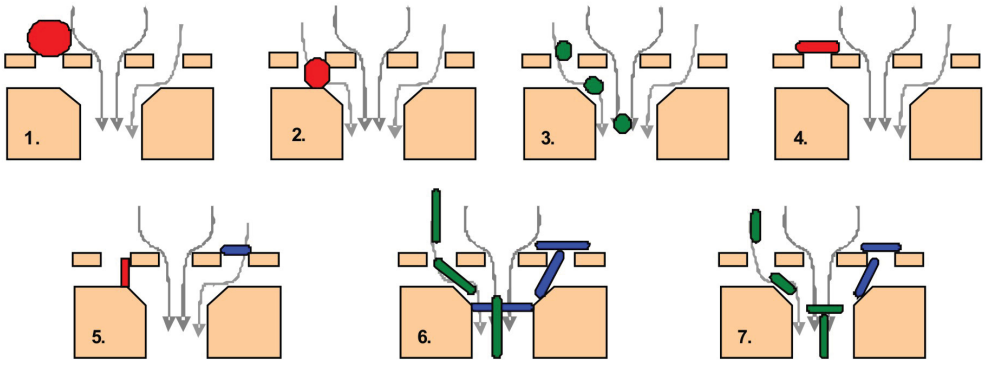

Figure 7.5: Characterization of real particles (left) and the filter-jet system (right). Possible real particle-filter-jet interactions (bottom)

Both filters seem to slow down large gel particles which might become a problem if a lot of dirt is present in the cellulose solution. The open area above the jets should be maximised in order for large gel particles to pass the filters as soon as possible. Gel particles larger than the filter mesh or the jets with high surface tension can block either the filter or the jet directly. A combination of large gel particles which pass through the filter with some delay due to a higher resistance than the cellulose solution might trap solid particles and block the filters or the jet.

In order to prevent blocking of the filter, the amount of possible surfactants or solid particles that can get trapped by gel particles must be minimised. The open surface above the jets should be as large as possible so that small gel particles can pass and large gels have a smaller residence time on the filters. This minimizes the chance to trap solid particles.

If we look at the simplified filter shapes (not woven, quadratic mesh) we see that there are two extreme situations of the position of the filter over the jet which determine the flow through the filter (see figure 7.6):

- Open area (grey) lies exactly above jet (red), this situation is called MAX
- Wire cross (black) lies exactly above jet (red), this situation is called MIN

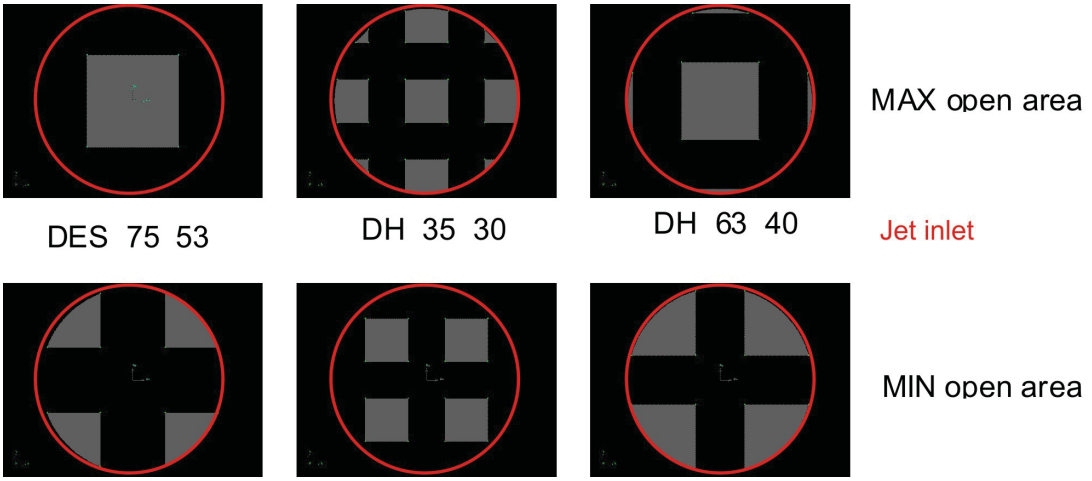

Figure 7.6: Minimum and maximum flow through area of filter-jet combination

The optimisation potential of both the DES and the DHS filter is an optimal spread between the MIN and MAX situation of the open area above the jet as shown in figure 7.7. The optimal DHS and DES filter for both solid and gel particles are defined as:

- DES
  - Let particles smaller than the filter mesh pass
  - Not delay large gel particles in order to have a continuous fibre production
  - Have a large spread between minimum and maximum open area
  - Divide cellulose homogeneous over the jet plate, i.e. spreading filter
- DHS
  - Hardly any spread between minimum and maximum open area
  - Filter out as much particles as possible, particle filter

7.4 Variational optimisation

In order to optimise either the filter mesh or the jet size, the parameters that can or should be optimised must be defined. These parameters are used to create a parameterised CFD model. Finally, an optimisation criterion is defined in order to determine what is optimal for a given situation.

Automatic optimisation algorithms such as the SIMPLEX method [57] can trace the optimal filter mesh or jet size by changing the parameters in the parameterised model according to certain rules. However, the results of such simulations often return a value that in theory is the optimum, but can not be manufactured practically. An optimisation of the filter mesh for example could return the optimal value of 25.4475μm. If meshes can only be made with an accuracy of 1μm, it is unclear whether the optimal solution would be 25μm or 26μm.

In order to avoid such a theoretical solution to come forward, the optimisation has been conducted using a variational approach. This means that all technically possible values for the parameters in the parameterised model are written in a list and every possible combination of these parameters is simulated.

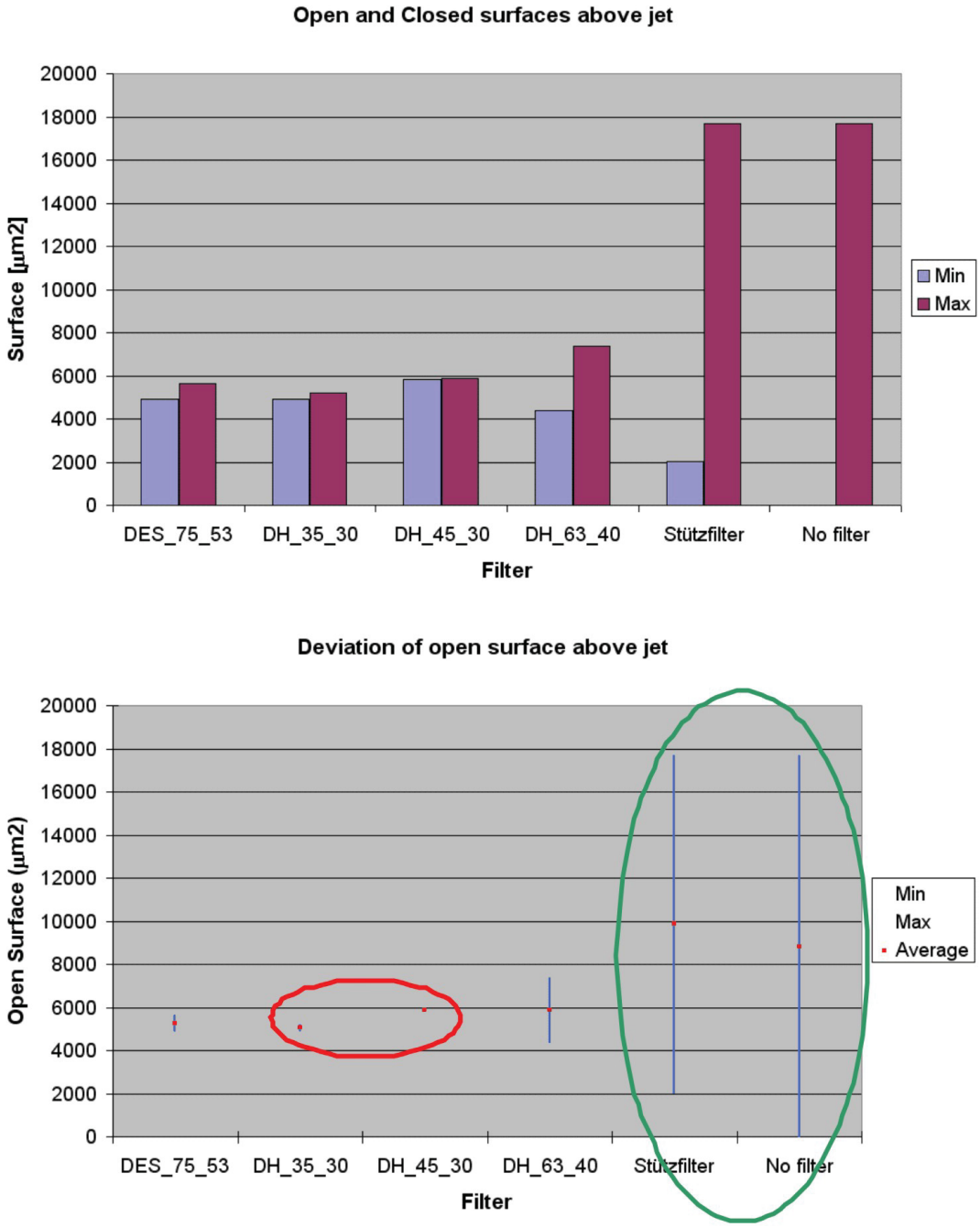

Figure 7.7: Spread of open area; difference between minimum and maximum open surface for a range of applied filters in the Lyocell process

7.4.1 Filter optimization

In case of the filters, the surface containing all the optimised open areas must be found. As has been described above, the open area should be maximised or minimised, depending on the exact function of the filter. If a filter is placed randomly on top of the jets, two different extreme situations can occur see figure 7.6. The filter might lie exactly on top of a jet (MIN open area) or the crossing of two wires might lie as far away as possible from the centre of the jet (MAX open area).

Two parameterised models for the MIN and MAX situations with variational parameters for the wire thickness and the mesh spacing have been created. Both situations are sketched in figure 7.8, based on the parameterised model for both a wire thickness and a filter mesh of 25μm. The optimisation criterion for these models is now to find the exact surface describing the open area difference between the MIN and the MAX situation. Since this difference should be either maximised (DES filter) or minimised (DHS filter) there is no absolute optimum. Each new situation or each new cellulose might demand a slight adjustment of the optimal filters and their open area difference. A complete map showing all the open area differences will allow the operator to choose the appropriate filter depending on the situation at hand.

The parameterised model consists of two variable parameters; the wire thickness and the mesh spacing, i.e. the space between two consecutive wires. They can vary according to the possible sizes the manufacturer can create. These are:

- **wire [μm]** 25, 30, 35, 36, 40, 53, 56, 60, 63, 80, 100, 125, 150, 160, 200, 250, 260, 300, 320, 370, 400, 500, 630, 700, 800, 900, 1.000, 1.400 and 1.600
- **mesh [μm]** 25, 33.5, 36, 42, 50, 58, 63, 67, 74, 87, 90, 100, 125, 160, 200, 250, 315, 380, 400, 500, 610, 630, 800, 950, 1.000, 1.200, 1.250, 1.490, 1.600, 2.000, 2.250, 2.020, 2.500, 2.480, 3.000, 4.000, 4.200, 4.750, 5.000, 6.000, 8.000 and 10.000

In total, this leaves 1260 possible combinations and hence 1260 different simulations to be conducted. For this reason, the mesh spacing is kept small. A

maximum of 15.000 elements is used to calculate the open area of the filter-jet combination.

In order to find the optimal surface, the MIN and the MAX open area of each combination (hence 2520 calculations) is calculated and their difference is plotted in figure 7.9. Note that as soon as the filter mesh and the wire thickness exceed 150μm the open area difference equals the area of the jet inlet, i.e. $\pi r^2 = 3.1415\dot{(}75)^2 = 17671\mu m^2$. Therefore, only the range of [0, 200] has been plotted for both parameters.

This surface now shows a clear map of the amount of open area of each wire-mesh combination, hence giving the operator of the Lyocell plant the freedom to pick the appropriate filter for each situation. A maximum open area should be applied to the DES situation and a minimum open area can be applied to the DHS and KREY situation, taking into account that a smaller open area also means a higher pressure drop over the filter.

Note that a change in wire thickness for a constant mesh spacing has more influence on the filter behaviour than vice versa. Especially for the DES filter, a larger wire thickness will improve the filter's function.

7.4.2 Jet optimization

In case of the jets, a maximum uniform flow above and through each jet is desired. This would mean a homogeneous flow through the complete spinneret and very little to no dead zones where particles can accumulate and cause blocking effects.

The variable parameters for each jet are the inlet radius and the height of the inlet cone of the jet. These are illustrated in figure 7.10. According to the geometrical dimensions of the jets, the following radius and heights are possible:

- **radius** [μ**m**] 50, 55, 60, 65, 70, 75, 80, 85, 90, 95, 100, 105, 110, 115, 120, 125, 130, 135, 140 and 145
- **height** [μ**m**] 50, 100, 150, 200, 250, 300, 350, 400, 450, 500, 550, 600, 650, 700, 750, 800, 850, 900 and 950

Note that the parameters all have been varied with equidistant steps. No manufacturing variations of the parameters are known hence a logical change in size has been assumed. In total, this leaves 380 possible combinations or 380

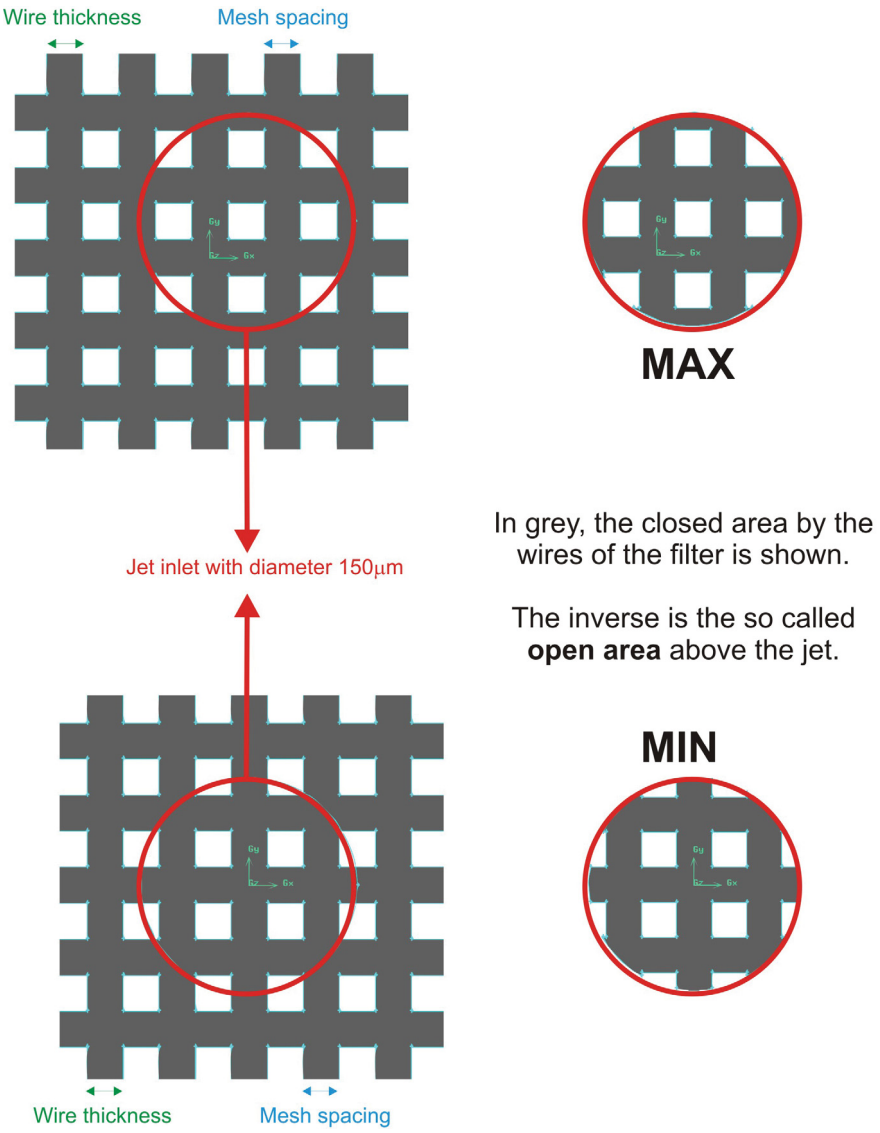

Figure 7.8: Sketch of the parameterised filter models for the minimum (MIN) and maximum (MAX) open area above the jet

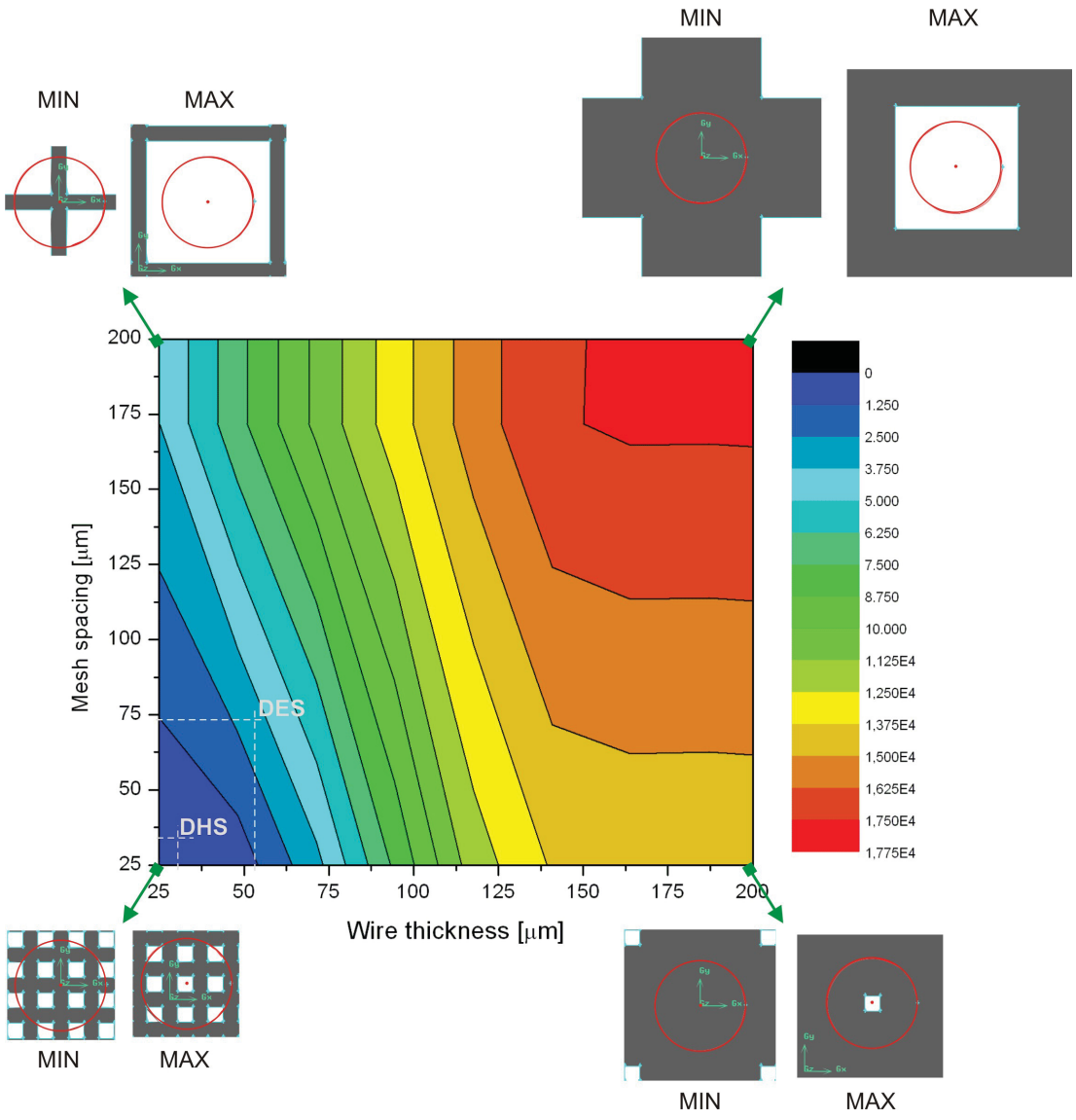

Figure 7.9: Difference in MIN and MAX open area in μm for all possible wire thicknesses and mesh spacings in the range of 25μm up to 200μm

different simulations to be conducted. Again, the number of cells has been limited to 50.000.

The optimisation criterion for these simulations is a maximum homogeneity of the flow above and through the jets. The influence of the flow field above the jets is illustrated in figure 7.2 whereas the importance of a homogeneous flow through the jets can be seen in figure 7.3 and 7.4. Homogeneous flow has been defined as a flow with the least deviation of all flow velocity components from the average axial flow velocity through the jet. For each model, the average axial flow velocity is calculated on the optimisation surface as defined in figure 7.10. On this surface, the axial velocity (z-direction) in each cell is compared to this average axial velocity whereas the x and y velocities are squared and summed up. The sum of the deviation of the z velocities for all cells compared to the average z-velocity and the squared x- and y-velocities must be minimised. This would mean that the flow above and through the jet is as axial and uniform as possible. The same boundary conditions as for the simulations in chapter 6 are used. The optimisation surface is plotted in figure 7.11.

From these results it is seen what the influence of changing the cone height or the jet radius is. For a constant cone height, changing the jet radius will gradually improve the flow through the jet up to a jet radius of about 100μm for small cone heights (<200μm). For larger heights, the improvement remains nearly constant. However, looking at a constant jet radius and changing the cone heights, it is clear that the flow can improve massively for large jet radii. In general, it can be concluded that the largest improvement in homogeneous flow through the jets can be obtained by maximising the jet radius with a minimum cone height of 200μm.

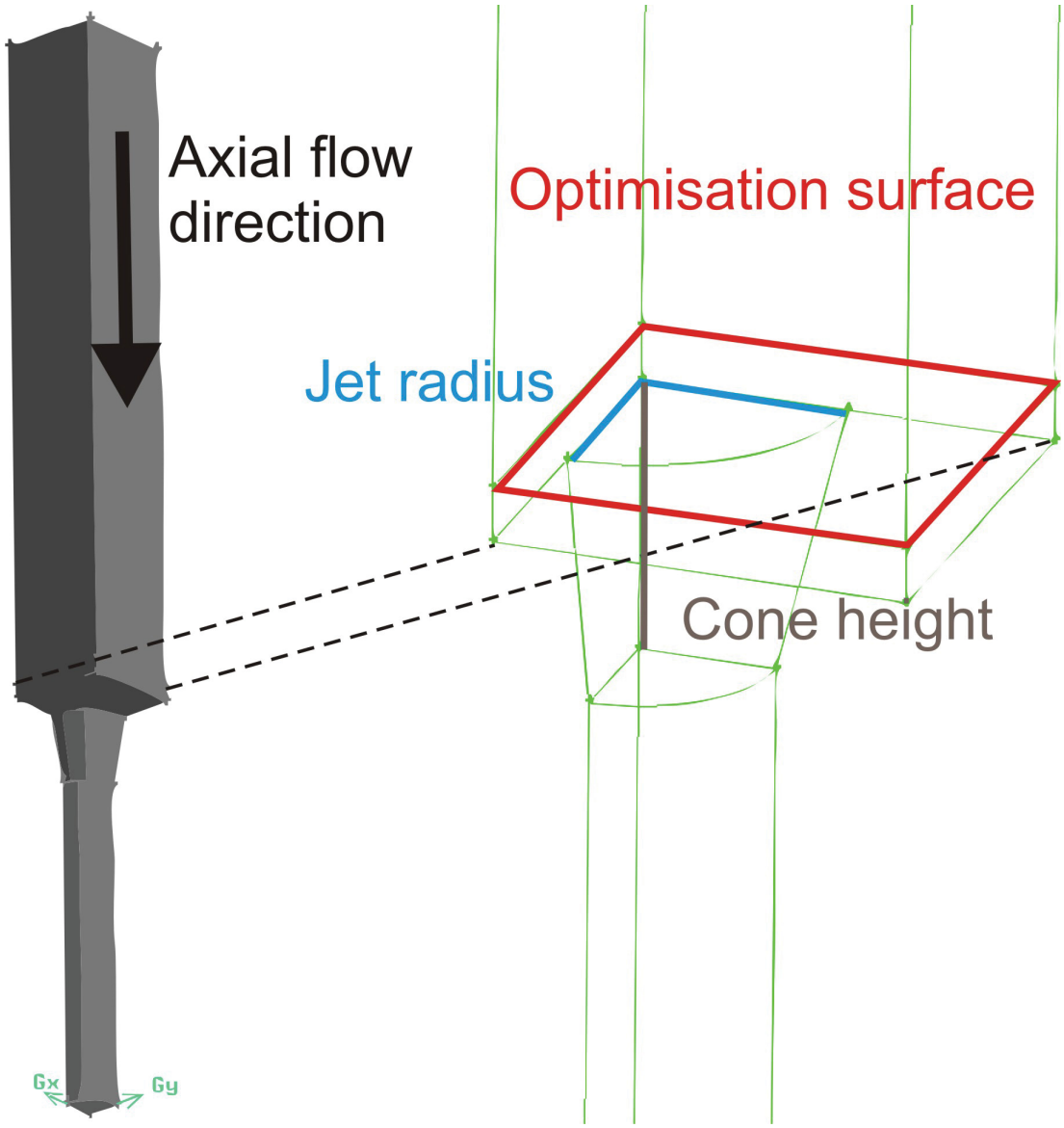

Figure 7.10: Sketch of the jet parameterised model showing the optimisation surface and the two optimisation parameters

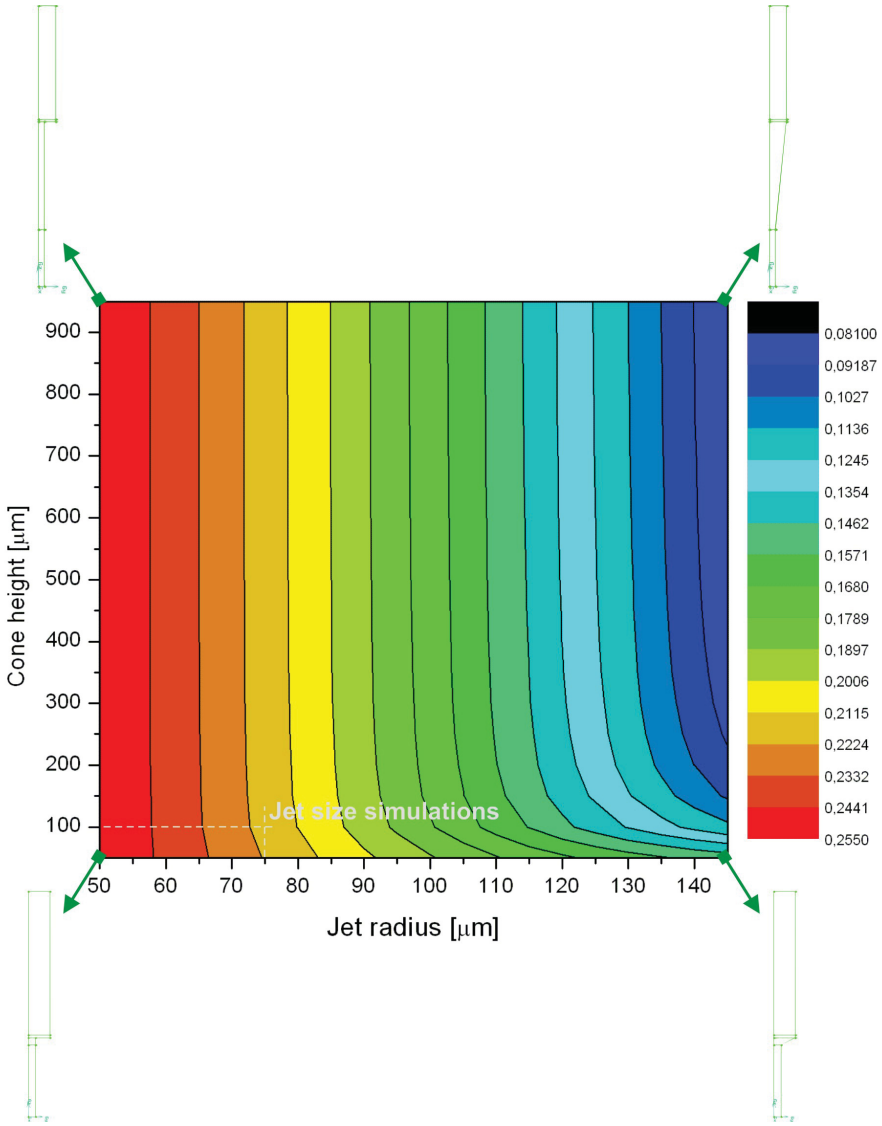

Figure 7.11: Surface showing the minimum (blue) and maximum (red) deviations of all flow velocity components from the average axial flow velocity through the jet.

Chapter 8

Conclusions

8.1 Final Conclusions

Starting with a general study of the Lyocell process, this thesis ended with the local optimisation of the used filter and spinneret system of that same process. It can be concluded that the assumptions that only small ($<50\mu$m) sand particles can reach the spinneret and gels do not cause any blocking problems are an underestimation of the complex situation at hand.

Due to defects (leaking and breathing) in the KREY and DHS filter, solid particles can reach the DES filter and block the spinning process. Both the experiments and the simulations showed that quite some particles get stuck underneath the DES filter. The DES filter has an efficiency of about 35%, where as the DHS filter has an efficiency of up to 65% for particles with a mean diameter of $25 \pm 25\mu$m.

Gel particles cause blocking, albeit not in the same abrupt manner as solid particles do. However, the combination of gels and solid particles is even more dangerous for the permeability of the spinneret.

The function of the DHS and the DES filter has been studied and it can be concluded that the DHS filter should be optimised as a filtering element with a minimum of open area whereas the DES filter should have a large open area. The exact dimensions depend on the degree of impurities in the dope and the

compromise between a the open area and the pressure drop over the filter. Note that a change in wire thickness for a constant mesh spacing has more influence on the filter behaviour than vice versa. Especially for the DES filter, a larger wire thickness will improve the filter's function.

At the same time, the inflow of the jets in the spinneret has quite some optimisation potential. For a constant cone height, changing the jet radius will gradually improve the flow through the jet up to a jet radius of about 100μm for small cone heights (<200μm). For larger heights, the improvement remains nearly constant. However, looking at a constant jet radius and changing the cone heights, it is clear that the flow can improve massively for large jet radii. Hence, the diameter of the inlet should be as large as possible and the inlet cone height should exceed 200μm. All these requirements can technically be implemented in the Lyocell process.

8.2 General remarks

Based on the work done from 2005 to 2008 [7–18], two major solvers have been created and thoroughly tested on the studied filter situations. It is now possible to simulate solid and gel particles in large and complex geometries in order to study the flow behaviour of the particles in these systems.

Experts on all different fields of interest have contributed to this work and without them it would probably not have been as successful. However, combining all this expertise in one closed theory was a challenge that the author has accepted with great gratitude.

8.3 Future Work

Although a lot of work has already been done, there are a few areas of interest that might need some extra attention:

1. The icoLagrangianFoam solver should be parallelised in order to speed up the simulations of large and complex geometries.

2. The interFoam and icoLagrangianFoam solver could be combined to have only one solver. However, more details must be known on the interaction between gels, particles and cellulose as well as some basic material properties of the cellulose.
3. The non-Newtonian model created in FLUENT by Mr Gruber [28] should be implemented in OpenFoam in order to have an even more exact simulation of the rheological behaviour of the cellulose. The simplistic non-Newtonian models present in OpenFoam will not be sufficient to simulate the complex behaviour of the cellulose.
4. Using the multiphaseInterFoam solver, some basic experiments with cellulose, air and thermoplastic polymer solutions called polyketones or Polyetheretherketone (PEEK) could be conducted on a lab scale. This multiphase solver could help explaining phenomena that are seen at the outlet of the spinneret where the dope-gel-solid-particle mixture enters the air flow of the cooling system.
5. As soon as the KREY filter can be simulated in a fast and accurate manner, this filter should be optimized too.
6. Finally, since the mechanisms of blocking are understood, any kind of arrangement of jets and filters can be optimised using the strategy described in chapter 7.

A long time ago, in a empire far far away, known beyond its borders for its culture and power, there ruled an emperor both feared and honoured for his great wisdom and just ruling. One day, the emperor decided to have the best artist in the empire to draw a majestic image of a rooster, the animal adored throughout the empire for its blinding beauty and great taste. He went to visit the artist and asked him how long it would take him to draw a fierce rooster. "One year", the artist mumbled. The emperor, although surprised by the long time it takes to draw one rooster, agreed for a great piece of art can not be conceived over night.

One year later, the emperor returned to the artist and asked him for the painting. "Just a moment", the artist replied and with a few strokes he drew a magnificent rooster. The emperor had to admit that it was a fantastic drawing, but he felt betrayed by the artist. Why did he have to wait one year for a drawing the artist could make in a few minutes!

The emperor screamed for his guards to execute the artist on the spot, but before the swords of the guards could do their murderous job, the artist begged for forgiveness and asked the emperor for one last wish. He would like to show the emperor his gallery where he kept all of his drawings. The emperor, curious about what he was going to see, agreed.

The artist took the emperor to a very small door, but when it was opened, an enormous room filled with drawings and sketches of the fantastic rooster displayed itself to the emperor. "You see majesty", the artist silently said, "I could only have drawn that rooster for you in a few minutes, because I have been practising every stroke of my pencil for the last year..."

Unknown source

Appendix A

Microscopy in all its glory

This appendix describes briefly all microscopical techniques used in this thesis.

A.1 Optical Microscopy (OM)

The polarizing microscope used for the experiments in this thesis has an enlargement of 500x and is equipped with a rotating stage and two polarizing filters, one below the stage and the other above it (see left hand side of figure A.1). Ordinary light may be considered to consist of waves vibrating in all directions whereas polarized light consists of vibrations in one plane only, the plane of polarization.

The polarizing filters in the microscope are normally set so that their polarization directions are at right angles to one another and parallel to the cross-wires in the eyepiece of the microscope. The polarizing filter below the stage is known as the polariser, that above the stage is the analyser. The analyser is mounted in such a way that it can be removed from the light path so that the rock section can be studied in plane-polarized (PP) light. When the analyser is inserted the sample is said to be observed with crossed polars (CP).

To describe a mineral and identify it correctly, one must be able to describe the shape of the crystals, note their colour and change in colour on rotation of the stage, note the presence of one or more cleavages, recognize differences in

refractive index and observe the interface colour with crossed polars [46]. The scale of all the images used is depicted in figure A.1, so each OM figure in this thesis has a horizontal width of about 340μm.

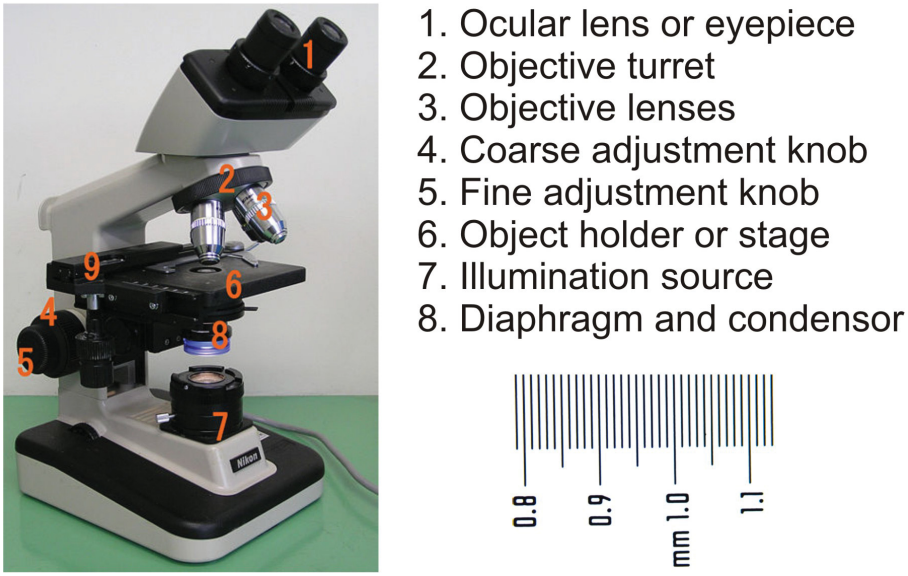

Figure A.1: Illustration of optical microscopy, including the scale of the images made for this thesis

A.2 Raman Spectroscopy (RS)

Raman spectroscopy (RS) is a spectroscopic technique used in condensed matter physics and chemistry to study vibrational, rotational, and other low-frequency modes in a system. It relies on inelastic scattering, or Raman scattering of monochromatic light, usually from a laser in the visible, near infrared, or near ultraviolet range. Photons or other excitations in the system are absorbed or emitted by the laser light, resulting in the energy of the laser photons being shifted up or down. The shift in energy gives information about the phonon modes in the system.

The Raman effect occurs when light impinges upon a molecule and interacts with the electron cloud of the bonds of that molecule. The incident photon excites

one of the electrons into a virtual state. For the spontaneous Raman effect, the molecule will be excited from the ground state to a virtual energy state, and relax into a vibrational excited state, which generates Stokes Raman scattering. If the molecule was already in an elevated vibrational energy state, the Raman scattering is then called anti-Stokes Raman scattering. This is illustrated in figure A.2.

A molecular polarizability change, or amount of deformation of the electron cloud, with respect to the vibrational coordinate is required for the molecule to exhibit the Raman effect. The amount of the polarizability change will determine the Raman scattering intensity, whereas the Raman shift is equal to the vibrational level that is involved.

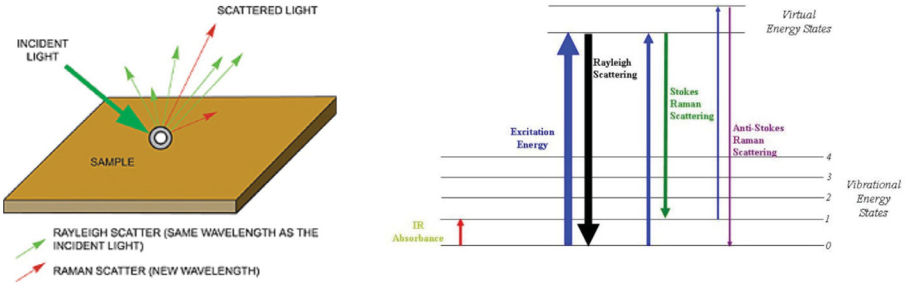

Figure A.2: Sketch of Raman scattering (left) and the Raman energy levels (right)

A.3 Scanning Electron Microscopy (SEM)

Scanning Electron Microscopes (SEM) are scientific instruments that use a beam of highly energetic electrons to examine objects on a very fine scale. This examination can yield the following information:

- **Topography** The surface features of an object or *how it looks*, its texture; direct relation between these features and materials properties (e.g. hardness and reflectivity)

- **Morphology** The shape and size of the particles making up the object; direct relation between these structures and materials properties (e.g. ductility, strength and reactivity)
- **Composition** The elements and compounds that the object is composed of and the relative amounts of them; direct relationship between composition and materials properties (e.g. melting point, reactivity and hardness)
- **Crystallographic Information** How the atoms are arranged in the object; direct relation between these arrangements and materials properties (e.g. conductivity, electrical properties and strength)

Electron Microscopes function exactly as their optical counterparts except that they use a focused beam of electrons instead of light to *image* the specimen and gain information as to its structure and composition.

Figure A.3 shows a sketch of the SEM principle. A beam of electrons is generated in the electron gun, located at the top of the column, which is pictured to the left. This beam is attracted through the anode, condensed by a condenser lens, and focused as a very fine point on the sample by the objective lens. The scan coils are energized by varying the voltage produced by the scan generator and create a magnetic field which deflects the beam back and forth in a controlled pattern. The varying voltage is also applied to the coils around the neck of the Cathode-Ray Tube (CRT) which produces a pattern of light deflected back and forth on the surface of the CRT. The pattern of deflection of the electron beam is the same as the pattern of deflection of the spot of light on the CRT.

The electron beam hits the sample, producing secondary electrons from the sample. These electrons are collected by a secondary detector or a backscatter detector, converted to a voltage, and amplified. The amplified voltage is applied to the grid of the CRT and causes the intensity of the spot of light to change. The image consists of thousands of spots of varying intensity on the face of a CRT that correspond to the topography of the sample.

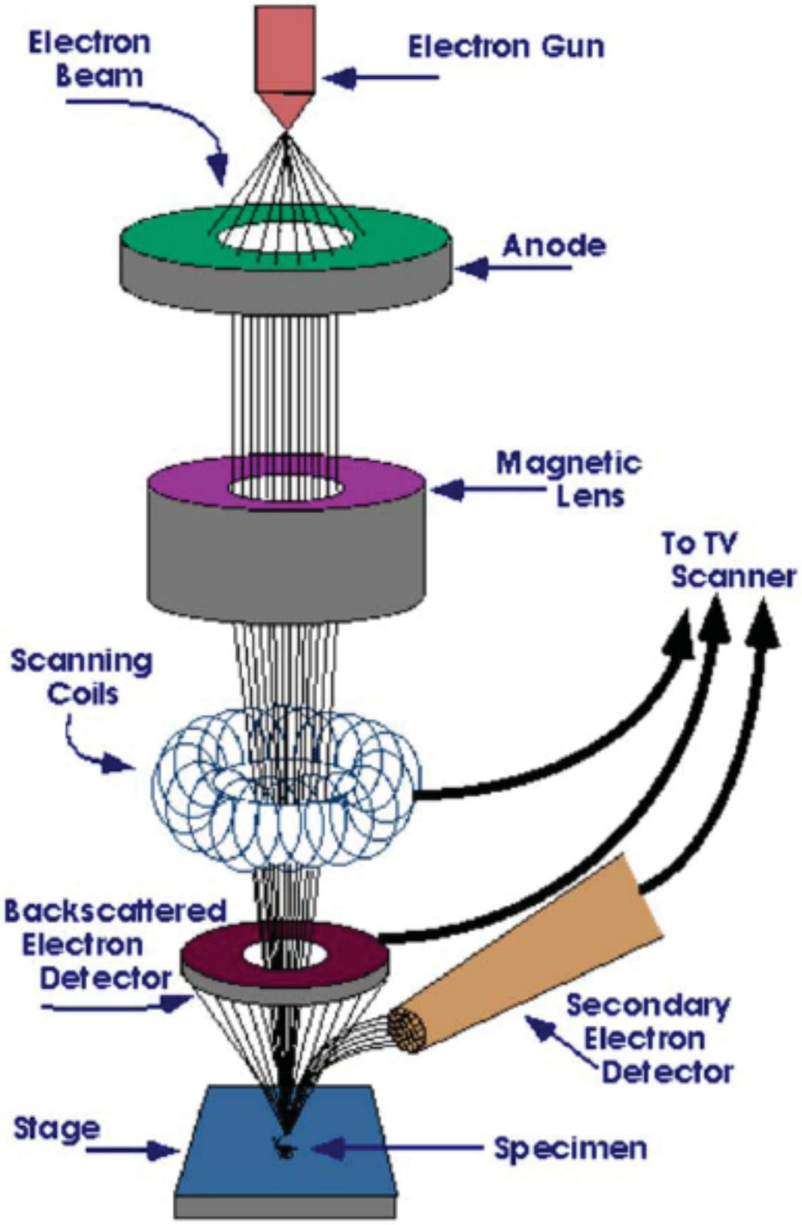

Figure A.3: Simplified sketch of SEM function

Appendix B

Parameterised Models

B.1 Filter MAX parameterised model

```
/Parameters
$wire = 25
$mesh = 25

/create jet
face create "jet" radius 75 xyplane circle
face move "jet" offset (($wire+$mesh)/2) (($wire+$mesh)/2) 0

/create filter
face create "X-wire0" width $wire height ($mesh*$wire) xyplane rectangle
face create "X-wire1" width $wire height ($mesh*$wire) xyplane rectangle
face create "X-wire2" width $wire height ($mesh*$wire) xyplane rectangle
face create "X-wire-1" width $wire height ($mesh*$wire) xyplane rectangle
face create "X-wire-2" width $wire height ($mesh*$wire) xyplane rectangle

face create "Y-wire0" width ($mesh*$wire) height $wire xyplane rectangle
face create "Y-wire1" width ($mesh*$wire) height $wire xyplane rectangle
face create "Y-wire2" width ($mesh*$wire) height $wire xyplane rectangle
face create "Y-wire-1" width ($mesh*$wire) height $wire xyplane rectangle
face create "Y-wire-2" width ($mesh*$wire) height $wire xyplane rectangle

face move "X-wire1" offset ($wire+$mesh) 0 0
face move "X-wire2" offset (2*($wire+$mesh)) 0 0
face move "X-wire-1" offset -($wire+$mesh) 0 0
face move "X-wire-2" offset -(2*($wire+$mesh)) 0 0

face move "Y-wire1" offset 0 ($wire+$mesh) 0
face move "Y-wire2" offset 0 (2*($wire+$mesh)) 0
face move "Y-wire-1" offset 0 -($wire+$mesh) 0
face move "Y-wire-2" offset 0 -(2*($wire+$mesh)) 0

face unite faces "X-wire0" "Y-wire0" "X-wire1" "X-wire2" "X-wire-1"
"X-wire-2" "Y-wire1" "Y-wire2" "Y-wire-1" "Y-wire-2" real

face intersect faces "jet" "X-wire0"
```

B.2 Filter MIN parameterised model

```
/Parameters
$wire = 25
$mesh = 25

/create jet
face create "jet" radius 75 xyplane circle

/create filter
face create "X-wire0" width $wire height ($mesh*$wire) xyplane rectangle
face create "X-wire1" width $wire height ($mesh*$wire) xyplane rectangle
face create "X-wire2" width $wire height ($mesh*$wire) xyplane rectangle
face create "X-wire-1" width $wire height ($mesh*$wire) xyplane rectangle
face create "X-wire-2" width $wire height ($mesh*$wire) xyplane rectangle

face create "Y-wire0" width ($mesh*$wire) height $wire xyplane rectangle
face create "Y-wire1" width ($mesh*$wire) height $wire xyplane rectangle
face create "Y-wire2" width ($mesh*$wire) height $wire xyplane rectangle
face create "Y-wire-1" width ($mesh*$wire) height $wire xyplane rectangle
face create "Y-wire-2" width ($mesh*$wire) height $wire xyplane rectangle

face move "X-wire1" offset ($wire+$mesh) 0 0
face move "X-wire2" offset (2*($wire+$mesh)) 0 0
face move "X-wire-1" offset -($wire+$mesh) 0 0
face move "X-wire-2" offset -(2*($wire+$mesh)) 0 0

face move "Y-wire1" offset 0 ($wire+$mesh) 0
face move "Y-wire2" offset 0 (2*($wire+$mesh)) 0
face move "Y-wire-1" offset 0 -($wire+$mesh) 0
face move "Y-wire-2" offset 0 -(2*($wire+$mesh)) 0

face unite faces "X-wire0" "Y-wire0" "X-wire1" "X-wire2" "X-wire-1"
"X-wire-2" "Y-wire1" "Y-wire2" "Y-wire-1" "Y-wire-2" real

face intersect faces "jet" "X-wire0"
```

B.3 Jet parameterised model

```
/Parameters
$radius = 75
$height = 100

/create outlet volume
vertex create "v1" coordinates 0 0 0
vertex create "v2" coordinates 50 0 0
vertex create "v3" coordinates 0 50 0
vertex create "v4" coordinates 0 0 500
vertex create "v5" coordinates 50 0 500
vertex create "v6" coordinates 0 50 500

edge create "e1" straight "v1" "v2"
edge create "e2" straight "v1" "v3"
edge create "e3" center2points "v1" "v2" "v3" minarc arc

edge create "e4" straight "v1" "v4"
edge create "e5" straight "v2" "v5"
edge create "e6" straight "v3" "v6"

edge create "e7" straight "v4" "v5"
edge create "e8" straight "v4" "v6"
```

```
edge create "e9" center2points "v4" "v5" "v6" minarc arc
face create "outlet" wireframe "e1" "e2" "e3" real
face create "symmetry_x1" wireframe "e1" "e4" "e5" "e7" real
face create "symmetry_y1" wireframe "e2" "e4" "e6" "e8" real
face create "wall_outlet" wireframe "e3" "e5" "e6" "e9" real
face create "interior_jet_outlet" wireframe "e7" "e8" "e9" real
volume create "outlet" stitch "outlet" "symmetry_x1" "symmetry_y1"
"wall_outlet" "interior_jet_outlet" real
/create jet volume
vertex create "v7" coordinates 0 0 ($height+500)
vertex create "v8" coordinates $radius 0 ($height+500)
vertex create "v9" coordinates 0 $radius ($height+500)
edge create "e10" straight "v4" "v7"
edge create "e11" straight "v5" "v8"
edge create "e12" straight "v6" "v9"
edge create "e13" straight "v7" "v8"
edge create "e14" straight "v7" "v9"
edge create "e15" center2points "v7" "v8" "v9" minarc arc
face create "symmetry_x2" wireframe "e7" "e10" "e13" "e11" real
face create "symmetry_y2" wireframe "e8" "e10" "e14" "e12" real
face create "wall_jet" wireframe "e9" "e11" "e12" "e15" real
face create "interior_control_jet" wireframe "e13" "e14" "e15" real
volume create "jet" stitch "interior_jet_outlet" "symmetry_x2"
"symmetry_y2"  "wall_jet" "interior_control_jet" real
/create control volume and surface
vertex create "v10" coordinates 150 0 ($height+500)
vertex create "v11" coordinates 0 150 ($height+500)
vertex create "v12" coordinates 150 150 ($height+500)
vertex create "v13" coordinates 0 0 ($height+520)
vertex create "v14" coordinates 150 0 ($height+520)
vertex create "v15" coordinates 0 150 ($height+520)
vertex create "v16" coordinates 150 150 ($height+520)
edge create "e11" straight "v8" "v10"
edge create "e12" straight "v9" "v11"
edge create "e13" straight "v10" "v12"
edge create "e14" straight "v11" "v12"
edge create "e15" straight "v7" "v13"
edge create "e16" straight "v10" "v14"
edge create "e17" straight "v11" "v15"
edge create "e18" straight "v12" "v16"
edge create "e19" straight "v13" "v14"
edge create "e20" straight "v14" "v16"
edge create "e21" straight "v16" "v15"
edge create "e22" straight "v15" "v13"
face create "symmetry_x3" wireframe "e13" "edge.20" "e19" "e16" "edge.16"
face create "symmetry_y3" wireframe "edge.20" "e14" "edge.17" "e17" "e22"
face create "periodic_y1" wireframe "e16" "e20" "edge.18" "e18"
face create "periodic_x1" wireframe "e18" "edge.19" "e21" "e17"
face create "wall_control" wireframe "edge.16" "edge.18" "edge.19"
"edge.17" "e15"
```

```
face create "interior_inlet_control" wireframe "e22" "e19" "e20" "e21"
volume create "control" stitch "interior_control_jet" "wall_control"
"symmetry_x3" "periodic_y1" "periodic_x1" "symmetry_y3"
"interior_inlet_control" real

/create inlet volume
vertex create "v17" coordinates 0 0 ($height+1520)
vertex create "v18" coordinates 150 0 ($height+1520)
vertex create "v19" coordinates 0 150 ($height+1520)
vertex create "v20" coordinates 150 150 ($height+1520)

edge create "e23" straight "v13" "v17"
edge create "e24" straight "v14" "v18"
edge create "e25" straight "v15" "v19"
edge create "e26" straight "v16" "v20"

edge create "e27" straight "v17" "v18"
edge create "e28" straight "v18" "v20"
edge create "e29" straight "v20" "v19"
edge create "e30" straight "v19" "v17"

face create "symmetry_x4" wireframe "e19" "e23" "e27" "e24" real
face create "symmetry_y4" wireframe "e22" "e23" "e30" "e25" real
face create "periodic_y2" wireframe "e20" "e24" "e28" "e26" real
face create "periodic_x2" wireframe "e21" "e25" "e29" "e26" real
face create "inlet" wireframe "e27" "e30" "e29" "e28" real
volume create "inlet" stitch "interior_inlet_control" "symmetry_x4"
"periodic_y2" "periodic_x2" "symmetry_y4" "inlet" real
```

Bibliography

[1] S.V. Apte, K. Mahesh, and T. Lundgren. A eulerian-lagrangian model to simulate two-phase/particulate flows. Technical report, Center for Turbulence Research, Annual Research Briefs, 2003.

[2] S. Ardizzone, F.S. Dioguardi, P. Quagliotto, B. Vercelli, and G. Viscardi. Microcrystalline cellulose suspensions: effects on the surface tension at the air-water boundary. *Colloids and Surfaces A*, 176:239–244, 2001.

[3] O. Biganska and P. Navard. Phase diagram of a cellulose solvent: N-methylmorpholine-n-oxide-water mixtures. *Polymer*, 44:1035–1039, 2003.

[4] G. Boiger. Phd thesis. in print, Montanuniversity Leoben, Department of Petroleum Engineering, 2009.

[5] G. Boiger, M. Mataln, B. Gschaider, and W. Brandstätter. Part 2: Large particle modelling, simulation of particle filtration processes in deformable media. *International Journal of Multiphysics*, 2(2):191–206, 2008.

[6] R.M.H. Bouwman. Analysis of subgrid-scale models for turbulence modelling. Master's thesis, Katholieke Universiteit Leuven, Departement Fysica, 2004.

[7] R.M.H. Bouwman. Microscopy results. Technical report, CD-Laboratory for Applied Computational Thermofluiddynamics, 2005.

[8] R.M.H. Bouwman. Sem. Technical report, CD-Laboratory for Applied Computational Thermofluiddynamics, 2005.

[9] R.M.H. Bouwman. Visit i-report. Technical report, CD-Laboratory for Applied Computational Thermofluiddynamics, 2005.

[10] R.M.H. Bouwman. Optimierung diffusorteil der beblasungseinrichtung. Technical report, ICE Strömungsforschung GmbH, 2006.

[11] R.M.H. Bouwman. Proposition experiments. Technical report, CD-Laboratory for Applied Computational Thermofluiddynamics, 2006.

[12] R.M.H. Bouwman. Proposition experiments 2. Technical report, CD-Laboratory for Applied Computational Thermofluiddynamics, 2006.

[13] R.M.H. Bouwman. Proposition experiments 3. Technical report, CD-Laboratory for Applied Computational Thermofluiddynamics, 2006.

[14] R.M.H. Bouwman. Report 2006 q1 - q3. Technical report, ICE Strömungsforschung GmbH, 2006.

[15] R.M.H. Bouwman. Scheelite experiment. Technical report, CD-Laboratory for Applied Computational Thermofluiddynamics, 2006.

[16] R.M.H. Bouwman. Scheelite processing. Technical report, ICE Strömungsforschung GmbH, 2006.

[17] R.M.H. Bouwman. Visit ii - report. Technical report, CD-Laboratory for Applied Computational Thermofluiddynamics, 2006.

[18] R.M.H. Bouwman. Technical report 2008 i-iii. Technical report, ICE Strömungsforschung GmbH, 2008.

[19] A. Brandner and H.G. Zengel. De 3 034 685. Technical report, Akzona, 1980.

[20] W. Brandstätter, J. Leixnering, P. Faraldi, E. Merlone Borla, M. Ranalli, N. Vlachos, and A.G. Konstandopoulos. The styff-dexa project: Advanced simulation tools for ceramic foam diesel particulate filters. Technical report, ICE2005 - 7th International Conference on Engines for Automobile, 2005.

[21] W. Brandstätter, C. Wassermayr, and P. Prenninger. An integrated approach for the design of diesel engine exhaust systems to meet euro 4 and beyond emissions legislations. Technical report, THIESEL 2002/Thermodynamic Processes in Diesel Engines, 11.-13. September, Valencia, 2002.

[22] E. Taeger et al. *Cell. Chem. Technol.*, 20:289–301, 1986.

[23] F.A. Buijtenhuijs et al. *Das Papier*, 10:615–619, 1986.

[24] Konstandopoulos et al. The diesel exhaust aftertreatment (dexa) cluster: A systematic approach to diesel particulate emission control in europe. Technical report, A.G., SAE 2004-01-0694, 2004.

[25] J.H. Ferziger and M. Peric. *Computational Methods for Fluid Dynamics*. Springer, 1999.

[26] H. Firgo, M. Eibl, and D. Eichinger. Lenzinger berichte 75. Technical report, Lenzing AG, 1996.

[27] H. Firgo, M. Eibl, W. Kalt, and G. Meister. Lenzinger berichte 74. Technical report, Lenzing AG, 1994.

[28] M. Gruber. Phd thesis. in print, Montanuniversity Leoben, Department of Petroleum Engineering, 2006.

[29] B. Gschaider, C. Honeger, and C. Redl. Soot particle deposition within porous structures using a method of moments lattice boltzmann approach. Technical report, Computational Science ICCS 2004, 4th International Conference Krakòw Poland, 2004.

[30] M. Henschke, M.A. Waheed, and A. Pfenning. Wandeinfluss auf die simulationsgeschwindigkeit von kugeln. *Chemie Ingenieur Technik*, 72:1376–1380, 2000.

[31] D.P. Hill. *The Computer Simulation of Dispersed Two-Phase Flows*. PhD thesis, Imperial College of Science, Technology and Medicine, 1998.

[32] C.W. Hirt and B.D. Nichols. Volume of fluid (vof) method for the dynamics of free boundaries. *Journal of Computational Physics*, 39:201–225, 1981.

[33] C. Honeger. Piv messung an der modeldüse. Technical report, CD-Laboratory for Applied Computational Thermofluiddynamics, 2005.

[34] T.J. Horton, T.R. Fritsch, and R.C. Kintner. Experimental determination of circulation velocities inside drops. *The Canadian Journal of Chemical Engineering*, pages 143–146, 1965.

[35] Fluent Inc. *Fluent 6.3 User's Guide*. FLUENT Inc., 2006.

[36] S. Jary. Online quality control of viscose by means of image analysis. Technical report, Lenzing AG, 2002.

[37] S. J. Kadolph and A. L. Langfordt. *Textiles: Ninth Edition*. New Jersey: Prentice-Hall, 2002.

[38] G. Kastner. *Numerical modelling of Mould Powder Entrapment in a Continuous Casting Process*. PhD thesis, Montanuniversity Leoben, 2006.

[39] R. Kickinger. Contributions to the fluid mechanics of viscose spinning. Technical report, Johannes Kepler University, Department of Fluid Dynamics and Heat Transfer, 2002.

[40] C. Klein and Jr. C.S. Hurlbut. *Manual of Mineralogy*. John Wiley & Sons, Inc., 1999.

[41] P. Korbel and M. Novak. *Geillustreerde Mineralen Encyclopedie*. Rebo Publishers, 2001.

[42] B. Lafaurie, C. Nardone, R. Scardovelli, S. Zaleski, and G. Zanetti. Modelling merging and fragmentation in multiphase flows with surfer. *J. of Computational Physics*, 113:134–147, 1994.

[43] J. Leixnering, B. Gschaider, W. Brandstätter, and R.M.H. Bouwman. A multiscale simulation approach for diesel particulate filter design based on openfoam and dexasim. Technical report, Third OpenFoam Conference, 2007.

[44] OpenCFD Limited. Openfoam, the open source cfd toolbox, programmer's guide. Technical report, OpenCFD Limited, 2008.

[45] OpenCFD Limited. Openfoam, the open source cfd toolbox, user guide. Technical report, OpenCFD Limited, 2008.

[46] W.S. MacKenzie and A.E. Adams. *A Colour Atlas of Rocks and Minerals in Thin Section*. Manson Publishing, 1994.

[47] H.R. Manouchehri, K. Hanumantha Rao, and K.S.E. Forssberg. Review of electrical seperation methods, part 1: Fundamental aspects. *Minerals & Metallurgical Processing*, 17(1):23–36, 2000.

[48] H.R. Manouchehri, K. Hanumantha Rao, and K.S.E. Forssberg. Review of electrical seperation methods, part 2: Practical considerations. *Minerals & Metallurgical Processing*, 17(3):139–166, 2000.

[49] C. Michels and B. Kosan. Das lyocell-verfahren - gegenwärtige leistungsgrenzen aus stofflicher und technologischer sicht. Technical report, Thüringisches Institut für Textil- und Kunstoff-Forschung e.V., 2002.

[50] C. Michels and H. Mertel. Dd 229 708. Technical report, Akzona, 1984.

[51] A.F. Miller and A.M. Donald. Surface and interfacial tension of cellulose suspensions. *Langmuir*, 18:10155–10162, 2002.

[52] H. Mohammed, A.P. Triana, J.H. Johnson, and S-L. Yang. An advanced 1d 2-layer catalyzed diesel particulate filter model to simulate: Filtration by the wall and particulate cake, oxidation in the wall and particulate cake by no2 and o2, and regeneration by heat addition. Technical report, SAE 2006-01-0467, 2006.

[53] http://www.opencfd.co.uk/openfoam.

[54] http://www.paraview.org/.

[55] S.V. Patankar. *Numerical Heat Transfer and Fluid Flow*. Hemisphere Publishing Coorperation, 1980.

[56] U. Piomelli. High reynolds number calculations using the dynamic subgrid-scale stress model. *Physics of fluids A*, 5:1484–1490, 1993.

[57] W.H. Press, S.A. Teukolsky, W.T. Vetterling, and B.P. Flannery. *Nummerical Recipes, The Art of Scientific Computing, Third Edition*. Cambridge University Press, 2007.

[58] M. Ranalli, P. Kroner, and W. Brandstätter. Dpf soot mapping. a simple and cost effective measurement method for series development. Technical report, World Automotive Congress, Barcelona, Spain, 2004.

[59] Th. Röder, R. Möslinger, U. Mais, B. Morgenstern, and O. Glatter. Charakterisierung der lösungsstrukturen in technisch relevanten celluloselösungen. Technical report, Lenzing AG, 2002.

[60] C. Redl. In situ combustion modeling in porous media using lattice-boltzmann methods. Technical report, ECMOR VIII, Freiberg, 2002.

[61] C. Redl, C. Wassermayr, and J. Leixnering. On the numerical simulation in foam filter design for diesel exhaust gas system. Technical report, Haus der Technik, Essen, 2003.

[62] T. Rosenau, A. Potthast, H. Sixta, and P. Kosma. The chemistry of side reactions and byproduct formation in the system nmmo/cellulose (lyocell process. *Prog. Polym. Sci.*, 26:1763–1837, 2001.

[63] M.W. Rybczynski. Über die fortschreitende bewegung einer flüssigen kugel in einem zähen medium. *Bulletin International de Academie des Sciences de Cracovic*, pages 40–46, 1911.

[64] H.A. Stone. Fluid dynamics: Physical ideas, the navier-stokes equations, and applications to lubrication flows and complex fluids. Technical report, A presentation for AP298r, Division of Engineering & Applied Science, Harvard University, 2004.

[65] E. Taeger, H. Franz, and H. Mertel. *Formeln, Faserstoffe, Fertigware 4*, 4:14–22, 1984.

[66] M.A. Waheed, M. Henschke, and A. Pfenning. Simulating sedimentation of liquid drops. *Int. J. Numer. Meth. Engng*, 59:1821–1837, 2004.

[67] C. Wassermayr, W. Brandstätter, H. Schreier, and P. Prenninger. Virtual engineering of diesel exhaust systems to meet future emission legislation. Technical report, Presented at 2003 JSAE Annual Congress, 2003.

[68] C. Wassermayr and M. Kästenbauer. Modelle zur berechnung von strömung in partikelfiltern. Technical report, Forschungsinformationen der Montanuniversität Leoben, 2001.

[69] H. Weller. Derivation, modelling and solution of the conditionally averaged two-phase flow equations. Technical report, OpenCFD, 2005.

Index